THE UNIVERSITY OF CHICAGO

POLYMERS IN MOTION:
OBSERVATIONS OF ORDERING, FLUCTUATIONS, AND COARSENING IN BLOCK COPOLYMER FILMS WITH ATOMIC FORCE MICROSCOPY

A DISSERTATION SUBMITTED TO THE

FACULTY OF THE DIVISION OF THE PHYSICAL SCIENCES

IN CANDIDACY FOR THE DEGREE OF

DOCTOR OF PHILOSOPHY

DEPARTMENT OF CHEMISTRY

BY

JULIA G. MURPHY

CHICAGO, ILLINOIS

DECEMBER 2022

Isn’t it splendid to think of all the things there are to find out about? It just makes me feel glad to be alive – it’s such an interesting world. It wouldn’t be half so interesting if we knew all about everything, would it? There’d be no scope for imagination then, would there?

- *L. M. Montgomery, Anne of Green Gables*

Table of Contents

List of Figures

List of Tables

Abbreviations

2D	two-dimensional
3D	three-dimensional
AFM	atomic force microscopy
AFM-IR	atomic force microscopy infrared spectroscopy
BCP	block copolymer
C-AFM	conductive atomic force microscopy
DIA	direct immersion annealing
EC-AFM	electrochemical atomic force microscopy
GISAXS	grazing-incidence small-angle X-ray scattering
hBN	hexagonal boron nitride
HS-AFM	high-speed atomic force microscopy
IR	infrared scattering
KPFM	Kelvin probe force microscopy
P2VP	poly(2-vinyl pyridine)
P3DT	poly(3-decylthiophene-2,5-diyl)
P3HT	poly(3-hexylthiophene-2,5-diyl)
PA 6	polyamide 6
PAAm	polyacrylamide
PC-AFM	photoconductive atomic force microscopy
PCBM	phenyl-C61-butyric acid methyl ester
PCL	polycaprolactone
PDMS	poly(dimethylsiloxane)

PEG	polyethylene glycol
PEO	polyethylene glycol
PET	polyethylene terephthalate
PHEMA	poly(2-hydroxyethyl methacrylate)
PiFM	photo-induced force microscopy
PLLA	polylactic acid
PMMA	polymethyl methacrylate
PS	polystyrene
PSBMAm	polysulfobetaine methacrylamide
PSBVB	polysulfobetaine vinylbenzene
PTrFE	polytrifluoroethylene
PVDF	polyvinylidene fluoride
SAXS	small-angle X-ray scattering
SECM	scanning electrochemical microscopy
SEM	scanning electron microscopy
s-SNOM	scattering scanning near-field optical microscopy
SPL	scanning probe lithography
SVA	solvent vapor annealing
TEM	transmission electron microscopy
TEM	transmission electron microscopy
UVO	ultraviolet/ozone
XPS	X-ray photoelectron spectroscopy

Acknowledgments

To my advisor, Prof. Steve Sibener: Although I don't think you would admit it, thank you for taking a chance on me when I was a terrified first-year who decided that watching polymers wiggle with AFM was the coolest. It is amazing to think about how much I have grown as a scientist and person while in your group. Thank you for giving me so much freedom to explore, pushing me outside my comfort zone, and always having my back.

To Prof. Paul Rupar: Your class is the reason I had the confidence to pursue a chemistry degree. Thank you for your patience in teaching and dedication to your students; I would not be where I am today without you.

To Prof. David Dixon and Dr. Andy Sutton: Thank you for welcoming me into your labs and giving me an introduction to research. My skills, confidence, and curiosity grew under your tutelage and set me up to be successful in graduate school.

To my committee members, Prof. Stuart Rowan and Prof. Andrei Tokmakoff: I consider it a great privilege that I was able to have such a close working relationship with my candidacy committee and that you became the natural choices for my thesis committee. Stuart, I have greatly enjoyed being an Honorary Rowan Group member; thank you for letting me work (and party) with your group on so many different projects. Andrei, thank you for being such a great Department Chair over the years; I appreciate your unwavering support for students and

willingness to work towards a more inclusive, equitable department. And thank you for always coming to my posters at AMEWS meetings.

To the Sibener group, past and present - Ali, Becca, Blake, Caleb, Darren, Genevieve, Grant, Jacob, Jasper, Jeff, Jon, Josh, OG Kevin, Kevin 2, Mark, Michael, Michelle, Rachael, Ross, Sarah B., Sarah W., Stephen, and Tim: Thank you for being the most supportive, fun, wonderful group of humans and for making my time in graduate school so positive. Jon, thank you for teaching me about AFM, polymers, and Separate Projects, while also always being down to do something fun. Michelle, Rachael, the Sarahs, and Josh, thank you for proofreading, talking science, going on walks, and for demonstrating how to be a badass scientist.

To the Rowan group: Thank you for being my unofficial second group. I am proud of the work we did together and treasure the friendships I made. You were always a welcoming, safe place to come to when I needed it.

To Luis, Virgil, Amanda, and Doug: Thank you for your patience, encouragement, support, and time while I learned to navigate a lab and the world of research.

To Maria, Brenda, Tracy, Tanya, Melinda, Vera, Laura: Thank you for always helping me navigate the department and university administrative things. You always had the answers and made life so much easier.

To Justin and Qiti: I quite literally would not be able to do any of my research without you. Thank you for training me on so many instruments, answering so many questions, and your willingness to help.

To all the student committees and organizations I have served or been a part of - the Midwest Women in Science Committee, Women in Chemistry, the PSD EDI Committee, GRIT, and GSU: I am proud of the work that we put in and the many things we have accomplished. There's still a long way to go to create the just, equitable, and inclusive research world we want, so keep up the good fight.

To my wonderful friends: Sarah, thank you for being the best of friends and the chicken to my farmer. I will miss taking hours to get home because we can't stop talking, going to all the shows, and the countless hours spent on the office couch. I will forever ask you to proofread my emails and will always proofread yours. Jake, thank you for our potatoes. I appreciate your incredible ability to listen to and understand my crazy brain. The Bouncy Castle crew, thank you for welcoming me into your circle and letting me tag along for all your events. And also Jon.

To my family (and friends who might as well be family): Thank you for your patience and understanding during this unusual time of my life.

To Hannah: You are my example of what it means to be a strong woman and person. Thank you for laughing at my memes, teaching me how to code, and being the best sister anyone could ask for.

To Madre and Padre: Thank you for your unwavering support in my pursuit of becoming a scientist. You knew this path was right for me and guided me here even when I couldn't see it myself. Thank you for letting me take over the kitchen for my science projects, talking me through all the teary late-night phone calls, for care packages full of soup so I have real food, and for reminding me that I probably just need to get some sleep. You are responsible for the woman I have become, and I hope I have made you proud.

And finally, to Neil: I could not have gotten through these last few years of graduate school without you by my side. You have introduced me to so many new things and people, encouraged me to grow and look at the world differently, and given me a love of coffee and homebrew that errs on snobbery. Thank you for being there to help me through the hard times and making me laugh harder than anyone.

Abstract

The spontaneous self-assembly of block copolymers (BCPs) into a variety of morphologies makes these systems desirable templates for lithography-based applications, including next generation energy storage and filtration membranes. BCP thin films are sensitive to their preparation and operational environments, which often involve solvents or high temperatures and are limited in the extent of control over local thickness variations. As such, understanding the dynamic properties and organization of polymer thin films in these environments is critical for achieving control over the nanopattern structures, a goal for fundamental science as well as technology applications. Atomic force microscopy (AFM) offers a unique characterization method to capture the real-time dynamics of these systems non-destructively and with application-relevant conditions, including imaging at high temperatures.

The research presented in this thesis utilizes environmentally controlled AFM to directly observe the dynamics of terrace and hole formation in incommensurate BCP thin films, as well as domain interfacial fluctuations in confinement with lithographic templating using environmentally controlled AFM at high temperatures. These studies contribute to the understanding of the influences of structural defects and thermal fluctuations on nanopatterns, and how this disorder defines the limits of perfection in these films. BCP thin films are sensitive to local thickness variations and will form terraces and holes if the thickness is incommensurate. AFM imaging at high temperatures allows capture of the complete spatiotemporal evolution of the terraces and holes, revealing details of the thickness-dependent nucleation, growth, and coarsening mechanisms. Many applications for templated block copolymer films require long-range order that extends over wafer size scales and a variety of methods, known as directed self-

assembly (DSA), have been employed to control the domain ordering in these films. Despite the perfect linearly achieved with DSA techniques, disorder persists in the form of thermal fluctuations and pattern roughness. Slow-scan-disabled AFM increases the effective imaging time resolution such that these interfacial fluctuations can be captured in real time. Additionally, imaging at high temperatures captures the dynamics and interfacial fluctuations around individual defects in topographically confined cylinder-forming PS-b-PMMA, revealing the pathways by which defects evolve and annihilate during thermal annealing and how these structural defects influence thermal fluctuations of the polymer film.

Finally, environmental AFM is extended to characterize the local transport of redox mediators through membranes in liquid environments with combined scanning electrochemistry-atomic force microscopy (SECM-AFM). Understanding transport at the single-pore level is a crucial component towards the development of novel materials to meet increasing demands on water filtration. Overall, this thesis seeks to understand the influences of confinement on ordered block copolymer systems with advanced AFM techniques.

Introduction

Atomic force microscopy (AFM) has become a critical tool for the surface characterization and investigation of polymer materials. A broad variety of AFM modes and operational environments allow for measurements of different properties and dynamic processes, in addition to static imaging. In particular, AFM lends itself to characterization of block copolymer (BCP) thin films due to the sensitivity and complexity within these materials. BCP thin films are a fascinating system due to their ability to spontaneously self-assemble into a variety of morphologies, as well as their broad and facile applicability to many industrial applications, including next-generation energy storage and filtration membranes. However, BCP thin films are sensitive to their preparation and operational environments, which often involve solvents or high temperatures. Thus, understanding the dynamic properties and organization of polymeric thin films in these environments is critical for achieving control over the nanopattern structures, a goal for fundamental science as well as technology applications. AFM offers a unique characterization method to capture the real-time dynamics of these systems non-destructively and within application-relevant conditions, including imaging at high temperatures. Chapter 1 of this thesis discusses important developments in AFM technology that enable advanced characterization of polymer materials, including surface structure, function, and dynamics.

The work presented in this thesis focuses on diblock copolymer systems, in which there are two blocks covalently bonded in a linear arrangement, as depicted in **Figure I.1a-b**. Diblock copolymers can be described by three chain parameters: the degree of polymerization, N, which describes the total number of monomer units; the Flory-Huggins interaction parameter, X, which

describes the free energy of mixing between the different blocks; and the relative volume fraction of the blocks, *f*. These interaction parameters influence the formation of various phase morphologies, including lamellae, cylinders, and spheres, as shown in **Figure I.1c**. The work herein utilizes cylinder-forming poly(styrene-*block*-methyl methacrylate) (PS-*b*-PMMA), as in **Figure I.1b**. When cast as a thin film, diblock copolymers spontaneously phase separate into polycrystalline domain structures that lack long-range or directional ordering, natively forming a high-defect-density state called a fingerprint pattern, shown in **Figure I.2a**. If the film is incommensurate, terraces (also called islands) and holes form within the film. Chapter 2 presents a study of the early terrace and hole formation and growth in PS-*b*-PMMA thin films, as well as a discussion of the early stages of fingerprint pattern formation.

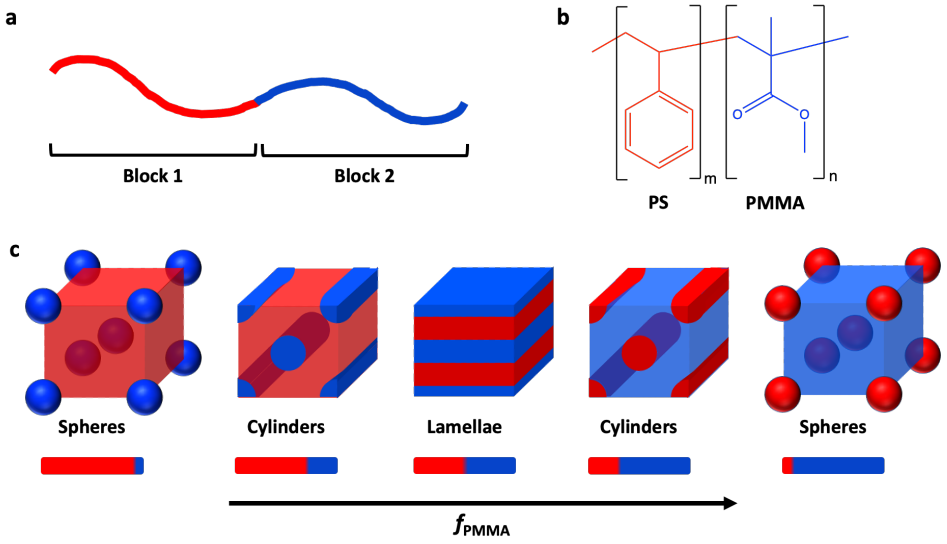

Figure I.1 Diblock Copolymer Phase Separation. (a) Schematic depiction of a diblock copolymer, consisting of two components (Block 1 and Block 2) that are covalently bonded in a linear arrangement. (b) Chemical structure of PS-*b*-PMMA, in which the PS block is shown in red and the PMMA block in blue. (c) Diblock copolymer morphology structures, including spheres, cylinders, and lamellae. The structures are shown in increasing volume fraction of the PMMA block (blue).

Many applications for templated BCP films require control over the long-range ordering and orientation of the domains that extends over wafer size scales. There is a need to achieve

perfect linearity in these ordered films, but also to control the formation of isolated defect structures, such as jogs, T-junctions, and bends, in the BCP nanopatterns in, for example, semiconductor devices. A variety of methods, known collectively as directed self-assembly (DSA), have been employed to control the domain ordering in BCP films. The work presented in Chapters 3 and 4 rely on a DSA technique called graphoepitaxy, in which the polymer is confined in lithographic trenches. When PS-*b*-PMMA is confined in lithographic templates on a silicon substrate, preferential alignment of the PMMA block with the silicon drives alignment of the domains along the trench walls, propagating linearly throughout the entire lithographic template and thus, providing control over the degrees of freedom and defect density in the domains. Aligned PS-*b*-PMMA in straight trenches is shown in **Figure I.2b**. It is important to note that this alignment occurs during an annealing process. The as-cast polymer films exist in a quenched state and cannot move freely at ambient conditions. Exposure to a solvent vapor or elevated temperature above the glass transition enables polymer mobility, which in turn allows defect healing and domain alignment. The work presented in Chapter 3 utilizes lithographic trenches to examine and measure the interfacial fluctuations and roughness in linearly ordered PS-*b*-PMMA when the system is brought to annealing temperatures.

If the width of the lithographic trench is tapered - that is, gradually decreases - defects in the nanopattern are generated in a precise manner, allowing for controlled study of defect behavior and formation that is directly observable with AFM imaging, as shown in **Figure I.2c**. Chapter 4 examines PS-b-PMMA thin films confined in such tapered-width trenches with AFM at elevated temperatures, revealing the pathways by which defects evolve and annihilate during thermal annealing and how these structural defects influence thermal fluctuations of the polymer film.

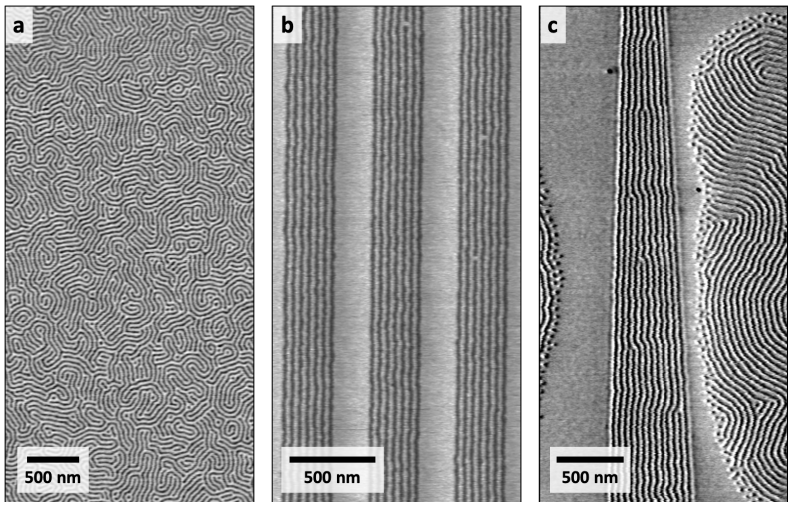

Figure I.2 PS-*b*-PMMA Self-Assembly Patterns. AFM phase images showing PS-*b*-PMMA (a) fingerprint, (b) linearly aligned in straight lithographic channels, and (c) confined in tapered-width lithographic channels.

Finally, as an extension of AFM, the last chapter in this thesis presents current work on utilizing combined scanning electrochemical-atomic force microscopy (SECM-AFM) to characterize local transport through membranes *in operando*. SECM is a scanning probe technique that provides local surface electrochemical information through monitoring redox reactions between a scanning probe and redox mediators in an electrolyte solution. When combined with AFM, this technique can provide high resolution mapping of surface reactivity to structure. Chapter 5 presents progress towards using SECM-AFM to monitor transport through commercial water filtration membranes, as well as the outlook for more advanced characterization of individual pores and novel membranes with this technique.

Overall, the work in this thesis seeks to understand the influences of confinement on ordering, interfacial fluctuations, and coarsening in block copolymer systems with advanced AFM techniques. My work on each of these projects has contributed to an extensive literature working towards achieving perfection in block copolymer thin films and nanopatterns.

Chapter 1.

Correlating Polymer Structure, Dynamics, and Function with Atomic Force Microscopy

Reprinted with permission from J. G. Murphy, J. G. Raybin, S. J. Sibener. *J. Polym. Sci.* **2022**, *60*, 1042-1058.[1]

Since its development, atomic force microscopy (AFM) has become an indispensable tool for investigating fundamental and technological applications of polymer materials. The versatility of AFM imaging modes and operating conditions allows for nanoscale characterization of a range of dynamic processes, such as crystallization, phase separation, self assembly, and electronic transport. Advances in AFM technology, particularly high-speed and high-resolution imaging, enable investigation of polymer structure, function, and dynamics in real world conditions and across a range of relevant spatial and temporal scales. In this Chapter, I highlight a collection of recent polymer studies that utilize AFM to correlate the function and structure of polymer films, with focus on its multiparametric imaging capabilities. As the complexity of polymer materials and morphologies continues to increase, AFM is well poised to meet the accompanying demand for nanoscale imaging and characterization.

1.1 Introduction

Due to their remarkable material flexibility, polymers have found widespread use in many contemporary fundamental and technological applications. Polymer structure and function depend hierarchically on their chemistry and chain architecture, as well as their organization and aggregation.[2] Structural organization occurs over a hierarchy of length scales, ranging from the conformational packing of individual chains to the self-assembly of mesoscale patterns. Similarly, polymer dynamics span a range of time scales, from rapid single-chain reptation to slow bulk diffusion and mass transport. This multiscale material heterogeneity yields emergent and application-specific functionality. As new and increasingly complex polymer materials are continually designed, imaging methods must meet the challenge of correlating local structure and function over the full breadth of relevant structural and dynamic properties.

In this Chapter, I examine the contributions of atomic force microscopy (AFM) toward addressing key developments in polymer science. The multiparametric imaging capabilities of AFM make this technique particularly useful for investigating the structure, dynamics, and functionality of polymer surfaces and interfaces.[2-4] I follow in the footsteps of an excellent recent review by Wang and Russell.[4]

Alongside AFM, many nanoscale imaging techniques have been employed to understand the structure and function of polymer materials, with electron microscopy (SEM and TEM) and X-ray scattering (SAXS and GISAXS) methods, being among the most commonly used.[5-7] While electron microscopy offers fast scan rates and high resolution, polymer samples are generally sensitive to damage from the electron-beam exposure, precluding dynamic measurements of a single region. Additionally, polymers often require pretreatment (e.g. staining, mineralization, or encapsulation) to enhance contrast and stability.[8,9] Requisite

compatibility with a vacuum chamber also limits the capacity for *in situ* environmental control in SEM or TEM measurements. As complementary methods, X-ray scattering experiments, i.e., small-angle X-ray scattering (SAXS) and grazing incidence small-angle X-ray scattering (GISAXS), reveal mesoscale ordering and phase transitions in polymer systems.[10,11] Reciprocal space measurements provide bulk information averaged over the sample or, for GISAXS, averaged over the film surface. Most X-ray scattering experiments still rely on synchrotron radiation, narrowing instrumental access. Lastly, both electron microscopy and X-ray scattering measurements are typically limited to obtaining only structural information, requiring external acquisition of functional properties. AFM stands out for its unrivaled capability to study a wide breadth of structural and dynamic features nondestructively in real space and time, and in a variety of application-relevant conditions.

Since its development 35 years ago, AFM has proven to be a powerful and flexible tool for characterizing nanoscale materials.[12,13] Over time, this initially revolutionary advancement has become part of the everyday toolkit for polymer scientists, transforming our understanding of nanostructure and processes. New advances in AFM imaging have successfully overcome a series of traditional limitations; these developments have been catalogued in detail in refs. 14 - 18.[14-18] Although the focus of this Chapter will predominantly be on synthetic polymer systems, many of the key developments have been the result of efforts studying biologically-derived polymers.[14,17,19-21] The mission to capture biological mechanisms and dynamics in real time and under physiologically relevant conditions have highlighted the demand for gentle, non-perturbative imaging, fast scan rates, and imaging in liquid environments. These same methods have also been applied to answer critical questions in synthetic polymer systems. Among these developments, high-resolution, high-speed, and environmentally-controlled AFM, in particular,

have expanded the scope of functionality that can be understood at the local scale: high-resolution imaging captures the structure of single molecules; high-speed AFM has transformed the ability to track dynamics in real-time; and environmentally-controlled AFM has enabled simulating real-world conditions *in situ*.

In this Chapter, I highlight a collection of recent advances in AFM imaging with a focus on the potential applications of synthetic polymeric materials. I first introduce AFM along with a few of the key modes and capabilities that have enabled characterization of polymer function alongside imaging. I then examine the contributions of AFM to a range of topics in polymer science: crystallization, self-assembly, polymer electronics, transport, and solvation. The versatility of AFM has unlocked new and ongoing potential for uncovering structural, dynamic, and functional properties of polymers.

1.2 AFM Methods for Polymer Analysis.

AFM is a scanning probe technique that measures the force between the tip of a cantilever probe and a sample surface. It was first developed by Binnig, Quate, and Gerber in 1986, extending the scope of scanning tunneling microscopy to non-conductive samples.[12] Since their invention, AFM systems have become more advanced but the underlying principles remain the same. The AFM probe, consisting of a force-sensing cantilever equipped with a sharp nanoscale tip, is brought in contact with, or in proximity to, the sample surface. As the probe is scanned over the region of interest, variations in the cantilever's response are used as feedback to control the tip-sample separation and maintain a consistent interaction force. In this manner, AFM imaging may be used to directly interrogate the sample's topography and nanomechanical response. This force-measurement scheme can be further generalized to study a wide range of

surface attributes and map local heterogeneities in the electronic, magnetic, optical, or electrochemical properties of a sample.[4] This multiparametric capability of AFM enables its unique ability to correlate surface structure and functionality.

A particularly valuable feature of AFM is its amenability to a wide range of sample environments, including ambient, vacuum, and liquid environments, that simulate real-world operational conditions.[22,23] It can be used in an oxygen- and water-free glovebox, as well as under controlled humidity or solvent-vapor conditions relevant to polymer processing.[24,25] The AFM stage can also be heated to observe dynamics or high-temperature phase transitions or cooled to promote stability.[26-28] Fluid-cell imaging in which the sample and AFM probe are immersed in an aqueous solution has long been used for biological samples and has been extended to other polymer systems. This method can help with sample preservation and imaging stability, while also replicating physiological conditions.[29]

Advances in AFM imaging have helped to build on its natural strengths and to overcome its traditional limitations. Improvements in noise stabilization have enhanced AFM's sensitivity and spatial resolution such that commercial AFMs are now frequently used to resolve molecular features.[15,21]

1.2.1 Imaging Modes

The wide variety of AFM imaging modes make it an all-in-one tool for polymer characterization. In the simplest imaging scheme, the tip stays in contact with the surface (contact mode) and the feedback loop ensures a constant cantilever deflection. In amplitude-modulated AFM (tapping mode), the tip is oscillated at or near its fundamental resonant frequency, and the amplitude of the oscillations is used to monitor the sample interaction.

Intermittent contact with the sample reduces lateral forces in order to minimize damage to the tip and sample.[15] As another benefit of tapping mode, measurements of the phase offset between the oscillating drive frequency and cantilever response correspond with energy dissipation at the tip.[30] Phase imaging is particularly useful for studying polymeric systems where phase is associated with viscoelastic damping and can be used to map compositional or structural variation of the polymer surface.[31] However, the phase signal depends on a complex combination of dissipative and conservative interactions and is even susceptible to contrast inversion, making interpretation difficult. New methods of relating phase to real surface properties, has facilitated direct and quantitative viscoelastic measurements.[32,33] As one example, loss tangent mapping, derived from AFM phase imaging, measures the ratio of dissipative and conservative tip-surface interactions. Shown in **Figure 1.1**, such mapping can be used to distinguish the structural and compositional heterogeneity of a polymer blend during *in situ* crystallization.[33]

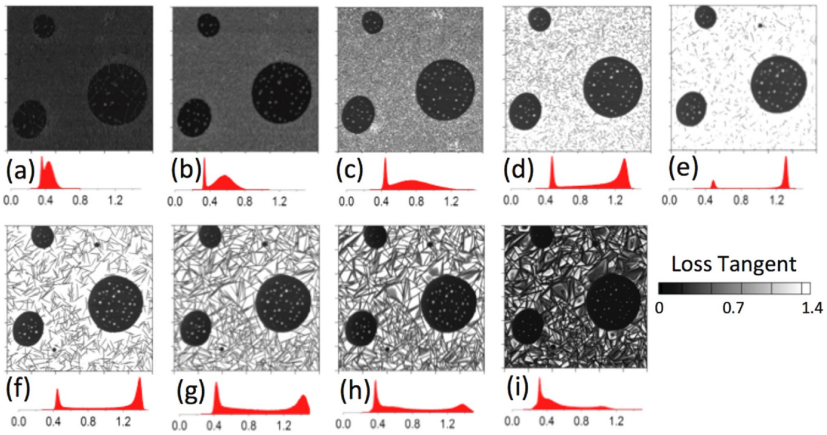

Figure 1.1 AFM Loss Tangent Mapping. AFM loss tangent images throughout an *in situ* heating experiment of a polymer blend film with a continuous phase of PP surrounding PS domains. The images Ire acquired as the film was first heated to (a) 55 C, (b) 80 C, (c) 100 C, (d) 120 C, and (e) 135 C, and then cooled to (f) 120 C, (g) 100 C, (h) 80 C, and (i) 55 C. Nanomechanical contrast of the loss tangent images tracks both the compositional differences as well as the structural evolution of the PP phase during crystallization. Reproduced with permission from Proksch, R.; Kocun, M.; Hurley, D.; Viani, M.; Labuda, A.; Meinhold, W.; Bemis, J. *J. Appl. Phys.* **2016**, *119*, 134901.[33] Copyright 2016 AIP Publishing LLC.

Quantitative measurements of polymer material properties can also be performed through a variety of nanomechanical imaging modes.[18] With off-resonant nanomechanical mapping, the cantilever is oscillated at a lower frequency in order to capture complete force-distance curves on each oscillation cycle. Additionally, multifrequency AFM, in which the cantilever is simultaneously excited at multiple resonances, allows for the concurrent acquisition of multiple parameters for decoupling the sample's intrinsic material properties from the tip specific interaction. Each excited mode can be maintained through different feedback channels or left open according to the experimental design.[16,34,35]

Advanced imaging modes utilize AFM's force-sensing capabilities to image a variety of functional properties. These modes are often coupled with application-specific cantilevers. For example, in conductive AFM (C-AFM), current flow between the sample and a metallic or metal-coated cantilever is used to map variations in electrical conductivity.[36] In Kelvin probe force microscopy (KPFM), tip bias is controlled to minimize mechanical oscillations and match the sample's surface potential.[36,37] In AFM-IR modes, a metallized probe acts as an antenna to locally amplify the spectroscopic signal for sub-diffractive imaging. These methods measure changes in either sample polarizability and thermal expansion (photo-induced force microscopy, PiFM) or in the tip-scattered light (scattering scanning near-field optical microscopy, s-SNOM) as a function of excitation wavelength.[38,39] In electrochemical AFM (EC-AFM), the probe is used to monitor redox chemistry of samples immersed in an electrolyte solution.[40] For these measurements, a conductive probe is coated in an insulating sheath exposing only the tip apex to ensure sensitivity to local reactivity. These modes represent just a few of many functional imaging capabilities, and with any of these techniques, multiparametric imaging allows direct correlation with the local surface topography or other properties.

1.2.2. High-Speed AFM

The development of high-speed AFM (HS-AFM) has opened up the possibility of imaging dynamic samples in real time with minimal interference from the imaging method. Imaging time-resolution has improved dramatically for real-time observation of dynamic processes, reflecting a remarkable transition from timelapse (multi-minute) to video rate (sub-second) imaging. HS-AFM advancements Ire largely initiated from biological studies, in which there was a desire to image at rates fast enough to capture dynamic biological processes, while also having the ability for non-destructive, label-free, and physiologically relevant imaging conditions. The development of this technique required advancements in nearly all components of traditional AFMs, including cantilevers, cantilever excitation methods, deflection measurement, scanners, and controllers, and subsequent commercialization of these ongoing developments has increased the accessibility of HS-AFM.[41-54]

One of the more notable accomplishments of HS-AFM is the elucidation of the translocation mechanism or walking of myosin V along actin filaments by Kodera et al., in which the authors used HS-AFM to capture the dynamic conformational changes in the protein in real time.[55] High-speed imaging has continuing relevance for polymer samples, including crystallization, polymerization, diffusion, and mesoscale self-assembly.[56-60] Recently, Kretzmann et al. used HS-AFM to directly observe polymer dynamics at a liquid-solid interface, replicating physiological conditions, to better understand the role of polymers in biomedical delivery applications.[61]

1.2.3. Subsurface Imaging

The functionality of many polymer systems depends not only on their surface, but on the nanostructural organization buried within their three-dimensional (3D) volume. While AFM is conventionally considered to be sensitive to only surface and near-surface regions, advancements in imaging methodology and theory have unlocked the potential for subsurface imaging.[62] In subsurface imaging modes, tip-sample interactions are influenced by the full volume underlying the contact point and consequently reflect a convolution of surface and subsurface properties. Decoupling these interactions is not obvious, and careful approaches are necessary to reconstruct a 3D map from a two-dimensional (2D) scan. In particular, imaging contrast in heterogeneous materials is dependent on both the depth and the physical contrast of subsurface features, and complete reconstructions must differentiate between these factors. A wide range of subsurface imaging modes have been developed, including nanomechanical, acoustic, and optical methods.[62] In polymer films, these methods have been used to map the organization of buried polymer crystallites and nanoparticles and to measure the depth of stacked multilayer films.[63-65]

1.2.4. Force Spectroscopy

In addition to imaging modes, the AFM tip can be used to measure tip-surface interactions as a function of sample distance.[66] In nanoindentation experiments, the probe is repeatedly depressed into a compliant sample surface to measure its viscoelastic response. The probe can also be used to "fish" individual polymer chains and measure their extension as the cantilever is retracted. The resulting force-distance spectra contain rich material information on local elasticity, hardness, and adhesion. All force spectroscopy data must be coupled with nanomechanical modeling to determine these rheological properties. Local force measurements

can be used to relate the mechanical properties of single polymer chains to bulk continuum properties.[67]

1.2.5. Scanning Probe Lithography

Alongside its characterization capabilities, the AFM nanoscale probe can be used to lithographically manipulate a sample surface.[68,69] Increasing the tip-sample interaction force can transition from a non-perturbative imaging mode to a lithographic mode that purposefully deforms, removes, or otherwise alters the scanned region.[70] Scanning probe lithography (SPL) is well-suited for the direct patterning of nanoscale features in polymer films.

In the simplest application of SPL, the scanning action is used to mechanically scratch or plow the polymer surface.[71] Alternative lithographic approaches take advantage of the ability to locally modify tip properties: thermal probes can be used to locally induce crystallization or mass flow in polymer samples and conductive probes can generate electric fields for manipulating charged samples.[72,73] In dip-pen lithography, the tip is coated in a fluid material, which it deposits (writes) by tracing over the surface.[74] Each of these methods is well-suited for the modification of polymer films due to their responsiveness and adaptability. While raster scanning limits throughput of SPL, the development of multiple tip write arrays has increased lithographic efficiency.[75]

1.3. Polymer Applications

1.3.1. Crystallization

More than half a century of intensive experimental and theoretical progress has served to advance our understanding of polymer crystallization.[76,77] Along the way, AFM has contributed

significantly to these efforts, with direct real-space imaging helping to resolve debates and to inspire the development of new crystallization models.[4,78] Still, many key questions remain unanswered and polymer crystallization has been highlighted as a top remaining challenge in polymer physics.[77,79]

Below the equilibrium melting temperature, semicrystalline polymers adopt a metastable morphology including both crystalline and amorphous regions. In these systems, polymer chains fold into crystalline lamellar sheets with nanoscale thicknesses interposed with amorphous layers. On the mesoscale, lamellae further organize into a diverse array of structures, including single-crystal platelets, branching dendrites, and space-filling spherulites. The morphology and degree of crystallinity in semicrystalline systems is dependent on the sample's processing history as limited by crystallization kinetics. For any of these forms, structural heterogeneity also leads to local variation in polymer properties and functionality.[78]

Key features of folded chain crystallization are captured by secondary nucleation theory, developed by Hoffman and Lauritzen, which describes the attachment of polymer stems at the crystal growth front.[80] This model is based on a single-step growth process in which a sharp capillary interface separates crystalline and amorphous regions. However, AFM observations of the formation of lamellar crystallites challenged these assumptions. Following crystallization from the melt, syndiotactic polypropylene lamellae exhibit a knobbled texture indicative of a multistage crystallization process in which discrete crystal subunits fuse to form lamellar sheets.[81] In measurements of spherulite formation in bisphenol A, AFM phase images identify a region with gradually shifting contrast at the growth front between crystalline and amorphous regions.[82] Consistent with these observations, a multistage crystallization theory, developed by

Strobl, introduced an intermediate mesomorphic region in which polymer chain organization and mobility change continuously when approaching the growth front.[83]

Advances in AFM imaging stability have enabled measurements of the lamellar substructure and growth processes with molecular and submolecular resolution. Kumaki et al. first observed the characteristic folded-chain structure in 2D isotactic PMMA crystals prepared through the slow compression of a monolayer Langmuir-Blodgett film and deposited on mica.[84] More recently, humidity-induced crystallization of isotactic PMMA has enabled *in situ* observations of nucleation and growth processes with molecular resolution.[85] The crystals exhibited stepwise growth kinetics, potentially due to the attachment of discrete polymer chains and further indicative of a multistage crystallization process. The evolution of crystal shapes revealed significant chain mobility and cooperative slipping even within aligned lamellae. In separate experiments, high-resolution imaging of 2D P3DT crystals on hBN also clearly resolved the folded-chain structure of the polymer backbone as well as faint contrast of the perpendicularly orientated decyl side chains, **Figure 1.2a-c**.[86] The packed crystalline stems fold in place, connected by tie-chains with sharp hairpin bends. To further improve imaging sensitivity, measurements using a small oscillation amplitude and the third cantilever eigenmode distinguished individual sulfur atoms within the thiophene rings, as identified by the extended size of the sulfur lone-pair, **Figure 1.2d**. The P3DT lamellae Ire found to orient with three-fold symmetry, guided by epitaxial alignment of the alkane side chains with the hBN substrate. This contrasts with observations of isotactic PMMA on mica, which showed only partial alignment with the substrate lattice. Instead, the orientation was determined during the initial nucleation step and reinforced through subsequent coarsening.[85] In substrate confined systems, a balance

of epitaxial and interchain interactions must be accounted for in understanding crystal organization.

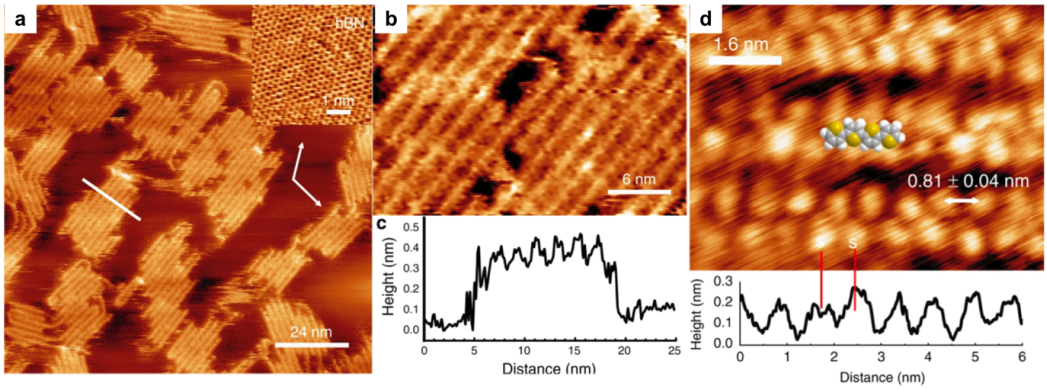

Figure 1.2 Folded Chain Lamellar Structure. High-resolution tapping mode height images of two-dimensional P3DT adsorbed on the surface of hBN. (a) The folded-chain lamellar structure is clearly visible in the topographic image; the inset shows a lattice frequency shift image of the hBN substrate. Three-fold orientational symmetry of crystalline domains is due to epitaxial alignment with the hBN lattice. (b) A selected area from scan (a) shows the organization of individual PT molecules and orthogonally-oriented low-contrast features associated with decyl side chains. (c) A height profile along the line in (a) shows a molecule-to-molecule separation of 1.95 ± 0.02 nm. (d) An AFM height image acquired using the third cantilever eigenmode resolves features associated with individual sulfur atoms in the P3DT chains with 0.81 ± 0.04 nm interatomic spacing. Adapted under Creative Commons Attribution 4.0 International License. (http://creativecommons.org/licenses/by/4.0/) from V. V. Korolkov, A. Summerfield, A. Murphy, D. B. Amabilino, K. Watanabe, T. Taniguchi. P. H. Beton, *Nat. Commun.* **2019**, *10*, 1537.[86]

Molecular resolution has also been achieved outside of 2D, surface-confined polymers. AFM imaging has visualized the lattice structure of P3HT crystals at the surface of a spin-coated film, in which π-π stacking of the thiophene backbones leads to alignment of hexyl chains in a square lattice normal to the surface plane.[86] With high-speed AFM imaging, Acevedo-Cartagena et al. observed the real-time surface nucleation of P3HT nanofibers from a supersaturated solution. Phase imaging of the nanofibers tracked their growth and clearly resolved crystalline packing of the backbone and hexyl side chains in alignment with the nanofiber axis.[87]

Chain-packing interactions within a crystal can be measured through single-molecule force spectroscopy. With finite probability, contact between the AFM probe and a polymer crystal leads to physisorption of an individual chain. As the chain is drawn from the crystal lattice, periodic peaks in the force-extension spectrum correspond with the removal of each complete fold, as shown in experiments with PA 6 in **Figure 1.3a-b.**[88] The magnitude and substructure of each peak further reveal the nature of chain packing interactions, **Figure 1.3c-d**. Stick-slip profiles result from incremental breaking and reformation of hydrogen bonds at each repeat monomer unit. Similar stick-slip motion, albeit with lower magnitude forces, is observed in PCL crystals, in which chains are stabilized through electrostatic dipole interactions.[89] In contrast, PEO and PLLA chains, which adopt a helical chain conformation, instead show continuous unraveling of each lamellar fold.[89,90]

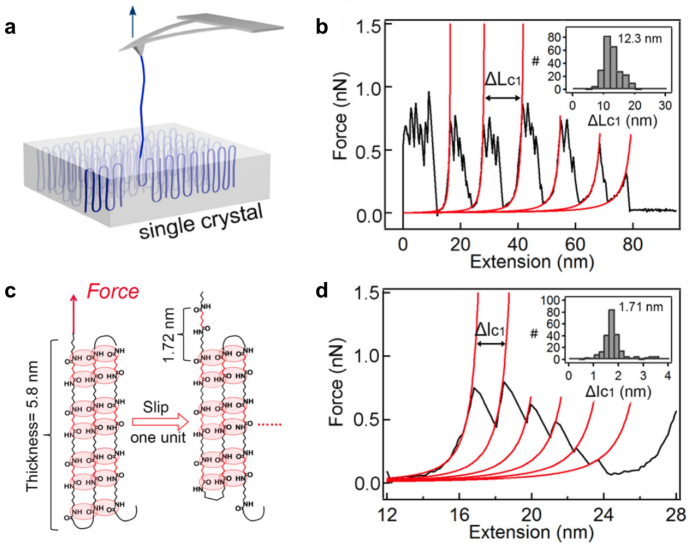

Figure 1.3 Single-Molecule Force Microscopy. (a) Scheme of a single-chain pulling experiment from a single crystal. Adapted with permission from Y. Song, Z. Ma, P. Yang, X. Zhang, X. Lyu, K. Jiang, W. Zhang, Macromolecules 2019, 52, 1327–1333.[89] Copyright 2019 American Chemical Society. (b) Force extension curves of PA 66 chains have periodic structure corresponding to the unraveling of successive polymer folds. (c) Schematic showing hydrogen bonding interactions between adjacent polymer chains within the lattice. (d) The substructure of each peak shows stick-slip motion due to iterative breaking and reforming of these hydrogen bonds between monomer units. Adapted with permission from X. Lyu, Y. Song, W. Feng, W. Zhang, *ACS Macro Lett.* **2018**, *7*, 762–766.[88] Copyright 2018 American Chemical Society.

1.3.2. Block Copolymer Self-Assembly

Block copolymers (BCP) have garnered attention from academia and industry for their ability to self assemble into periodic nanoscale patterns with features sizes smaller than can be obtained through traditional lithographic methods.[91,92] The periodic structures adopt a variety of stable morphologies, including lamellae, cylinders, or spheres, depending on the relative volume fraction of the blocks.[93,94] However, lack of directional preference for alignment limits long range ordering and produces defect-dense fingerprint patterns, as shown in an AFM phase image of cylinder-forming PS-b-PMMA in **Figure 1.4a**. There has been a concerted effort to guide the self-assembly process in order to control the orientation and organization of the patterns. Ordering can be achieved through external guiding fields (i.e. electric fields, solvent flow, strain) that break symmetry and ensure a preferred pattern orientation. Alternative strategies have focused on directed self-assembly through lithographic substrate patterning under two broad categories: (1) graphoepitaxy, which modifies the substrate topography,[95] and (2) chemoepitaxy, which modifies the substrate chemistry.[96] In each case, the periodicity of the lithographic pattern is multiplied by the BCP self-assembly process to produce patterns with finer resolution than achieved through top-down methods alone.[92] An example of graphoepitaxy, again with cylinder-forming PS-b-PMMA, is shown in **Figure 1.4b** before and after alignment. In addition to fully aligned systems, the formation and location of dislocations can be further controlled by the channel geometry, as with tapered channels in which the width varies continuously. Dislocations form at regularly-spaced sites where the channel width does not accommodate an integral pattern spacing, shown in **Figure 1.4c**. With *in situ* AFM imaging, tracking the motion of individual dislocations allows for controlled measurements of defect energetics and diffusivity.[97]

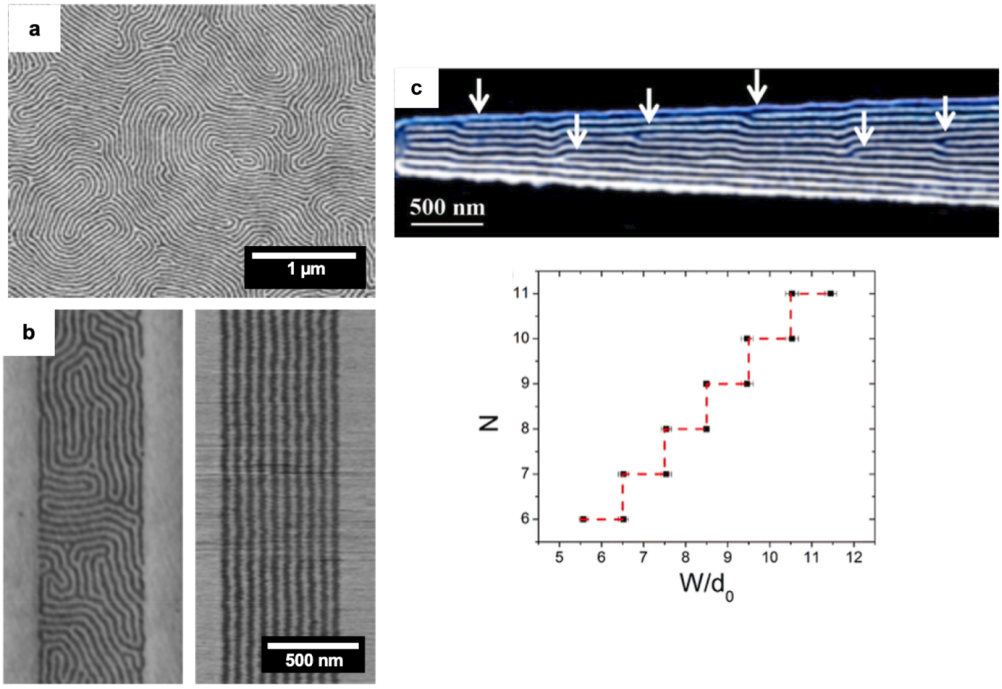

Figure 1.4 Cylinder Domain Alignment *via* Graphoepitaxy. (a) AFM phase image of cylinder-forming block copolymer in a fingerprint pattern. The BCP in this image is PS-b-PMMA. (b) AFM phase images illustrating the graphoepitaxy process with cylinder-forming PS-b-PMMA. The cylinders preferentially align with the channel sidewalls, propagating linear alignment throughout the polymer upon thermal annealing. (c) Representative images showing confinement of PS-b-PMMA in annealed tapered-width channels. Dislocations, indicated with white arrows in the AFM phase image, occur at regular intervals along the length of the channel, as shown in the plot of number of cylinder domains, N, versus the confinement width, W, in terms of equilibrium periodicity, d_0; the black dots represent the dislocation positions. Adapted with permission from Q. Tong, Q. Zheng, S. J. Sibener, *Macromolecules* **2014**, *47*, 4236–4242.[97] Copyright 2014 American Chemical Society.

The intricate patterns produced by BCPs have inspired AFM imaging from early in its development.[98] Real-space images of BCP morphology served as direct confirmation of its structure as predicted theoretically and measured in reciprocal space through X-ray and neutron scattering experiments.[93] AFM phase imaging, as shown in **Figure 1.4**, measures differences in the viscoelastic properties of the BCP components to produce a compositional map. In combination with topographic imaging, phase images are routinely used to relate the microstructure to various material parameters, including composition, molecular weight, film thickness, and interfacial interactions, and composition.[94,99] In addition to elucidating the

surface morphology, subsurface imaging of BCP patterns has been used to map the 3D structure of embedded cylinders, distinguishing depth information from the materials' mechanical contrast.[63,100]

Beyond structural characterization, the AFM environment can be controlled to replicate BCP processing conditions — including solvent-vapor annealing (SVA), direct immersion annealing (DIA), and thermal annealing — and track pattern evolution. The presence of solvent vapor plasticizes polymer films while also swelling the BCP domains and mediating block interactions. During SVA, polymer films therefore freely reorganize to adopt a new equilibrium morphology as defined under solvent swollen conditions.[101-103] However, measurements of the quenched state following SVA are complicated by chain collapse, gradients in solvent flow, and surface dewetting upon solvent removal. For example, Zhang et al. showed that thermally annealed PS-b-P2VP films with cylinders, initially oriented perpendicular to the substrate, exhibit dewetting after SVA, with parallel cylinders near the dewetted regions. After SVA for 24 h, the parallel alignment propagates across the film, as the cylinders align with the moving contact line at the edge of a dewetted region.[104] Environmental AFM imaging offers the potential to image these annealing processes *in situ*, capturing the annealing dynamics and mechanisms in real time, as well as capturing the morphological changes that accompany deswelling of the polymer films. Takano et al. recently demonstrated *in situ* AFM imaging within a sealed SVA chamber, enabling direct measurements of solvent-swollen films. The system monitored the coarsening of fingerprint patterns in ultrahigh molecular weight PS-b-PMMA thin films over an 8 h period of *in situ* SVA imaging, shown in **Figure 1.5**.[105] DIA offers a method to overcome many of the challenges associated with SVA, fully immersing BCP

films in a tunable solvent mixture, in order to maintain a finite interaction parameter for microphase separation.[106,107]

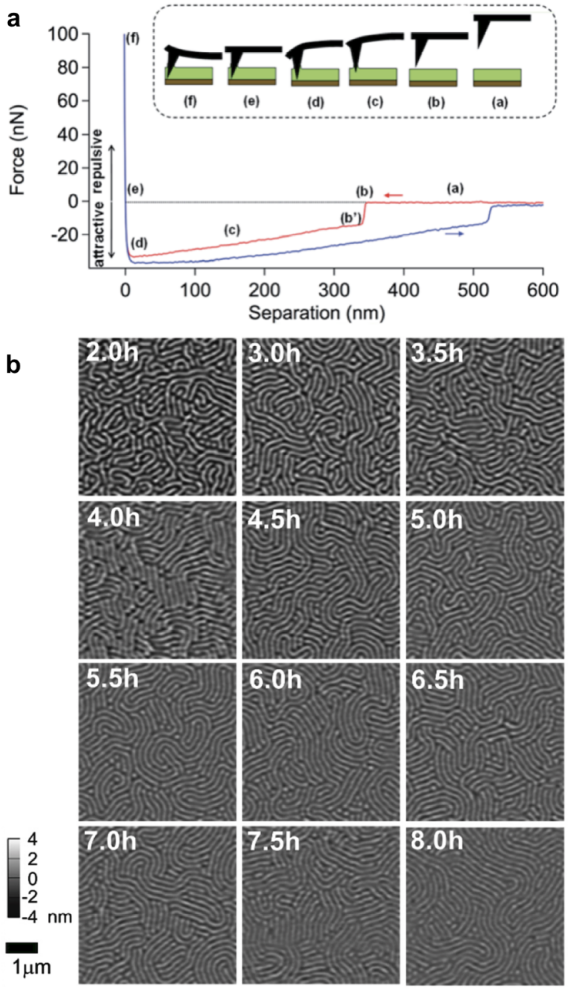

Figure 1.5 *In Situ* Solvent Vapor Annealing Force Measurements. (a) Schematic illustrating force-distance measurements in solvent-swollen films, along with a representative force-distance curve used to determine the thickness of the swollen film. (b) AFM topographic images of the solvent swollen films, showing the progression of the SVA *in situ*. Over the 8.0 h annealing time, the polymer domains coarsened and correlation length increased, while defect density decreased. Adapted under Creative Commons Attribution 4.0 International License (http://creativecommons.org/licenses/by/4.0/) from K. Takano, T. Nyu, T. Maekawa, T. Seki, R. Nakatani, T. Komamura, T. Hayakawa, T. Hayashi, *RSC Adv*. **2020**, *10*, 70–75.[105]

AFM imaging has been extensively used to study the dynamics and mechanisms of BCP defect healing and grain coarsening during thermal annealing. Harrison et al. first identified grain growth kinetics following a $t^{1/4}$ power law in striped fingerprint patterns, determined by the

annihilation of topological defect structures.[108] Subsequent *in situ* studies of unconfined thin films elucidated the complex pattern evolution mechanisms involved in the annihilation process.[109,110] Confinement in lithographic channels provides a controlled environment for isolating individual defect pairs, allowing for direct measurement of the free energy landscape for defect annihilation pathways.[111-113] *In situ* thermal annealing has also been used to track self-healing and flow of polymer in response to mechanical damage. An AFM probe was used to scratch the polymer film and its subsequent recovery was observed. The re-emergent BCP patterns Ire found to conform with the orientation of the neighboring undisturbed pattern.[114] Recent advancements in HS-AFM during thermal annealing have expanded the range of accessible BCP dynamics. High-speed imaging has been used to study the initial stages of microphase separation and lamellar formation from a spin-coated film.[115] It has also been applied to track the conversion of a metastable "stitched" morphology templated by a chemically-patterned substrate (chemoepitaxy) to its final aligned geometry.[58,116] In these systems, scan rates are limited by the potential for sample damage of the heated polymer melts rather than the AFM imaging capabilities. In addition to measuring morphological evolution, high-speed, temperature-controlled AFM has been used to track fluctuations of the PS/PMMA interface of confined BCP cylinders in real time, shown in **Figure 1.6**.[117] Disabling of the AFM slow-scan axis allowed for rapid sampling of one-dimensional phase profiles to monitor equilibrium fluctuations of the interfacial boundary, sacrificing one spatial dimension for a dramatic increase in time resolution. Fluctuations of the cylinder edges, placements, and widths Ire found to be spatially coherent over multiple domains due to the chain connectivity and incompressibility of the blocks and Ire enhanced with increasing measurement temperatures.

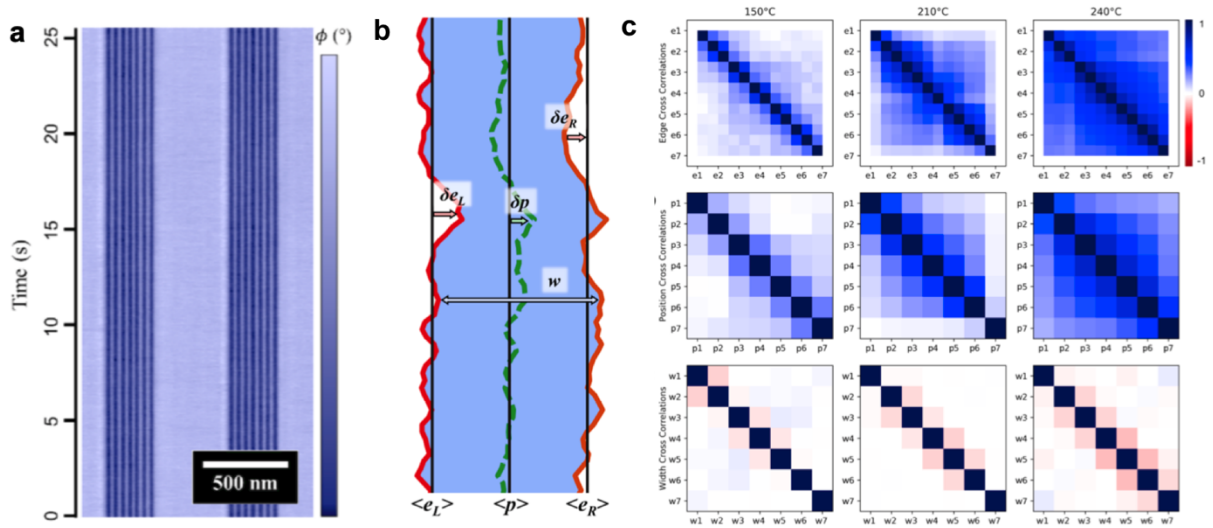

Figure 1.6 Slow-Scan Disabled AFM. (a) Slow-scan disabled (SSD) AFM phase image of cylinder-forming PS-b-PMMA confined in lithographic channels. In SSD imaging, the *x*-axis is displacement and the *y*-axis is time, allowing direct tracking of the displacement of polymer cylinders in real time. (b) Schematic depiction of fluctuations of polymer cylinder edges ($\delta e_{L/R}$), placement (δp), and width (δw). (c) Pearson correlation coefficient plots showing coherence in cylinder fluctuations, propagating throughout the channel for edge and placement fluctuations, and anticorrelation for width fluctuations, extending only to adjacent cylinders. Reproduced with permission from J. G. Raybin, J. G. Murphy, M. Dolejsi, S. J. Sibener, *ACS Nano* **2019**, *13*, 11741–11752.[117] Copyright 2019 American Chemical Society.

Recent advancements in AFM-IR have achieved nanoscale chemical contrast of BCP patterns. With 10 nm spatial resolution, IR s-SNOM measurements of PS-b-PMMA Ire sensitive to sample volumes containing ~10^4 carbonyl oscillators. In these measurements, the PMMA carbonyl stretch was found to redshift at the center of PMMA-enriched domains due to the changing dielectric environment.[118] As a complementary method, PiFM imaging was used to generate complete multispectral maps of PS-b-PMMA and PS-b-P2VP patterns,[119] and has also been performed in combination with nanomechanical mapping, correlating chemical composition with nanoscale material properties.[120]

1.3.3. Polymer Electronics

Conductive polymers are useful for organic electronic devices due to their compatibility with low-cost and low-energy fabrication processes.[121] Among their applications, polymer-based systems can be used for solar cells, light-emitting diodes, memory storage, and bioelectronic devices. The active layer of these devices typically consists of a donor/acceptor blend with large interfacial areas to facilitate charge separation. The performance of these blends depends on their nanoscale morphology, including the domain size, domain connectivity, degree of separation and electrode contact area. In turn, the heterogeneous film structure is strongly dependent on its processing history. For example, blend films form different as-cast structures when deposited from different solvents.[122]

AFM topographic mapping alone is insufficient for characterizing these blend morphologies, as compositional domains can be observed as either concave and convex features even within the same image.[123] For this reason, electrical AFM methods are used to correlate functional material properties with the local material structure: C-AFM measures current flow through conductive pathways, providing information on through-film connectivity and local mobility; KPFM maps the surface potential, providing information on molecular energy levels and charge trapping; and photoconductive AFM (PC-AFM) measures charge generated from light exposure.[36,121] Local mobility measurements often significantly exceed bulk mobility measurements obtained using parallel plate electrodes, as the 3D tip-substrate geometry samples current from an extended effective surface region. Corrections accounting for these space charge effects yield mobilities in good agreement with macroscopic measurements, but with nanoscale spatial resolution.[124]

By measuring current flow through polymer films, C-AFM can determine whether surface domains extend through the entire film thickness to the underlying electrode. Measurements of P3HT/PVDF-co-PTrFE blends found that at low P3HT loading, the majority of domains observed at the surface did not form conductive columns. Comparative KPFM measurements, which sampled the surface potential to a depth of 100 nm of the same films mapped the subsurface domain connectivity. As the P3HT fraction was increased, domains formed large interconnected networks and correspondingly greater through-film conduction.[123] Similarly, Daviddi et al. found that, in blends of P3HT:PMMA, the P3HT forms conductive islands in a surrounding insulating PMMA matrix. The C-AFM measurements, shown in **Figure 1.7**, indicate that the conductivity of the islands is not uniform, with the larger domains tending to have a higher measured current.[125] C-AFM measurements show continuous conductivity gradients across domain boundaries, indicative of blend intermixing.[126] In polymer solar cells, the intermixed donor/acceptor region is important for charge generation, but has poor mobility and can also contribute to quenching.[122] The width of the boundary region narrows with increasing annealing temperature and more complete phase separation.[126]

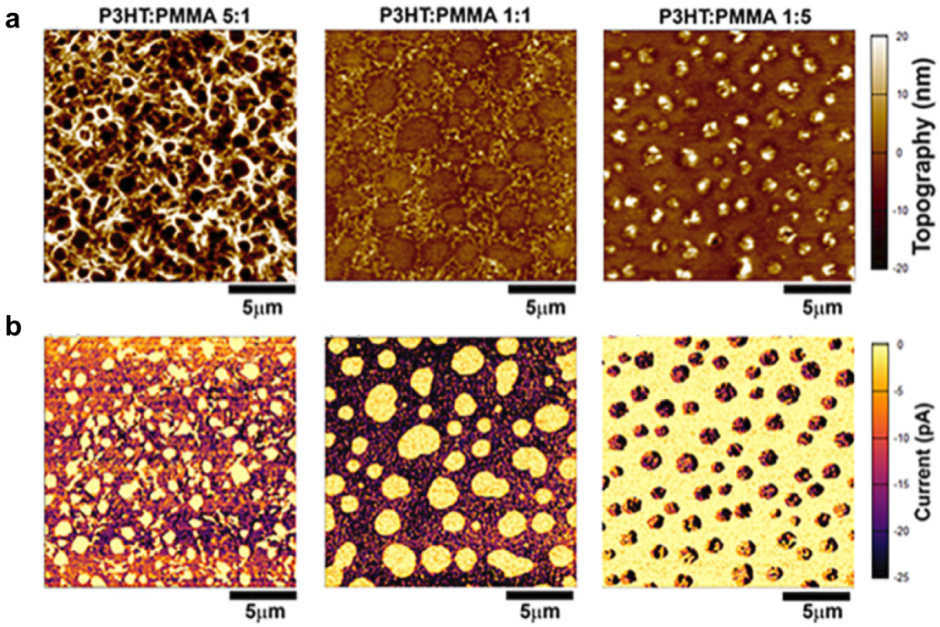

Figure 1.7 Conductive AFM. C-AFM (a) topography and (b) current images of P3HT:PMMA blend films of various blend ratios. Areas of higher topography correspond to areas of higher current, indicating the formation of conductive P3HT islands in an insulating PMMA matrix. Reproduced with permission from E. Daviddi, Z. Chen, B. Beam Massani, J. Lee, C. L. Bentley, P. R. Unwin, E. L. Ratcliff, *ACS Nano* **2019**, *13*, 13271–13284.[125] Copyright 2019 American Chemical Society.

Beyond structural characterization, with external illumination AFM can be used to measure photogeneration and degradation processes during device operation.[127] Significant variations in measured photocurrent have been observed within topographically indistinguishable domains.[128] Fluctuations in the photocurrent are associated with charge trapping and detrapping events in disconnected minority inclusions within phase-separated domains.[129] Combined heating and light exposure has been used to study photodegradation processes in polymer:fullerene blend films. These films undergo competing dimerization and decomposition (de-dimerization) processes when exposed to light and high temperatures, respectively. The AFM studies, shown in **Figure 1.8**, focused on PS:PCBM thin films as a model system and revealed that, above the glass transition temperature, pre-exposure to light reduces structural coarsening, indicating that the light-induced dimerization imparts stability to the system.[130]

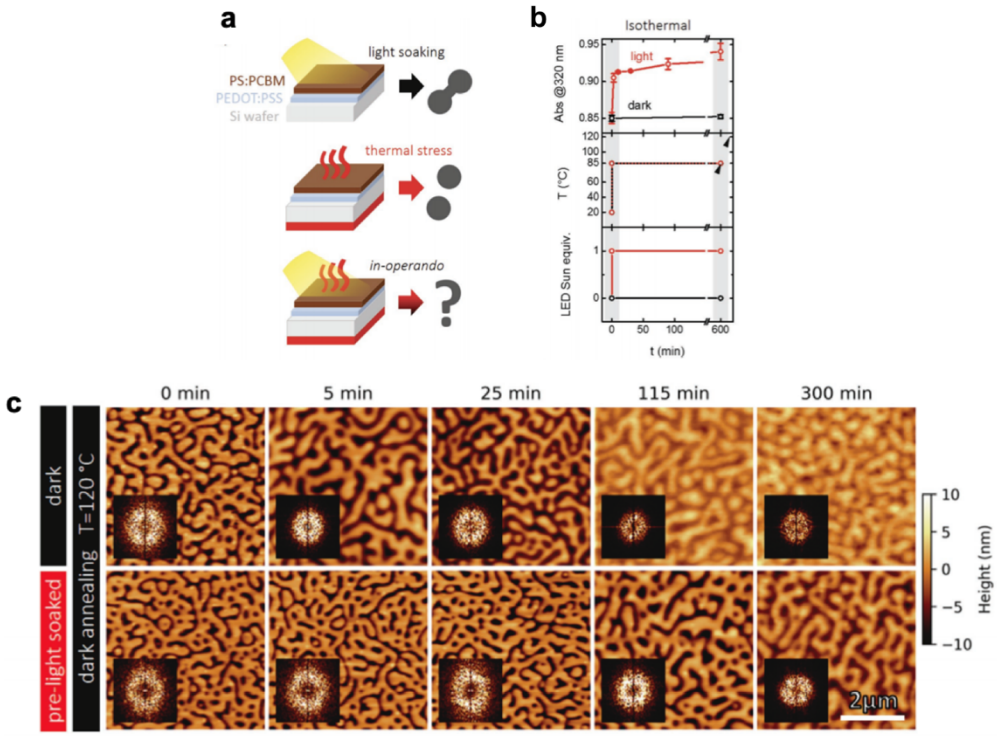

Figure 1.8 Photogeneration and Degradation in Polymer Blends. (a) Schematic illustration of the experimental setup to investigate the impact of light on polymer:fullerene blends in (b) isothermal imaging conditions with (red) and without (black) pre-illumination. (c) AFM topography images of polymer blend films annealed at 120 ºC over time, with and without pre-illumination. Films not previously illuminated (top row) have rapid coarsening, while pre-illuminated films (bottom row) exhibit limited structural coarsening in the same period of time. The 2D Fourier transform insets indicate a spinodal structure. Adapted under Creative Commons Attribution 4.0 International License (http://creativecommons.org/licenses/by/4.0/) from S. Pont, F. Foglia, A. M. Higgins, J. R. Durrant, J. T. Cabral, *Adv. Funct. Mater.* **2018**, *28*, 1802520.

1.3.4. Membrane Transport

To keep up with increasing demands for clean water, improvement in filtration methods is needed for water purification with improved energy efficiency, greater selectivity, and lower fouling. Polymer phase-inversion membranes are widely used due to their low cost and straightforward production. Next-generation membranes based on the self-assembly of block copolymers achieve narrow pore size distributions, high porosities, and controllable surface properties and chemistries. The synthesis of these membranes is beyond the scope of this Chapter, but several recent reviews cover this topic,[131-134] as well as many literature

examples.[135-143] AFM is commonly utilized to nondestructively characterize membrane topography, including pore size, shape, and size distribution, at a local level, as well as to understand membrane behavior in solvent environments.[144-146] In addition, AFM phase imaging has been used to determine the relative hydrophobicity or hydrophilicity of a membrane sample[147] and to distinguish between new and fouled membranes.[148]

Further advances in AFM techniques offer the potential to gain insight into the behavior of membranes in environments that mimic their operating conditions. In particular, combining scanning electrochemical microscopy (SECM) with AFM offers the unique ability to characterize polymer membranes, including localized sensitivity, flux, and fouling. SECM, first introduced by Allen Bard in 1989,[149] is a scanning probe technique that measures local surface electrochemical properties by monitoring redox reactions at the imaging probe. A major limitation in SECM imaging is that the tip is held at constant height as it scans the sample surface, such that the resulting measurements are a convolution of current and topography. Combined SECM-AFM was subsequently introduced[150] to decouple these signals.[151-153] This combined imaging technique has been demonstrated as a method for imaging porous surfaces and membranes, as well as measuring transport through membranes.[154-156] The work of Gardner et al. in particular highlights the potential value in using SECM-AFM to characterize membranes *in situ*. They investigated iontophoretic transport through track-etched polyethylene terephthalate (PET) membranes and saw that not all pores identified in topography images contributed to ion transport and found significant transport heterogeneity across active pores, highlighting the added value of localized transport measurements.[157]

1.3.5. Solvation and Swelling

Many polymer applications, including drug delivery, lithographic etching, and molecular signaling, require the use of polymer films or brushes in liquid environments. However, when submerged in liquid, the polymer matrix swells, altering the polymer morphology, ordering, and self-assembly, particularly if the system is a BCP or polymer blend with differential solvent compatibility. Solvent-responsive polymers can be engineered to utilize these changes for desired functionality. Deswelling of the polymers after removal from the solvent can further alter the surface structure as the swollen chains collapse and enter a kinetically trapped state. The ability to image in liquid environments makes AFM a particularly powerful tool for investigating native swelling dynamics as well as programmed responses.

Lai et al. investigated polyacrylamide (PAAm) hydrogels to validate the use of Flory-Huggins theory, which describes the thermodynamics of polymer mixing, for modeling swollen polymeric materials.[158,159] They used dynamic oscillation indentation AFM to measure various poroelasticity metrics (including shear modulus, Poisson's ratio, and diffusivity) submerged in aqueous polyethylene glycol (PEG). These experiments showed that the large volume change and accompanying stretching of the polymer chains renders Gaussian statistics insufficient to model stretched chains in swollen polymer films, and demonstrated that the deformation mechanism cannot be fully explained by Flory-Huggins theory. The authors proposed a series of equations to modify the swelling model and explain the observed behavior.[160] Our lab has used *in situ* AFM to investigate the swelling of terraced PS-b-PMMA thin films when submerged in cyclohexane. Solvent was observed to infiltrate along step-edges and propagate uniformly through polymer terraces. Solvation kinetics are limited by relaxation of the glassy polymer chains at the swelling front, as shown in **Figure 1.9**.[161] In addition to impacting the ordering or

phase separation of polymer films, solvent-induced swelling can also lead to degradation of the polymer backbone. Messmer et al. investigated the solvation-induced main-chain scission in dendronized polymers, utilizing AFM topography along with molecular dynamics simulations to decipher the scission mechanism in charged and neutral dendronized polymers. They find that solvent-induced scission is due to sterically-induced degradation, that is internal mechanical stress caused by swelling in the dendritic periphery, as opposed to external stressors (e.g., reactants, temperature instability, etc.).[162] These findings provide further evidence that dendronized polymers can be thought of as colloidal particles, rather than classical linear polymers, in solution.[163]

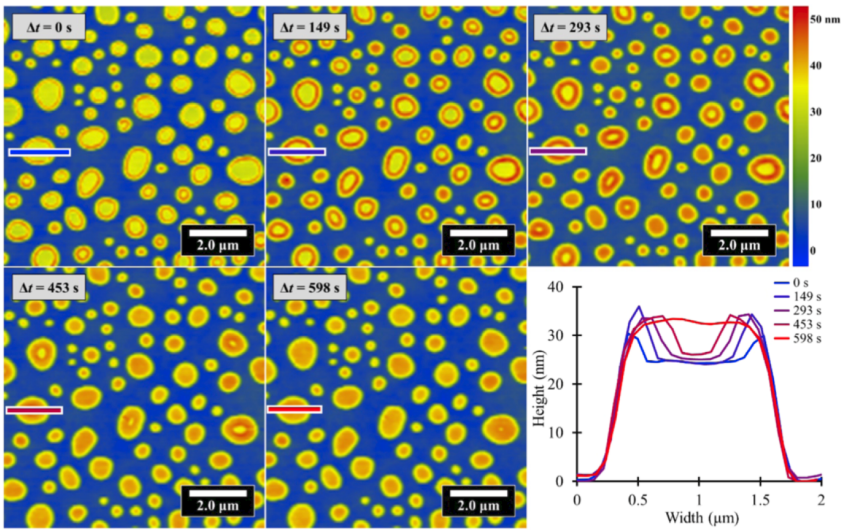

Figure 1.9 Solvation Kinetics in Swollen Films. Time series of PS-PMMA islands immersed in cyclohexane tracking the solvation process. A sharp swelling front separating the solvent-swollen melt from the unsolvated glass propagates from the island edges. Height profiles show the time-evolution of island swelling. Reproduced with permission from J. G. Raybin, S. J. Sibener, *Macromolecules* **2019**, *52*, 5985–5994.[161] Copyright 2019 American Chemical Society.

Controlled polymer swelling can favorably alter the morphology and functionality of polymer films, for example altering the surface roughness or adhesive properties. Jalili et al. demonstrated that the roughness of polymer brushes can be manipulated by exposing the brush to good or poor solvent environments. They imaged morphology changes in PHEMA brushes on

PDMS substrates when the substrates Ire submerged in water and cyclohexane, good and bad solvents, respectively. When exposed to a good solvent, AFM imaging revealed a swollen needle-like morphology structure with a uniform surface roughness, while exposure to a poor solvent led to collapse of the polymer film and a carpet-like morphology. Additionally, the PHEMA brush becomes more hydrophobic when exposed to varying degrees of ultraviolet/ozone treatments and the surface roughness decreases with longer exposure times.[164] Controlled polymer swelling also has important implications for creating antifouling surfaces in relation to marine applications, e.g. preventing barnacle adhesion on ships.[165,166] A recent paper in this area utilized colloidal AFM-based force spectroscopy to investigate the response of methacrylamide- and styrene-based sulfobetaine polymer brushes, PSBMAm and PSBVB, respectively. Comparison of the nanomechanical and adhesive properties in water, salt water, and deuterium water revealed that the methacrylamide-based films have lower adhesion forces to surfaces, due to the stronger hydration of these brushes in the high-ionic-strength media.[167]

1.4. Conclusions and Outlook

AFM has become an indispensable tool for both fundamental polymer physics and functional applications research due to its unique capacity for multifunctional characterization and imaging. AFM imaging has highlighted the rich complexity and heterogeneity of polymers at the nanoscale: It has helped elucidate mechanisms of polymer ordering, phase separation, and crystallization, as well as correlated nanoscale structures to functionality in relation to membranes and electronics applications. In this Chapter, I have highlighted some of the current and forefront polymer issues using AFM to study the function and structure of polymer films. Ongoing developments in AFM technology, including high-speed, high-resolution, and

multiparametric imaging, with improved environmental controls for *in situ* temperature and solution imaging, continue to provide insight into polymer dynamics and interactions under real world conditions. As new and increasingly complex polymer materials are continually designed, I may anticipate that, in the future, the unique capabilities of AFM will help resolve outstanding issues and guide the formulation of new questions at the frontier of polymer science.

Chapter 2.

Spatiotemporal Mapping of Hole Interaction Dynamics during Block Copolymer Terracing with High-Speed Atomic Force Microscopy

As a platform for investigating two-dimensional phase separation, we track the structural evolution of poly(styrene-*block*-methyl methacrylate) thin films during thermal annealing with environmentally controlled atomic force microscopy (AFM). Upon thermal annealing, a block copolymer film with incommensurate thickness separates into a terraced morphology decorated with holes. Using high-speed AFM imaging, we directly observe the complete hole formation process, beginning from nucleation and continuing through late-stage coarsening. Analysis of the growth statistics from time series AFM images reveals homogeneous nucleation and growth consistent with classical nucleation theory. At later times, we find that hole coarsening is driven by the combination of both Ostwald ripening and coalescence. By visualizing the real-space mechanism for each coarsening process, we determine their relative contributions and resolve the anomalous scaling behavior of BCP terrace growth.

2.1 Introduction

Across a diverse array of phenomena, activated phase transformations follow a consistent progression, featuring nucleation and growth at early times, followed by coarsening at late times. The evolution between these stages is a continuous process governed by a common set of thermodynamic relationships.[1] As described by classical nucleation theory (CNT), homogeneous nucleation events arise when localized fluctuations of the emerging phase exceed a threshold size, described by the critical radius, R_C. Fluctuations with radius $R < R_C$ are unstable and short-lived, as the energy penalty of the interface (which scales as R^2 in 3D or as R in 2D) out-competes the favorable bulk energy of the new phase (which scales as R^3 or R^2, respectively). Droplets with $R > R_C$ grow over time, driving phase conversion until the system attains its equilibrium composition. At that stage, further reduction in free energy may be achieved by shrinking the interfacial area between phases through a droplet coarsening mechanism known as Ostwald ripening. As described by Lifshitz, Slyozov, and Wagner, each droplet maintains local equilibrium through the exchange of material with its surroundings, following the same detailed balance considerations as CNT.[2,3] Similar models have been developed that extend this description to 2D systems.[4] This capillarity-driven process results in the net transfer of material from smaller high-curvature droplets to larger low-curvature droplets. Over the same period, binary collisions between droplets can also lead to their coalescence, which contributes as an additional coarsening mechanism. Together, these processes, which have each been thoroughly examined through theory, simulation, and experiment, provide a consistent model for understanding phase transformations. [5-7]

Block copolymer (BCP) thin films have frequently served as 2D platforms for studying nanoscale phase dynamics.[8,9] Due to their native ability to self-assemble into ordered

nanopatterns, BCPs form structured films with a natural length scale L_0.[10,11] At equilibrium, thin-films therefore adopt integral thicknesses τ, such that:

$$\tau = \frac{1}{2} n L_0 \; ; \; n = 1,2,3,4,\ldots \qquad \textbf{(2.1)}$$

For films deposited on a solid substrate, both symmetric and anti-symmetric wetting conditions can occur depending on the affinity for each block with both the free and confined interfaces. In the case of symmetric wetting (*n* even), the same block presents at both interfaces, whereas for anti-symmetric wetting (*n* odd) a different block wets each surface. When the thickness of a deposited film is incommensurate with L_0, *i.e.,* for non-integer values of *n*, a terraced surface structure forms to enforce local commensurability. The initially disordered morphology undergoes phase separation into regions of upper and lower terraces, where thickness serves as a globally conserved order parameter. This phase separation has been observed to occur *via* either nucleation and growth or spinodal decomposition mechanisms, where the activation barrier for terracing is dependent on the initial film thickness.[1,12,13]

The dynamics of BCP terrace formation have previously been investigated through both *in situ* and *ex situ* methods.[14-18] Previous studies relying on neutron reflectometry, ellipsometry, and X-ray scattering have followed the *in situ* progression of phase separation but are limited to measurements of spatially averaged film properties. Optical microscopy has been used to track mesoscale terrace dynamics, but diffraction-limited resolution prevents nanoscale characterization. Real-space imaging methods using atomic force microscopy (AFM) or scanning electron microscopy have also probed terrace formation but have previously been limited to *ex situ* measurements due to the demanding high-temperature annealing conditions. Although these methods are sufficient for capturing statistical properties of the transition, they are unable to follow terrace evolution continuously over time. More recently, advances in

environmentally-controlled and high-speed AFM have now enabled localized imaging of dynamic systems in real space and time under annealing conditions. Improved imaging stability has also facilitated continuous imaging of a single region over hour-long timescales necessary to track terrace formation.

Here, we directly observe the nucleation and growth of holes in terraced poly(styrene-*block*-methyl methacrylate) (PS-*b*-PMMA) thin films. Starting from an initially disordered film morphology, we use environmentally-controlled AFM to heat the samples above the glass transition temperature and observe the phase separation to a terraced equilibrium state. These experiments capture the full temporal range of the transition, starting from the earliest stages of nucleation and growth and following through to late-stage coarsening. Through analysis of the growth statistics from these images, we see homogeneous nucleation and growth of the holes consistent with the expectations of CNT. At later stages, we find that coarsening occurs *via* a combination of simultaneous Ostwald ripening and coalescence mechanisms. In each case, real-space imaging reveals interactions between holes, mediated through either the interconnected terrace or binary merger events. Together these observations provide an explanation for anomalous power-law exponents in measurements of BCP terrace growth kinetics.

2.2 Approach

Here, we study a cylinder-forming PS-*b*-PMMA thin film. The BCP has a molecular weight of 77 kg/mol with a 71 w. % PS composition resulting in L_0 = 45.5 (± 0.4) nm, as determined through measurement of the pattern periodicity (shown in the **Figure SI.2.1**). The polymer is spin-coated from toluene onto an unpatterned silicon wafer substrate, with an incommensurate average thickness of τ = 30.0 ± 0.2 nm measured by ellipsometry. The as-cast

film morphology is far from equilibrium but is kinetically quenched, preventing terrace formation at room temperature. The film thickness falls in the range $\frac{1}{2}L_0 < \tau < L_0$, such that the final structure after thermal annealing phase separates into commensurate holes with local thickness $\frac{1}{2}L_0$ and terraces with local thickness L_0.[10,11] A 3D perspective of the terraced topography of an annealed incommensurate film is shown from two angles in **Figure 2.1a** with an overlaid phase color map. AFM phase imaging is sensitive to variation in the viscoelastic tip-surface interaction, providing contrast between PS and PMMA domains. In this image, the lower terrace ($\frac{1}{2}L_0$) shows uniform PS coverage, while the upper terrace (L_0) is decorated by PS and PMMA stripes, indicative of BCP cylinders oriented parallel to the substrate. In the layered equilibrium film structure state, there is an initial $\frac{1}{2}L_0$ wetting layer where PMMA preferentially wets the silicon substrate, and PS is presented at the top surface. Because PS and PMMA have similar affinities for the air interface, in subsequent layers of cylinder-forming PS-*b*-PMMA the top surface presents a characteristic striped morphology including domains of both components.

Starting from an as-cast BCP film, we use environmentally-controlled AFM to continuously image the terracing process. The film is heated *in situ* to 200 °C with a temperature ramp of 1 °C/s immediately prior to AFM imaging. In topography images, holes are observed to nucleate and grow over the course of imaging for roughly 2 h with a 26.2 s/image time resolution. Because we are primarily interested in mesoscale terrace dynamics, we image over a wide 20 μm × 20 μm field of view where we do not resolve the striped BCP pattern. The time series AFM data tracking hole formation is shown in **Figure 2.1b** and the full movie is included as Supporting Information. The hole area fraction over time is defined $\Phi(t) = A_h(t)/A_{tot}$ where

$A_h(t)$ is the hole area at time t and A_{tot} is the total imaging area. Following the lever rule, the film approaches an equilibrium hole coverage of:

$$\Phi_{eq} = 2\left(1 - \frac{\tau}{L_0}\right) \qquad \textbf{(2.2)}$$

corresponding to an expected value of $\Phi_{eq} \sim 0.66$ for this system. We see the initial nucleation of the $\frac{1}{2}L_0$ level that grows isotropically over time, resulting in formation of circular holes within an interconnected terrace. The relative terrace height measured in AFM is 19.8 ± 1.8 nm consistent with a $\frac{1}{2}L_0$ height difference (**Figure SI.2.2**). When holes grow into the same area, they coalesce – often multiple, consecutive times – forming complex, irregular shapes. Continued growth of coalesced holes causes them to become rounder over time to minimize interfacial line tension. AFM scratch tests following the *in situ* experiment, find a height of 44.2 ± 1.8 nm of the upper terraces over the silicon substrate confirming the $\frac{1}{2}L_0$:L_0 terrace structure.

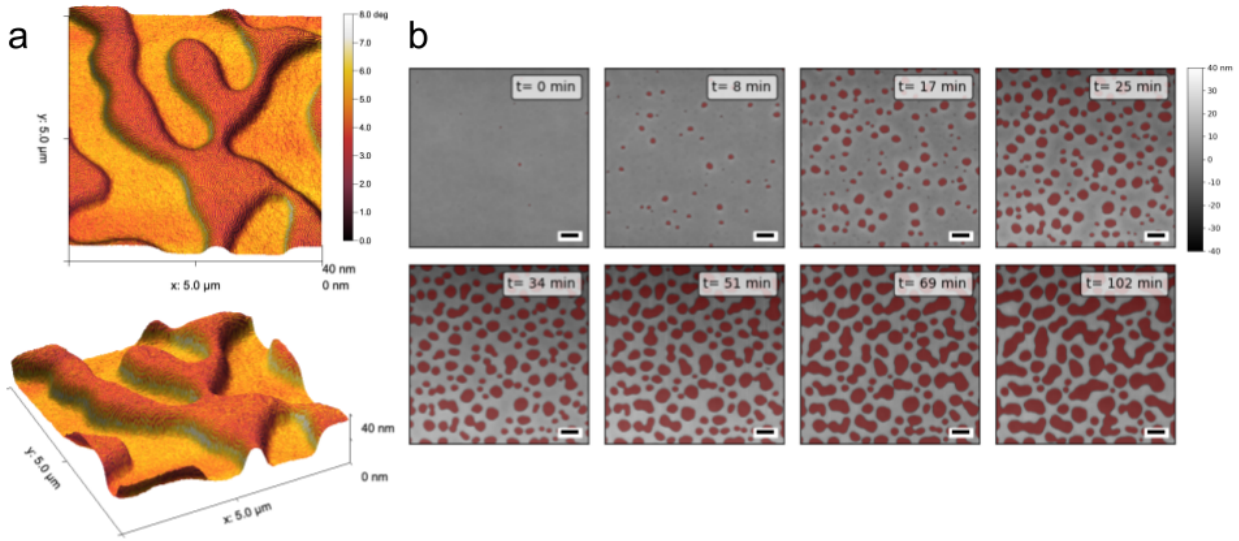

Figure 2.1. Terraced Film Morphology. (a) 3D perspective of the terraced PS-*b*-PMMA thin film topography, colored according to an overlaid AFM phase image to show compositional contrast. The holes regions have uniform PS coverage at the air interface, while both PS and PMMA domains are present in the upper domains, resulting in a striped fingerprint pattern. (b) Time series AFM images showing the hole evolution over time. Nucleation sites are visible at the earliest imaging times, and these sites grow and merge over time. Hole regions are colored in red.

2.3 Results and Discussion

2.3.1 Ensemble Kinetics

Over the course of thermal annealing, the BCP film follows a progression of stages on the road to equilibrium: (1) induction, (2) nucleation, and (3) coarsening. Each stage follows different growth kinetics and mechanisms and is therefore analyzed separately. Through each period, we track the appearance and development of holes over time, as displayed in **Figure 2.2** on a logarithmic time scale – including **(a)** the total hole surface coverage $\Phi(t)$, **(b)** the average area per hole $\langle A(t) \rangle$, **(c)** the number density of holes $N(t)$, and **(d)** the average hole growth rate $\langle dR/dt \rangle$. The same data plotted on a linear time scale are in **Figure SI.2.3**. For this analysis, we exclude holes touching the image boundary. In determining the growth rate, the area of each hole is related to an effective radius as $A = \pi R^2$, assuming circular holes, and the average growth rate is then calculated from the frame-to-frame change in radius for each hole.

At the beginning of AFM imaging, we observe a delay period prior to the onset of steady-state nucleation. This induction stage, highlighted in gray in **Figure 2.2**, has been previously described for BCP terracing and is indicative of an activation barrier for nucleation.[19] We capture only a portion of the full induction time following the initial AFM temperature ramp, due to the need for thermal equilibration before imaging. After the sample chamber reaches its setpoint temperature, the cantilever resonance changes and must be redetermined under the new thermal equilibrium.[9] Altogether, the polymer film is held above its glass transition temperature for approximately 5 min prior to imaging, and the first AFM image, shown **Figure 2.1b**, therefore already includes sparse features distributed over the surface.

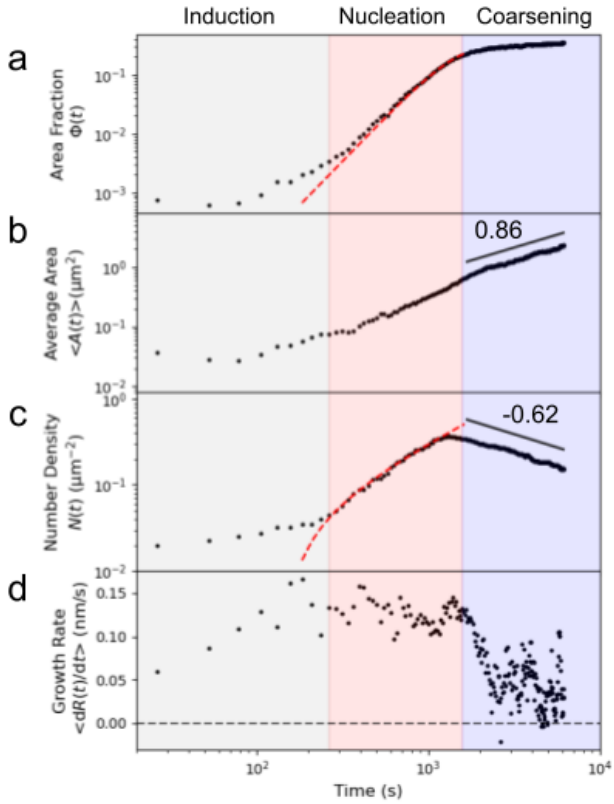

Figure 2.2. Ensemble Hole Growth Statistics. Plots over time of the (a) total hole surface coverage $\Phi(t)$, (b) average area per hole $\langle A(t)\rangle$, (c) number density of holes $N(t)$, and (d) average hole growth rate $\langle dR/dt\rangle$. Three distinct periods are observed as the system progresses to equilibrium: induction (gray), nucleation (red), and coarsening (blue). The red-dashed line in (a) shows a fit to the Avrami equation **(3)** with fixed Avrami exponent $d = 3$ for 2D nucleation and growth. The red-dashed line in (c) shows a linear regression to $N(t)$ over the same period. The black trendlines in (b) and (c) show power-law scaling with the indicated exponents for the average area and number density during late-stage coarsening, respectively.

Following induction, the film enters the steady-state nucleation regime, displayed in red in **Figure 2.2**. As a measure of terracing kinetics, we apply Avrami analysis to quantify the hole area fraction $\Phi(t)$ **(Figure 2.2a)** following:

$$\Phi(t) = A_\tau\,[1 - \exp(-Kt^n)] \qquad \textbf{(2.3)}$$

where A_τ is the area fraction of holes at the end of the nucleation stage, K is the Avrami constant, and n is the Avrami exponent. The Avrami equation **(2.3)** describes the kinetics of phase transformations in the case of homogeneous nucleation and constant, isotropic growth. Under

these assumptions, the Avrami exponent is related to dimensionality d of the growth process as $n = d + 1$, and, therefore, in our system $n = 3$. The red dashed line in the nucleation stage of **Figure 2.2a** corresponds to a least-squares fit of **(2.3)** with fixed $n = 3$, showing close agreement with the observed change in area fraction over this period. Throughout this period, we find that new holes are uniformly distributed in space and show a linear increase in number density over time, as indicated by the linear fit in **Figure 2.2c**. We also observe conformal hole growth that maintains roughly circular hole shapes with a constant radial growth rate of 1.2 (± 0.1) $\times$ 10^{-4} μm s^{-1} (**Figure 2.2d)**. Altogether, these observations are consistent with the expected kinetics for homogeneous nucleation under CNT.

The end of the nucleation period, highlighted in blue in **Figure 2.2,** is identified by a slowdown of the terracing process. This transition marks the onset of late-stage coarsening, which is typically characterized by power-law scaling behavior. At this point new holes stop forming and existing holes begin to disappear, as evidenced by a turnover in N (**Figure 2.2b**), which decreases following $N \propto t^{\beta}$. At the same time, individual holes continue to grow and $\langle A \rangle$ increases following a power law $A \propto t^{\gamma}$ (**Figure 2.2c**). In cases where Φ is constant, the power-law exponents are related such that $\beta = -\gamma$.[20,21] The discrepancy between these measured exponents, with β = -0.62 and γ = 0.86, is indicative of ongoing growth of the total hole coverage.[4] In fact, at the onset of coarsening, the hole fraction reaches a coverage of Φ = 0.21, still far from the expected equilibrium of $\Phi_{eq} = 0.66$. Although terracing slows significantly in this regime, the average hole growth rate remains positive (**Figure 2.2d**).

The identification of power-law exponents is traditionally used to distinguish coarsening mechanisms.[16,22,23] For example, in the case of 2D Ostwald ripening, coarsening scales as $R \propto t^{1/3}$, and measurements of hole area correspondingly follow $A \propto R^2 \propto t^{2/3}$. Meanwhile,

scaling-laws for coalescence are predicted to follow a range of exponents, from $t^{1/4}$ to t^{1}, depending on the precise character of hole transport. The observed $A \propto t^{0.86}$ scaling obtained from ensemble statistics, however, does not unambiguously establish a single coarsening mechanism. Instead, through direct observation of the growth process, we see that the coarsening process occurs *via* two simultaneous mechanisms: Ostwald ripening and coalescence. Each process contributes to hole growth and decreases the total number of holes in the system – ripening through the evaporation of small holes and coalescence through hole merger events. The observed power-law exponents consequently reflect a combination of both concurrent mechanisms. Each of these coarsening processes will be discussed in more detail below.

2.3.2 Hole Nucleation and Growth

To better understand the growth process, we follow the evolution of an individual hole over time, from its initial nucleation and through the coarsening process. The time series AFM images and corresponding line profiles of the individual hole are displayed in **Figure 2.3a-b**. At the earliest imaging times, we already see evidence of an initial depression in the polymer film. This nucleation site develops into a conical divot, with the depth increasing over time until reaching a commensurate half-layer thickness. From there, the hole continues to expand laterally and isotropically, such that its center-of-mass position remains stationary. As the hole expands, a halo of excess material appears around the rim during the initial growth stage. Halo formation is indicative of subsurface restructuring into a layered morphology, propagating from hole edges.[15,24] Similar halos form around neighboring holes, which grow and join together until the surrounding terrace reaches a uniform commensurate thickness. The observed leveling of the outside terrace line profile coincides with the onset of the coarsening stage. At this point, the

hole continues to grow laterally, but at a slower rate. Eventually, following this image sequence, the growing hole impinges on neighboring holes and they coalesce.

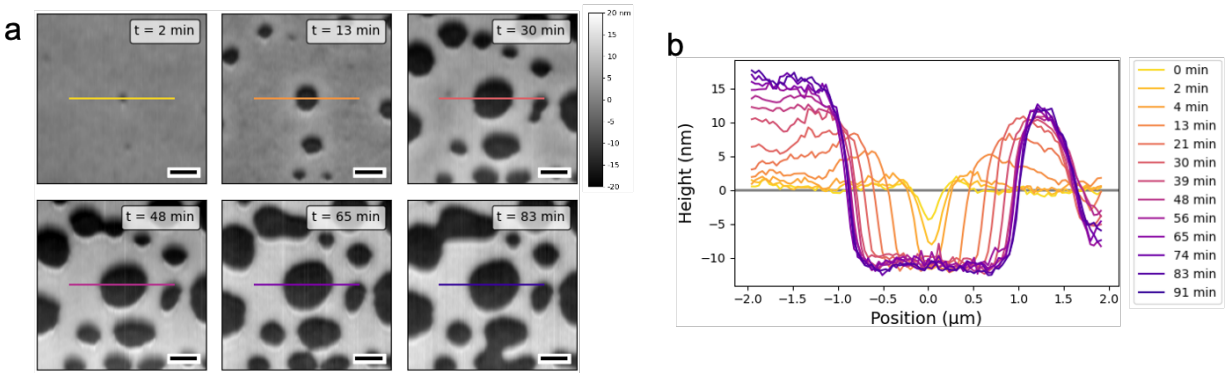

Figure 2.3. Nucleation and Growth of an Individual Hole. (a) Time series AFM images tracking the growth of a single hole with (b) the corresponding topographic line profiles. The initial nucleation site grows down to a conical divot and then expands laterally, and an elevated halo around the hole propagates outward over the surrounding terrace.

Hole nucleation and growth is driven by equilibration of the BCP film, which is initially unstable due to the incommensurability of the film thickness. The first stages of hole formation yield a commensurate $\frac{1}{2}L_0$ thickness within the hole, while the surrounding terrace remains incommensurate. Therefore, a chemical potential gradient is established between the hole edges and the surrounding polymer-depleted terrace, driving the migration of polymer chains. Detachment of polymer chains from the hole edge exceeds the rate of chain diffusion within the terraces, leading to local buildup of excess polymer that forms the halo.[15,16] As the surrounding terrace thickness becomes uniform, the chemical potential stabilizes over the film surface and reaches a steady-state.

2.3.3 Ostwald Ripening and Hole Coalescence

Following the steady-state nucleation period, real-space imaging reveals concurrent Ostwald ripening and coalescence mechanisms leading to droplet coarsening. To understand the

separate contributions of these mechanisms, we now examine each of these processes in more detail.

During Ostwald ripening, holes maintain equilibrium with the surrounding terrace environment through the exchange of individual polymer chains at the hole edges. As part of this process, hole coarsening proceeds through an evaporation-condensation mechanism involving the net transfer of material from small high-curvature holes to large low-curvature holes. Accordingly, alongside instances of hole growth, we also observe cases where smaller holes shrink and disappear. As an example, a time series showing the formation and subsequent disappearance of a hole is shown in **Figure 2.4a**. During the initial nucleation and growth period, the hole grows along with its neighbors. At the onset of coarsening, the hole area then plateaus and begins to decrease before completely vanishing, as shown in **Figure 2.4b**.

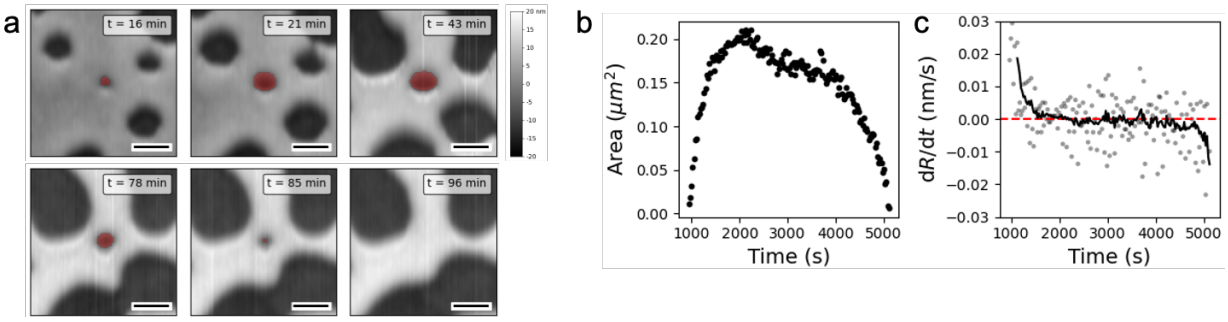

Figure 2.4. Ostwald Ripening and Hole Evaporation. (a) Time series AFM images of the disappearance of a hole (red) due to Ostwald ripening. (b) Plot of the area of the highlighted hole over time. The hole area initially increases at early times and eventually decreases at late times due to the changing critical radius, before vanishing completely.

The reversal in hole growth occurs due to changes in the local chemical potential of the surrounding environment over time. Initially, during nucleation and growth, the system is far from equilibrium and a large chemical potential gradient drives polymer chains to detach from the hole edge and flow to the surrounding terrace. As the terrace thickness stabilizes, the

chemical potential of the upper terrace region increases, leading to slower overall hole growth. Through this process, the critical radius for hole stability also increases over time, outpacing some fraction of smaller holes. Holes that fall below the critical radius, such as the one shown in **Figure 2.4a**, become unstable, shrink, and ultimately disappear as chains re-attach to their boundary.

To measure the change in critical radius, we compare the size dependence of the hole growth rate between the early-stage nucleation and growth and late-stage coarsening. From statistical analysis of the frame-to-frame change in radius of each hole, we measure the fraction of holes that grow (ρ_g) and shrink ($\rho_s = 1 - \rho_g$) as a function of radius over each stage. The net growth probability ($\rho_g - \rho_s$) initially increases from negative to positive, with the crossover marking the critical radius R_c, and stabilizes for sufficiently large holes (**Figure 2.5a**).[6,25] At late times, the difference $\rho_g - \rho_s$ is generally smaller and the crossover shifts to larger radii, consistent with slowing hole growth rates. Between these stages, the critical radius increases from R_c = 39 ± 20 nm to R_c = 137 ± 20 nm.

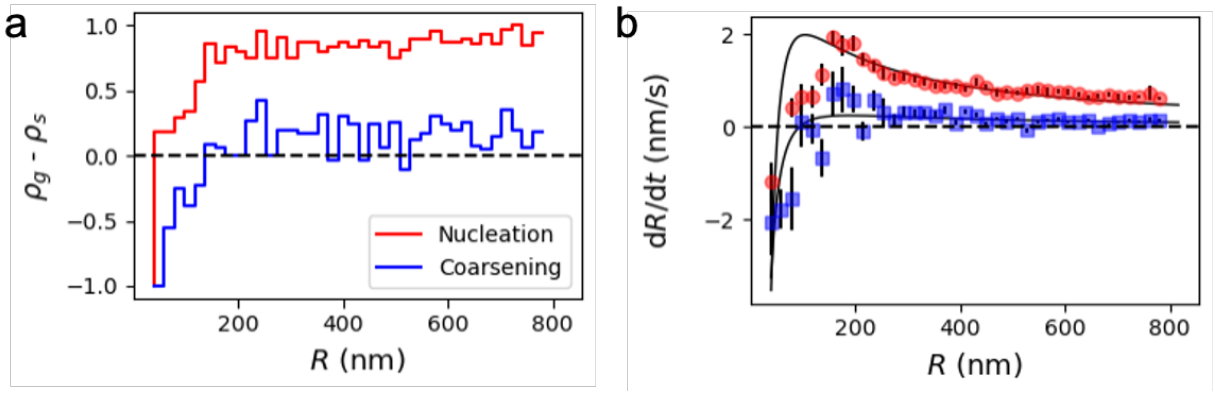

Figure 2.5. Evolution of the Critical Radius. (a) The probability difference ρ_g - ρ_s for holes to grow and shrink as a function of hole radius during nucleation (red) and coarsening (blue) periods. Growth is slower at late times, and the critical radius, which corresponds to the crossover from negative to positive, also increases. (b) Comparison of the average hole growth rate as a function of hole radius over each time period. The black trend lines show fits to equation **(2.4)**.

Similar trends are observed in plots of the average growth rate as a function of radius (**Figure 2.5b)**, with a crossover from negative to positive growth at the critical radius. The growth rate peaks shortly above the critical radius and then decreases asymptotically at large radii. As with measurements of the growth probability, the average growth rate is generally lower at late times. In the case of diffusion-controlled growth, the growth rate of an individual hole may be determined from the Gibbs-Thomson equation and follows a size-dependence:

$$\frac{dR}{dt} = \frac{K}{R}\left(\frac{1}{R_c} - \frac{1}{R}\right) \qquad \textbf{(2.4)}$$

where the K is a constant proportional to the chain diffusion constant.[26-28] Although fits to **(2.4)** recover these qualitative trends, we find significant deviation at small hole sizes. Crucially, this expression assumes conformal growth, which does not hold for non-circular holes observed at late times. Moreover, this analysis averages over both space and time within each stage and does not account for heterogeneity or changes in the local environment. Still, differences in the size-dependent growth between each stage provide statistical confirmation of the time-evolution of R_c.

Alongside Ostwald ripening, we observe discrete binary hole mergers *via* a coalescence mechanism. Coalescence events, which occur when two holes converge, become more frequent as the total hole coverage increases and often recur multiple times for a given hole. Repeated mergers give rise to the irregular, non-circular hole shapes observed at late times. One example of a hole merger is shown in **Figure 2.6a**, in which two individual holes, outlined in blue and yellow, grow into the same region of space. As the holes approach, the bridge region separating them becomes unstable, and they coalesce into a single larger hole with a peanut shape, outlined in green. At this point, hole growth becomes concentrated at the high-curvature neck due to the Gibbs-Thomson effect, and the neck widens over time until the hole recovers a circular shape

that minimizes line tension along the hole boundary. The overall terrace shape evolution is governed by a competition between this thermodynamically-favored path toward circularity and kinetically-controlled merger events.

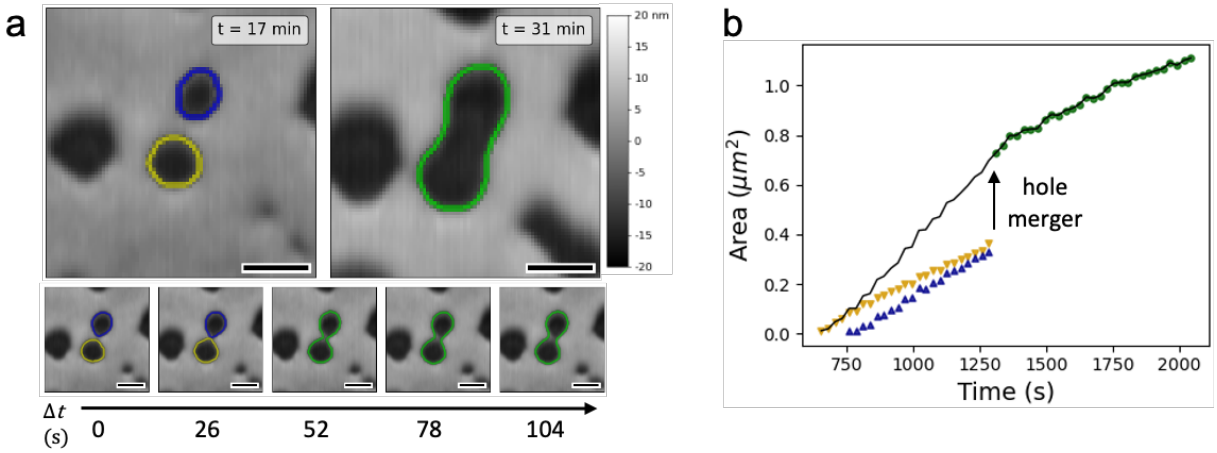

Figure 2.6. Hole Coalescence. (a) Time series AFM images capturing a merger event between two holes. The top images show the holes before (left) and after (right) coalescence, while the image series (bottom) shows the frame-to-frame progression of the coalescence mechanism through time. The perimeter of each hole is highlighted along contours of constant height. (b) Plots of the total area and area of the highlighted holes, with colors corresponding to panel (a).

We track the area of the component holes through this process in **Figure 2.6b**. This plot provides an illustration of the scaling behavior of hole growth, which slows with increasing area. The larger (yellow) hole initially grows more slowly than the smaller (blue) hole. After they merge, the total growth rate abruptly decreases due to the larger size of the new combined hole (green).

In this system, mergers occur when nearest-neighbor holes grow into each other. Over experimental time scales, we find negligible center-of-mass motion, such that hole diffusion and drift do not contribute to the coalescence rate (**Figure SI.2.4**). As two holes approach, the narrow bridge region that separates them is destabilized by the proximity of both hole boundaries. The

localized interfacial tension of this geometry establishes a pressure gradient that drives flow from narrow regions to wide regions in the interconnected phase, and, in fluid systems, the resulting hydrodynamic currents often further drive droplet motion.[29] The high viscosity of the polymer melt studied here limits long-range flow and we expect that hydrodynamic currents only disrupt the bridge locally, where curvature is highest.

The combined contributions of Ostwald ripening and coalescence together yield anomalous power-law exponents that exceed the predicted rate for capillarity-driven growth alone. Because we visualize the real-space mechanism for each process, we can distinguish discrete merger events from continuous growth due to ripening. In this manner, we consider the separate contributions of each mechanism to hole disappearance and growth during coarsening (**Figure SI.2.5**). Hole disappearance is primarily driven by coalescence, with mergers exceeding evaporations by roughly an order of magnitude. Conversely, hole growth is primarily determined by continuous ripening processes over the course of the experiment. In general, coalescence becomes increasingly significant at late times, as the increasing hole fraction shortens typical hole separation distances, and extrapolated to longer imaging times, growth due to coalescence would likely outpace ripening.

In our estimate of the separated growth rate excluding mergers, we find a power-law scaling of $A \sim t^{1/2}$, corresponding with $R \sim t^{1/4}$ and smaller than the predicted $R \sim t^{1/3}$ scaling for Ostwald ripening. This discrepancy underscores a limitation of the separation procedure. Coupling between ripening and coalescence processes introduces cross-interactions, such that the hole growth rate is not a simple additive sum. For instance, ripening dynamics are modified by coalescence due to the changing size and shape of holes. In particular, we expect that ripening is slowed, because merger events cause holes to grow larger at earlier times. Moreover, the

coalescence rate is entirely dependent on ripening kinetics, as mergers only occur when continuous growth causes neighboring holes to expand into each other. Altogether, real-space imaging reveals how the interplay between these processes contributes to coarsening dynamics.

2.4 Conclusion

We have presented real-space imaging of 2D phase separation dynamics in terraced BCP thin films with environmentally controlled and high-speed AFM. With *in situ* imaging at 200 ºC, we follow the continuous progression of terrace formation in a single region of a cylinder-forming PS-*b*-PMMA thin film, beginning with the disordered morphology on an unpatterned silicon substrate and continuing through nucleation, growth, and coarsening stages. At early times, we observe homogeneous hole nucleation and isotropic growth, with kinetics following the predictions of CNT. At later times, however, we find anomalous growth kinetics that cannot be ascribed to a single mechanism. Instead, through direct visual observation by AFM, we find that the combination of Ostwald ripening and coalescence mechanisms concurrently contribute to coarsening. In each case, our observations highlight the importance of hole interactions for determining coarsening kinetics, mediated either through the interconnected phase for Ostwald ripening, or through binary collision events for coalescence. From this analysis, we obtain sufficient statistics to track the time-evolution of the critical radius between nucleation and coarsening. The unique combination of real space imaging and analysis of growth statistics in 2D phase behavior is achieved through environmentally controlled AFM with high stability and imaging speeds, affording capture of the full temporal range of BCP film terracing.

2.5 Methods

Samples were prepared on silicon wafer substrates from Virginia Semiconductor, Inc. Wafers were cleaned by sonicating in toluene and then acetone for 5 min each, then rinsed with isopropanol and dried with N_2. Cylinder-forming PS-*b*-PMMA with a molecular weight of 77 kg/mol and 29 % PS was purchased from Polymer Source, Inc. and prepared in 0.9 wt. % solutions in toluene. The solution was spin cast onto the cleaned substrates at 3000 RPM for 60 s to obtain the desired film thickness. The average film thickness was measured on a Gaertner Waferskan ellipsometer, with an estimated index of refraction of 1.53, and found to be 30.0 ± 0.2 nm.

High-speed tapping mode AFM imaging was performed on an Asylum Research Cypher ES Environmental AFM, using FS-1500 cantilevers with 1.5-2.0 MHz resonant frequency and a setpoint of 500 mV to prevent sample damage during scanning. As-cast samples were heated *in situ* to 200 ^{o}C at a ramp rate of 1 ^{o}C/s under Ar atmosphere with gauge pressures of 30-40 mbar. Upon reaching the setpoint temperature, the cantilever resonance was redetermined prior to imaging. The sample was then imaged continuously with a line scan rate of 19.53 Hz with 512 × 512 pixel resolution over a 20 × 20 μm^2 area, giving an overall imaging rate of 26.2 s per image.

AFM images were processed and analyzed using custom Python code. Images were flattened and filtered with a Gaussian blur to remove imaging artifacts using the SPIEPy package. Terrace boundaries were identified through local height thresholding, excluding holes that touch the image edges. Frame-to-frame linking of holes was performed by tracking their center-of-mass positions using the trackpy implementation of the Crocker-Grier algorithm.

Chapter 3.

Direct Imaging of Interfacial Fluctuations in Confined Block Copolymer with *In Situ* Slow-Scan-Disabled Atomic Force Microscopy

Reprinted with permission from J. G. Raybin, J. G. Murphy, M. Dolejsi, S. J. Sibener, *ACS Nano*, **2019**, *13*, 11741-11752.[1]

Using environmentally-controlled, high-speed atomic force microscopy (AFM), we examine dynamic fluctuations of topographically confined poly(styrene-*block*-methyl methacrylate) (PS-*b*-PMMA) cylinders. During thermal annealing, fluctuations drive perturbations of the block copolymer (BCP) interface between polymer domains, leading to pattern roughness. Whereas previous investigations have examined roughness in room temperature and kinetically quenched samples, we directly visualize the dynamics of PS/PMMA interfaces in real space and time at *in situ* temperatures above the glass transition temperature, T_g. Imaging under these experimentally challenging thermal annealing conditions is critical to understanding the inherent connection between thermal fluctuations and BCP pattern assembly. Through the use of slow-scan-disabled AFM, we dramatically improve the imaging time resolution for tracking polymer dynamics. Fluctuations increase in intensity with temperature and, at high temperatures, become spatially coherent across their confining potential. Additionally, we observe that topographic confinement suppresses fluctuations and correlations in the proximity of the guiding field. *In situ* imaging at annealing temperatures represents a significant step in capturing the dynamics of chain mobility at block copolymer interfaces.

3.1 Introduction

The length scale and regularity of self-assembled block copolymer (BCP) patterns makes them attractive candidates for next-generation lithographic and templating applications.[2,3] BCP films natively self-assemble to form periodic nanostructures, including spherical, cylindrical, gyroid, and lamellar phases.[4,5] This self-assembly process is thermodynamically driven by microphase separation of the polymer domains as governed by χ, the Flory-Huggins interaction parameter between polymer segments. Strongly-segregated BCPs produce well-defined features that may be transferred onto hard substrates for subsequent lithographic processing. While the dimensions of BCP domains are favorable for device applications, in the absence of an external guiding field, the patterns lack long-range order and form a randomly oriented fingerprint-like pattern. Traditional top-down lithography can be used to engineer the polymer substrate, through processes known as directed self-assembly (DSA), to create local fields for controlling domain orientation and alignment. Chemical[6,7] or topographic[8-10] templates induce the organization of globally ordered BCP nanostructures, advantageous for both device fabrication and for creating stable environments to study BCP assembly. In particular, graphoepitaxial control using topographically-patterned substrates enforces the alignment of confined polymer cylinders using the trench sidewalls as well-defined boundary conditions.

DSA-templated systems have been extensively studied with a focus on producing long-range domain alignment[11-13] and removing point defects.[14-16] Concerted effort by the DSA community has resulted in the realization of single-crystal, essentially defect-free BCP thin films on the 300-mm wafer scale.[13,17] Nevertheless, even with perfect domain connectivity and control over defect density, structural disorder remains in BCP thin films.[18-20] Pattern roughness, which arises from bulk composition fluctuations in segregated polymer domains,[21-23]

is enhanced by thermally excited interfacial dynamics.[24,25] A deeper understanding of these boundary dynamics is essential to understanding the intrinsic role of fluctuations in defect healing and driving changes in pattern connectivity.

Researchers have developed a variety of models and experimental methods to fully characterize line roughness, including its spatial correlation and spectral dependence.[26-29] Stein *et al*. compared the use of soft X-ray diffraction and scanning electron microscopy as tools for non-destructively measuring domain roughness, which they modeled as interfacial capillary waves.[25] Further investigation by Bosse employed computer-simulated phase-field models to track the effects of temperature, segregation strength, and confinement on roughness.[30-32] In his theoretical treatment of confined BCP ordering, Bosse demonstrated that the line-edge roughness (LER) power spectra of lamellae-forming BCP can be modeled with a two-term expression that includes the contributions of thermal capillary wave fluctuations and bulk composition fluctuations.[32] Ruiz *et al*. adapted Bosse's model by modifying the description of interfacial dynamics to include a set of undulatory and peristaltic modes.[33] These modes correspond to line-placement roughness (LPR) and line-width roughness (LWR), respectively, following a phenomenological description used for bilayer membranes. Additionally, while traditional imaging techniques are limited to the polymer surface, several experiments have investigated interfacial fluctuations in three dimensions — through modeling of the reciprocal space signal with X-ray diffraction[34,35] and in real space with transmission electron microscope tomography[36] — to develop a complete, through-film description of roughness and to characterize the effects of substrate interactions.

The previously described experimental studies examined roughness in systems cooled below the glass transition T_g, *i.e*. at temperatures where dynamic fluctuations are quenched.

While low-temperature analysis can quantify residual spatial roughness, these methods are limited to static systems and cannot separate the effect of fluctuation damping during the cooling process. Measurements above T_g are essential for directly visualizing the dynamics of BCP patterns, which, alongside domain fluctuations, include defect healing[14,37,38] and domain alignment.[11,39] Using *in situ* AFM heating techniques, several groups have independently investigated the behavior of BCP interfaces during thermal annealing. Tsarkova *et al*. observed periodic undulations of domain boundaries and found qualitative correlations between the fluctuations of adjacent domains.[40,41] When studying the formation and growth of BCP microdomains, Yufa *et al*. measured spatiotemporal autocorrelation of the interdomain boundary structure and observed an interfacial restoring force resulting from curvature minimization.[42]

Recent advancements in high-speed AFM have significantly improved instrumental stability and imaging rates, enhancing our ability to track domain fluctuations.[43] Together, these developments allow us to achieve sufficient fidelity to characterize interfacial dynamics during the thermal annealing process. In this work, we apply *in situ* AFM imaging to measure fluctuations in topographically-confined cylinder-forming poly(styrene-*block*-methyl methacrylate) (PS-*b*-PMMA). Although lamellae are more widely used in lithographic applications, a cylinder-forming BCP was selected as a model system for mapping interfacial fluctuations due to the relative simplicity of preparation under confinement.[3] The aligned BCP cylinders act as a controlled environment for analyzing disorder under varying experimental conditions, including temperature and confinement strength. Because of the asymmetric volume fraction in cylinder morphologies, the minority block exhibits enhanced coherence within the majority matrix. In this report, we describe the use of slow-scan-disabled AFM imaging to directly capture and quantify the interdomain fluctuations in confined BCP, and show that these

fluctuations increase in intensity and become spatially coherent with temperature. Ultimately, this method provides direct experimental insight of BCP fluctuations in real time and real space, illuminating their contribution to interfacial roughness, defect healing,[40] and pattern aging.[44,45]

3.2 SSD Imaging

To optimize our time resolution, images are acquired in the slow-scan-disabled (SSD) AFM mode. An example SSD AFM image is shown in **Figure 3.1**, in which the slow-scan axis is disabled midway through the AFM scan, as indicated by the white horizontal line. The AFM phase image shows aligned PS-*b*-PMMA cylinders within a topographic trench flanked by two neighboring regions of unconfined fingerprint pattern; the PS and PMMA domains appear as light and dark blue, respectively. Above the dividing line, **Figure 3.1** shows a conventional AFM image, as collected over a two-dimensional surface raster. Then, after the slow-scan axis is disabled, the AFM probe begins to continuously trace over the same line of the sample along the *x*-axis, enabling rapid sampling of a single one-dimensional cross section of the surface. With this technique, the *y*-axis of the image becomes time, while, as usual, the *x*-axis indicates the lateral position of the probe. With typical high-speed AFM imaging under our experimental conditions, a full image with 512 lines takes 25 s. By disabling the slow-scan axis, the effective time resolution is enhanced to 50 ms, while still fully capturing the dynamics of a single cross section.

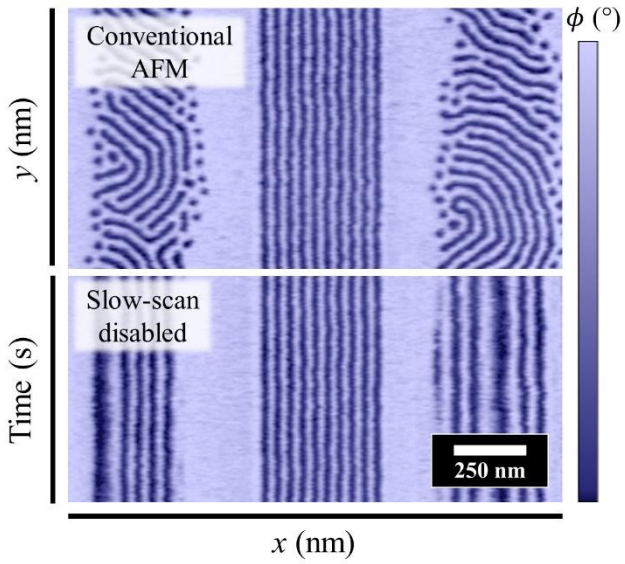

Figure 3.1 SSD AFM Phase Imaging. AFM phase channel image of aligned PS-*b*-PMMA cylinders within a topographic trench, with surrounding regions of unconfined fingerprint pattern; the PS and PMMA domains are light and dark blue, respectively. The slow-scan axis is disabled midway through the scan, as indicated by the white horizontal line, and the *y*-axis becomes time while the *x*-axis remains the lateral position. Disabling the slow-scan axis increases the effective sampling time resolution to 50 ms.

As an example of our method, an SSD image of aligned polymer cylinders in four lithographic trenches is shown in **Figure 3.2a**. The PS and PMMA domains have strong contrast in the phase due to differences in energy dissipation at the AFM tip, allowing us to distinguish between the two blocks.[38] Peaks and valleys in ϕ, shown in **Figure 3.2b**, correspond to the PS matrix and PMMA cylinders, respectively, in the image cross-section, marked as a line scan in **Figure 3.2a**. We identify the domain interfaces as the points of greatest change in phase, determined from the extrema of the first-derivative signal $\Delta\phi/\Delta x$. BCP domain interfaces are often described as arctangents or error functions.[22,46] We therefore model the boundary line using a Gaussian fit to the first derivative signal. Further details on Gaussian fitting are included in **Figure SI.3.1** in the Supporting Information. Each guiding trench contains seven PMMA cylinders, indexed i = 1 to 7, and each has two corresponding domain interfaces, with positions

$e_{i,n}$, where $n = L$ or R denote the left and right edges. We obtain the cylinder placement p_i from the average of the left and right edge positions and the width w_i from the edge separation:

$$p_i = \frac{1}{2}\left(e_{i,L} + e_{i,R}\right); \quad w_i = \left(e_{i,R} - e_{i,L}\right) \tag{1}$$

In our confined system, cylinders have a confined pitch of 46.5 ± 4.1 nm, which remains stable over the temperatures surveyed, as shown in Supporting Information, **Figure SI.3.2**. This pitch slightly exceeds the native cylinder periodicity L_0 of our BCP, 44.1 ± 1.7 nm, as measured in thin-film samples without lateral confinement. The polymer pattern is moderately incommensurate with the trench width, and the resulting strain is distributed between the cylinder domains.[9] Our measurements examine fluctuations of these domains within the free energy landscape defined by the confining trenches.

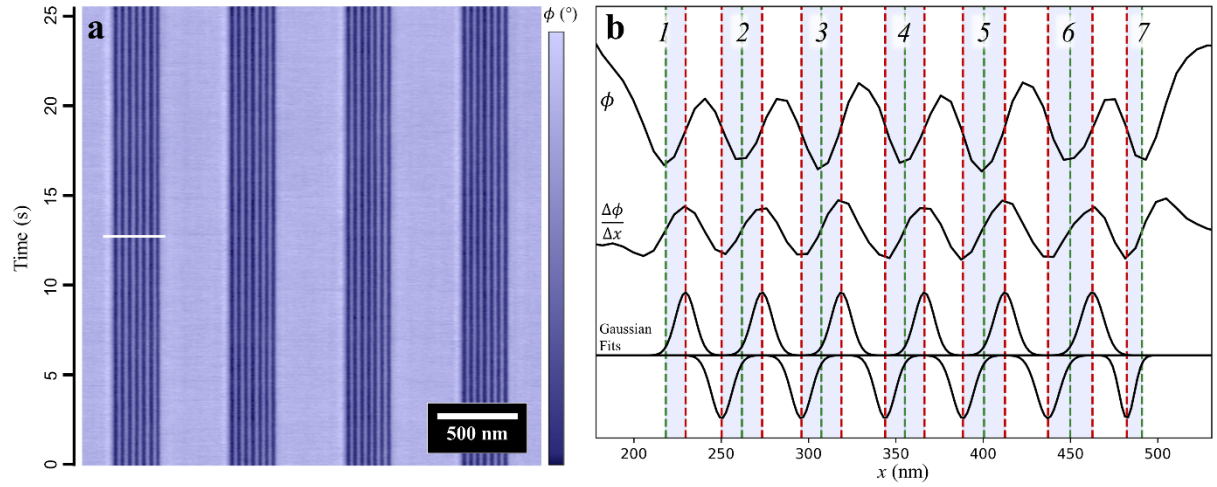

Figure 3.2 Identification of Cylinder Positions. (a) SSD AFM phase channel image of aligned PS-*b*-PMMA cylinders in a confining trench. Phase contrast distinguishes PS (light blue) and PMMA (dark blue). Because the slow-scan axis is disabled, the *y*-axis of the image measures time. A phase ϕ cross section of the seven cylinders, marked as a white horizontal line across the first trench, is plotted in (b). The $\Delta\phi/\Delta x$ derivative curve and associated Gaussian fits are used to determine the position of cylinder edges (dashed red lines), placements (dashed green lines), and widths (blue shaded areas). The left- and rightmost interfaces are not fit, as maxima are poorly defined at the trench sidewalls.

Within the trenches, the film topography varies slowly with respect to the AFM tip radius and phase imaging serves as a true measure of the surface composition. However, along the boundaries of the trench, where the film height changes rapidly, we see an unavoidable convolution of the phase signal due to coupling with the sample topography. Interactions between the AFM probe and the trench sidewall dissipate energy leading to a change in the phase offset.[47] As a result, we cannot directly identify the position of the left- and rightmost cylinder edges, *i.e.* $e_{1,L}$ and $e_{7,R}$, from the first-derivative signal. Instead, we assign the location of these edges by assuming the cylinders are symmetric about their central position, determined from the ϕ minima for these cylinders. Because of this methodological discrepancy, these edges are omitted from analysis of spatial correlations.

3.3 Time-Dependent Trajectories

Our *in situ* imaging directly captures the time-dependent fluctuations of each domain boundary. Each SSD image includes 512 linescan traces, which together produce a time-resolved trajectory of the fluctuations for each PS/PMMA interface $e_{i,n}(t)$. The position of the i-th interface fluctuates from its average point, with residual:

$$\delta e_{i,n}(t) = e_{i,n}(t) - \langle e_{i,n} \rangle \tag{2}$$

where <·> represents the time average. These terms are illustrated in the schematic in **Figure 3.3a**. From the edge trajectories we obtain the corresponding placement $p_i(t)$ and width $w_i(t)$ time series for each cylinder, with residuals:

$$\delta p_i(t) = p_i(t) - \langle p_i \rangle; \qquad \delta w_i(t) = w_i(t) - \langle w_i \rangle \tag{3}$$

The fluctuations for each term are observed to be normally distributed about their equilibrium values, as shown in **Figure 3.3b-d**. Additional examples over varying *in situ*

temperature are included in Supporting Information, **Figure SI.3.3**. Roughness parameters based on the variation of each of these terms are categorized as LER, LPR, and LWR. While roughness is conventionally determined from the spatial variation along pattern stripes, here we measure these parameters from the distributions of the time-resolved ensemble. Although we expect spectral dependence to differ in the time domain, the magnitude of fluctuations remains consistent in either ensemble. Following convention, LER is defined as the third standard deviation of the edge position:

$$3\sigma_e = 3\langle \delta e_{i,n}(t)^2 \rangle^{1/2} \quad (4)$$

Similar definitions are used for LPR and LWR:

$$3\sigma_p = 3\langle \delta p_i(t)^2 \rangle^{1/2}; \; 3\sigma_w = 3\langle \delta w_i(t)^2 \rangle^{1/2} \quad (5)$$

LPR and LWR are not independent variables, but rather are linked by their definitions in equation (1), and they are related to LER as:

$$\sigma_p{}^2 = \tfrac{1}{2}\,\sigma_e{}^2\,(1+c); \qquad \sigma_w{}^2 = 2\,\sigma_e{}^2\,(1-c) \quad (6)$$

where *c* is the linear correlation coefficient between adjacent edges under the assumption that the edge roughness is consistent across each cylinder. The value of *c* varies between -1 (total negative correlation), 0 (no correlation), and 1 (total positive correlation). Models of the in-phase and out-of-phase behavior of fully correlated and anti-correlated edge fluctuations, respectively, are depicted in **Figures 3.3e** and **f**. We note that in equation (6) positive correlation enhances LPR, while negative correlation enhances LWR. In BCP patterns, polymer chain connectivity and incompressibility lead to coherence between the interfacial positions, and we anticipate positive values for *c*.[48]

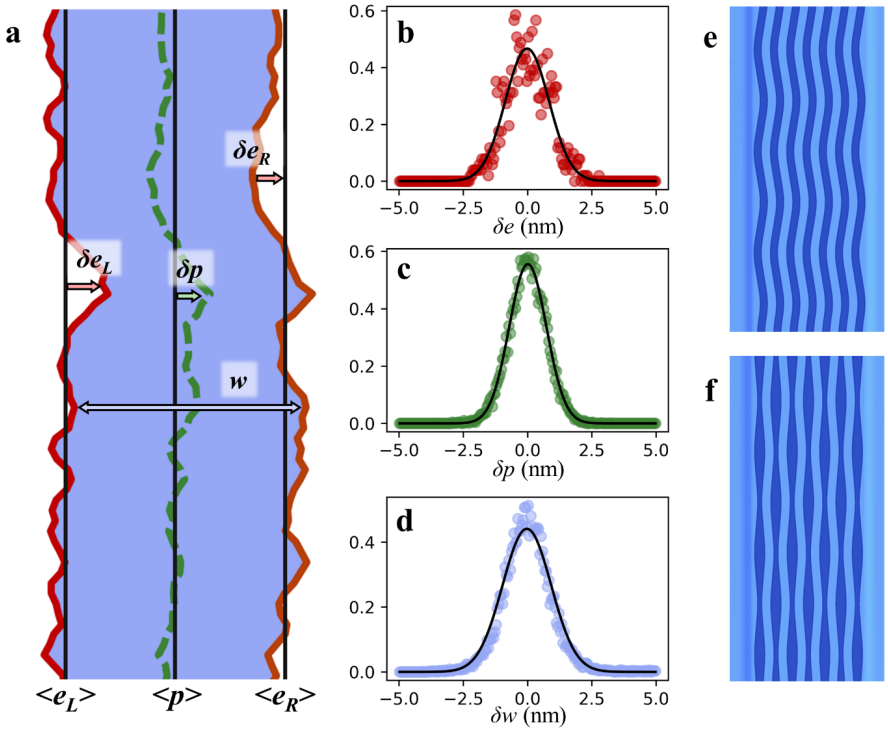

Figure 3.3 Roughness Parameter Definitions. (a) Schematic including definitions for cylinders edges, <*e*>, placements, <*p*>, and widths, <*w*> averaged over time and their residuals δe, δp, and δw. (b-d) Measurements at 150 °C of the respective residuals (red, green, and blue points) for each of these parameters, follow Gaussian distributions (black fit lines). Cylinder fluctuations include contributions from (e) correlated edge fluctuations and (f) anti-correlated edge fluctuations.

Representative trajectories showing the edge (red points) and placement (green points) fluctuations of a PMMA cylinder for a range of temperatures 150, 210, and 240 °C are shown in **Figure 3.4a**. Following thermal equilibration, the observed trajectories remain stable over time throughout SSD imaging. With increasing temperature, fluctuations intensify due to both an increase in thermal energy and a decrease in domain segregation. The resulting trajectories include a set of contributions over frequency space, reflecting a range of dynamic time scales. Each time series tracks a slowly varying low-frequency signal modulated by high-frequency variation. The relative frequency components of each trajectory are described using the discrete power spectral density (PSD) of edge displacements, as shown in **Figure 3.4b**. In the plots, the

red bands show the first-standard deviation bounds of the PSD signal averaged over 3-10 SSD images, which themselves include multiple trenches and cylinders. Analogous spatial PSD plots of real-space images are frequently used to quantify roughness and correlations in BCP patterns.[29,33] In our temporal PSDs, we observe an increase in roughness at low frequencies, reflecting the combined roughness contribution of multiple polymer chains over longer time scales. With increasing temperature, roughness spectra increase in magnitude and flatten as interaction dynamics extend to higher frequencies.

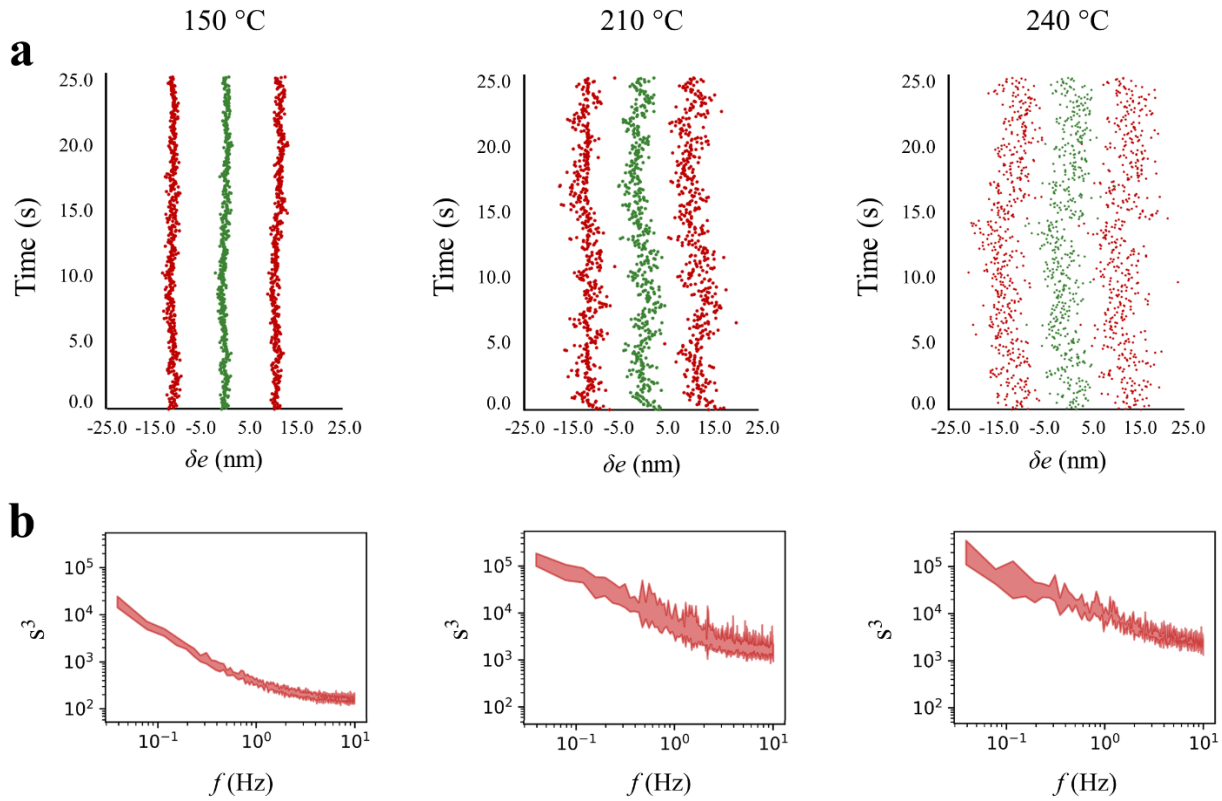

Figure 3.4 Spatial Trajectories. (a) Representative trajectories showing edge (red points) and placement (green points) residuals of a PMMA cylinder at 150, 210, and 240 °C. Trajectories show strong spatial correlation, but have insufficient time resolution to fully capture polymer dynamics. (b) Corresponding discrete PSD plots of the spectral roughness as a function of temporal frequency at each temperature. The red bands indicate the first standard deviation bounds of the discrete PSD as averaged over cylinder trajectories in 3-10 AFM images. Roughness spectra increase in magnitude and flatten with increasing temperature.

The PSD plots span a frequency range of 10^{-2} to 10 Hz, limited at low frequency by the survey time and high frequency by the scan rate. Imaging parameters were selected to ensure that the sample region was not influenced by the AFM scanning action, as verified by survey scans following each SSD experiment. Scanning too quickly can lead to abrasion of the polymer surface; scanning for too long can lead to local sample cooling due to the proximity of the AFM tip. Ultimately, these limits define the dynamic regime accessible to our investigation. Because the interdomain fluctuations exceed the rate of our AFM imaging, we see no time correlation in edge positions between line scans. Polymer dynamics faster than the Nyquist frequency cannot be detected and instead contribute to aliasing of the PSD signal, observed as flattening of the PSD at high frequencies.[49,50] More rapid scan rates will be necessary to fully resolve the spectral dependence of interdomain fluctuations.

Although we are unable to resolve time correlations, we do observe significant spatial correlation between cylinder edge displacements at each time step. The measured trajectories show coherence that is not consistent with stochastic thermal noise. To test for the possibility of systemic noise, we considered two controls: (1) comparison of cylinder edges at the same time step in spatially separated trenches and (2) measurements of sidewall motion in substrate trenches without BCP. Under each control condition, we observe no spatial coherence, affirming that our sampling serves as a reliable measure of boundary dynamics. Information on the roughness and correlation of the empty trench sidewalls is reported in **Figure SI.3.4** in the Supporting Information. Further discussion and analysis of spatial correlations of cylinder fluctuations is expanded on below.

3.4 Line Roughness

In the strong-segregation limit, the interdomain boundary has a finite width where the composition continuously transitions between PS and PMMA.[22,51] When examined in systems quenched below T_g, the block composition varies along the boundary resulting in spatial roughness. Above T_g, the interface is dynamic and is continuously modulated by fluctuations as seen above in **Figure 3.4a**; these fluctuations, in turn, contribute to the pattern roughness. Because thermal annealing conditions are difficult to access experimentally, roughness has been traditionally measured in cooled samples. However, our *in situ* measurements allow for analogous determination of roughness parameters in the time domain.

To understand the effect of the confining potential, we consider LER ($3\sigma_e$), LPR ($3\sigma_p$), and LWR ($3\sigma_w$) as a function of domain position. We find that each of the roughness parameters and their associated uncertainties are enhanced with increasing distance from the trench sidewalls at 240 °C, as shown in **Figure 3.5a**. The sidewalls act as external guiding fields and suppress interfacial fluctuations of sidewall-adjacent cylinders (i = 1, 7).[32,52] At the center of the trenches, polymer domains are insulated from the hard sidewall by neighboring cylinders and experience a local environment that more closely resembles unconfined polymer, leading to increased roughness. Interestingly, we measure a consistent value of $c \sim 0.78$ at 240 °C, suggesting that the enhanced roughness does not result from changes in interfacial correlation. This finding contrasts with phase-field simulations of confined polymer in which Bosse identified damping of the interface-interface covariance in the proximity of the guiding field.[31] This discrepancy arises because we examined PMMA cylinders, as opposed to the two-dimensional and fully symmetric patterns studied in Bosse's simulations. Cylinders act as incompressible units which have uniformly high interfacial correlation and are therefore less

susceptible to the influence of the guide pattern. A complete list of values for $3\sigma_e$, $3\sigma_p$, $3\sigma_w$, and c as a function of trench position are collected in **Table 3.1**, with uncertainties corresponding to their first standard deviation.

Table 3.1. LER, LPR, LWR, and edge-edge covariance as a function of position within the trench**.** Uncertainties correspond to the first standard deviation bounds.

Position (at 240 °C)	**$3\sigma_e$ (nm)**	**$3\sigma_p$ (nm)**	**$3\sigma_w$ (nm)**	***c***
1, 7	9.8 ± 0.4	8.6 ± 0.3	6.4 ± 0.1	0.79 ± 0.01
2, 6	10.5 ± 1.3	9.2 ± 0.7	6.9 ± 0.9	0.78 ± 0.03
3, 5	10.0 ± 0.9	9.1 ± 0.8	6.5 ± 0.4	0.79 ± 0.02
4	11.1 ± 2.0	9.4 ± 1.0	7.3 ± 1.0	0.77 ± 0.05

In addition to measurements across trenches, our *in situ* imaging allows us to directly measure LER, LPR, and LWR at a series of temperatures above T_g, as plotted in **Figure 3.5b**. At 150 °C, we measure a baseline fluctuation intensity consistent with the instrumental response at room temperature, as shown in **Figure SI.3.3** in the Supporting Information. Above 150 °C, roughness parameters, based on averages from multiple datasets at each temperature, initially increase with temperature due to an enhancement of thermal fluctuations alongside an accompanying decrease in the domain segregation strength. However, above 220 °C the roughness plateaus and we find limiting values of $3\sigma_e \sim 10$ nm, $3\sigma_p \sim 9$ nm, and $3\sigma_w \sim 7$ nm. In our system, the range of cylinder positions is constrained by the confining trench, which determines an upper limit for LER and LPR. Meanwhile, variations in cylinder widths are limited by the chain length and domain incompressibility, setting an upper bound for LWR.

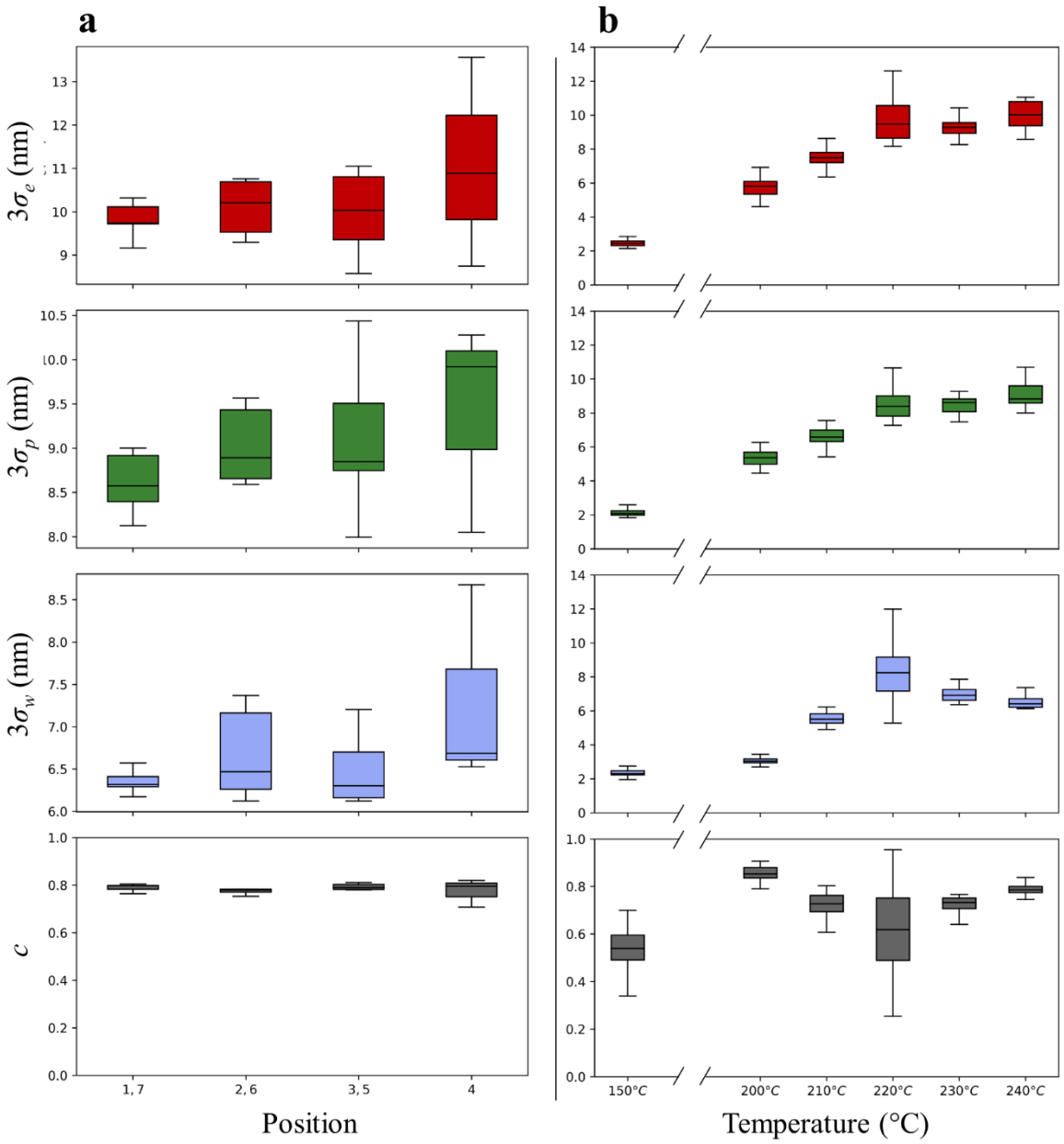

Figure 3.5 Roughness Parameters by Cylinder Position and Temperature. (a) Box plots showing the median and distribution of measured roughness parameters at 240 °C. Roughness varies between cylinders at sidewall positions (i = 1, 7) and those at central positions (i = 4). LER ($3\sigma_e$) and LPR ($3\sigma_p$), and LWR ($3\sigma_w$) are suppressed adjacent to sidewalls, where fluctuations are pinned by the confinement potential. The edge-edge covariance c is constant across the trench. (b) Box plots comparing roughness measurements over *in situ* temperature. Roughness initially increases with temperature and saturates above 220 °C. The value of c increases above 150 °C but varies due to measurement uncertainty. To control for confinement effects, cylinders at sidewall positions (i = 1, 7) are excluded from the temperature series data.

In all cases, our measurements include contributions from both cylinder fluctuations and AFM imaging noise. However, at 220 °C imaging noise is further amplified due to reduced phase contrast between the polymer domains. At this temperature, PS and PMMA have similar interaction energetics with the air interface, consequently lowering their contrast during AFM imaging.[53]

Over the temperatures surveyed, we measure positive values for c in the range $c \sim 0.5$ to 0.9. At 150 °C, where fluctuations are relatively small, dynamics at one interface have a minor influence on neighboring interfaces, and we measure $c = 0.54 \pm 0.10$. Above 150 °C, coherence helps accommodate the strain of increased fluctuations, leading to a general increase in the value of c. However, we see large variation in c at 220 °C that can be partially attributed to imaging noise, resulting in an apparent decorrelation of edge measurements. Mean values for $3\sigma_e$, $3\sigma_p$, $3\sigma_w$, and c as a function of temperature are collected in **Table 3.2**, with uncertainties corresponding to their first standard deviation.

Table 3.2. LER, LPR, LWR, and edge-edge covariance as a function of temperature. Uncertainties correspond to the first standard deviation bounds.

Temperature (°C)	**$3\sigma_e$ (nm)**	**$3\sigma_p$ (nm)**	**$3\sigma_w$ (nm)**	***c***
150	2.5 ± 0.2	2.1 ± 0.2	2.4 ± 0.2	0.54 ± 0.10
200	5.8 ± 0.5	5.4 ± 0.4	3.1 ± 0.2	0.86 ± 0.03
210	7.7 ± 1.7	6.8 ± 1.2	5.7 ± 1.5	0.72 ± 0.05
220	10.2 ± 2.5	8.6 ± 1.3	8.4 ± 1.7	0.60 ± 0.22
230	9.3 ± 0.6	8.5 ± 0.5	7.0 ± 0.4	0.72 ± 0.04
240	10.3 ± 1.3	9.1 ± 0.8	6.7 ± 0.7	0.78 ± 0.03

When interpreting these values, we note that AFM imaging is limited to measuring the structure and roughness of the BCP pattern at the atmospheric interface, and we therefore expect our analysis to overestimate roughness. At the free surface, the polymer forms a melt-like layer with increased chain mobility, leading to heightened fluctuations.[54-56] Three-dimensional surveys of BCP interfaces have confirmed that surface roughness is enhanced with respect to the bulk.[34,36]

3.5 Spatial Correlation

Within each trench, cylinder motions are coupled. The coherent behavior of the striped pattern may be described by a continuum model in which the motion of spatially-separated cylinders is coupled by a set of collective undulatory and peristaltic modes. LPR is directly associated with cylinder undulations; LWR is similarly associated with peristalsis, but is also influenced by bulk composition fluctuations.[34]

Heretofore, we have only examined the correlations between adjacent interfaces across a PMMA cylinder. We generalize our previous analysis to include long-range correlations using Pearson correlation coefficients (PCC) to identify correlations for a pair of edges $e_{i,n}$ and $e_{j,m}$ at each time step t:

$$\rho_e(i,n;\ j,m) = \frac{cov(e_{i,n}(t),\, e_{j,m}(t))}{\sigma_e(i,n)\ \sigma_e(j,m)} \tag{7}$$

where cov(·) measures the covariance and $\sigma_e(i,n)$ is the standard deviation of the n-th edge of the i-th cylinder.[57] This methodology follows a procedure employed by Constantoudis *et al*. to describe cross-line correlations in DSA-templated patterns.[27] Similar definitions may be used to compare cylinder widths and placements. This approach allows us to measure the extent of lateral correlation across a trench based on PCC values ranging from -1 (negative correlation) to

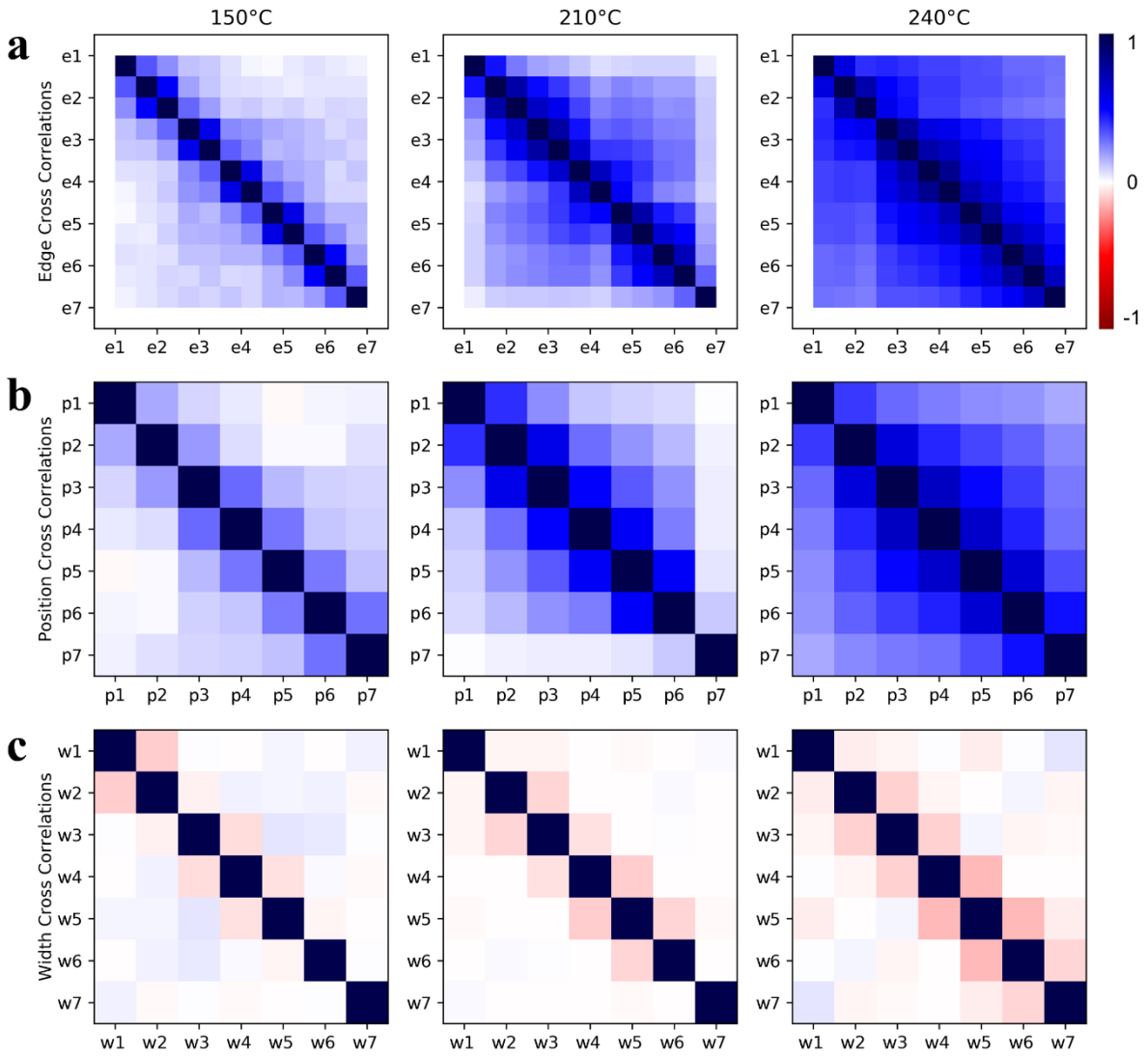

Figure 3.6 Long-Range Correlation Matrices. (a) PCC matrices show cross correlations of edge positions across the trench at 150, 210, and 240 °C. Each matrix element is colored according to the PCC value for a pair of edge residuals $\delta e_{i,n}$ and $\delta e_{j,m}$. The matrices are symmetric, and diagonal elements have an autocorrelation of 1. At 150 °C, the edge displacements of adjacent cylinders show positive correlation, and the correlation strength decreases with separation. As the temperature is increased to 210 and 240 °C, the magnitude and range of correlations increase to extend across the trench. The left- and rightmost edges, which were not directly fit, are not included in the matrices. (b) PCC matrices of cylinder placements at 150, 210, and 240 °C. At 150 °C. Positive correlation is observed between the placements of adjacent cylinders, which weakens with greater separation. With increasing temperature, the range and magnitude of placement correlation increases to extend across the trench, which we associate with coherent undulatory modes. (c) PCC matrices of cylinder widths at 150, 210, and 240 °C. Minimal correlation is observed at 150 °C, while at higher temperatures the widths of adjacent cylinders become negatively correlated. The range of the width anticorrelation, which is associated with peristaltic modes, does not extend beyond adjacent cylinders.

1 (positive correlation). **Figure 3.6** shows a set of correlation matrices comparing the positions of cylinder edges, placements, and widths over a temperature series of 150, 210, and 240 °C**.** In these plots, each matrix element compares the position of a reference cylinder to that of another cylinder in the trench at the same time step. Correlations are then averaged over time and over multiple trenches to generate PCC matrices representative of the statistical correlation for each pair of cylinders. The matrices are symmetric, and diagonal elements have an autocorrelation of unity. Collectively, these plots reveal trends in fluctuation intensity and correlation as functions of temperature and domain separation.

Correlations of edge fluctuations are shown in **Figure 3.6a**. Over this series, we observe that the strength and extent of spatial correlations are enhanced with increasing temperature. At 150 °C, adjacent domains, which are offset by one from the matrix diagonal, show positive correlation, while more separated domains show weaker correlations. Increasing the temperature to 210 °C, we find that the intensity of the positive correlations strengthens and that the range of coherence increases to include most of the trench, while still smoothly decreasing with separation. Finally, at 240 °C robust, positive correlations extend fully across the trench, indicating strong coupling between the confined cylinder edges. This range exceeds correlation lengths measured of DSA patterns on chemically-templated substrates, in which correlations are limited by the threefold periodicity of the underlying guide pattern.[27]

While edge correlations are consistently positive, the intensity of correlations between adjacent cylinders is observed to modulate between alternating edges: edges that span PMMA domains ($e_{i,L} \rightarrow e_{i,R}$) show a stronger correlation than those across PS domains ($e_{i,R} \rightarrow e_{i+1,L}$). The effect is most apparent when examining the adjacent off-diagonal terms in **Figure 3.6a** at 150 °C. With increasing temperature, the intensity difference between alternating matrix elements

narrows as the system becomes globally coherent. This contrast arises because the longer-chain PS domains have greater configurational flexibility, and elastic deformation of the majority block more effectively screens interfacial correlations. The PMMA cylinders are comparatively inflexible, leading to a stronger edge correlation. As such, the predominant stable mode of our system is characterized by undulations of the minority-block PMMA cylinders in the PS matrix.[58]

Next, in **Figure 3.6b**, we examine correlations between cylinder placements, which are directly related to undulatory oscillatory modes. The motion of placements is positively correlated, *i.e.*, as one cylinder oscillates, its neighbors tend to move in the same direction. At 150 °C, we observe weak positive correlation between nearest neighbors, which further weakens between more distant cylinders. Then, at 210 °C we find a significant increase in the strength of placement correlations that propagate throughout the cylinders in the trench. However, we observe that the coherence of sidewall-adjacent cylinders (i = 1, 7) is damped, due to the rigidity of the lithographic trench. Finally, we find complete coherence of cylinder placements at 240 °C, with a small decrease along the sidewalls. These correlations arise from in-phase edge dynamics and correspond to a collective undulatory mode. The similar trends between edge and placement correlations are expected because placements are determined from the numerical average of directly adjacent edges, which are observed to be positively correlated in all temperatures surveyed.

Correlations between cylinder widths, shown in a set of PCC plots in **Figure 3.6c**, are comparatively weak. At 150 °C, we see minimal correlation between cylinder widths at any separation. With increasing temperature, at 210 °C we observe anticorrelation between adjacent cylinders with no long-range coupling. Due to coupling of peristaltic modes, extension of one

domain induces compression in its neighbors, leading to anticorrelated behavior. The strength of the anticorrelation between adjacent cylinders is further increased at 240 °C, but there is no corresponding increase in range. Global coherence is mitigated by the contribution of local composition fluctuations to width variation.[34] Notably, we observe that the magnitude of the anticorrelation at 210 and 240 °C is suppressed for cylinders i = 1, 7, due to stabilization from the trench sidewalls.[31,48]

Due to the BCP microstructure, interfacial fluctuations are inherently structurally anisotropic. Our SSD measurements, which show long-range coherence extending across multiple domains to encompass the trench, only examine behavior perpendicular to the cylinder alignment. Previous studies have found that small-angle fluctuations in BCP patterns form anisotropic grains oriented orthogonally to BCP pattern.[45,59] Although inaccessible to our one-dimensional measurement technique, we expect a shorter length scale for correlations along the axis parallel to the stripes, which have predominant wavelength contributions on the order L_0.

As an additional representation of fluctuation correlation, sets of pairwise distributions of edge displacements are collected in hexagonally-binned, two-dimensional histograms, shown in **Figure 3.7**, for a series of domain separations (1st, 2nd, and 3rd order) and temperatures (150, 210, and 240 °C). Each histogram corresponds to a collection of cylinder pairs with uniform domain separation, as indicated by the colored diagonal lines in the associated PCC matrices. Hexagonal binning allows for visualization of the magnitude and correlation of roughness without biasing toward horizontal and vertical gridlines, while also displaying nearest-neighbor symmetry. From the variance and shape of the distributions, we obtain information on both fluctuation intensity and coherence: tight clustering signifies small fluctuations, while a wide distribution indicates large fluctuations. As shown in **Figure 3.7**, the distribution is initially

compact at 150 °C and broadens with increasing temperature as fluctuations are enhanced. Meanwhile, covariance in the pairwise edge displacements, which appears as a linear trend in the histogram plots, directly corresponds to correlations of the associated PCC matrix. At all temperatures, the plots become less linear and more diffuse with increasing separation as edge displacements become decoupled. Generally, we observe that edge fluctuations increase with temperature and become less correlated with increasing domain separation.

These trends result from local coupling of cylinder dynamics by BCP chain connectivity and compositional constraints. At each time point, the transient structure reflects a thermal perturbation from the equilibrium state, as determined by a balance between the enthalpic penalty of polymer mixing and the entropic freedom of the random coil.[4] Increasing temperature weakens domain segregation, resulting in enhanced composition fluctuations and interfacial broadening.[23] With increased thermal energy, the polymer chains also have greater configurational freedom, which is visible as increased interfacial roughness. The associated interfacial tension and bending strain from edge displacement are accommodated by neighboring domains, leading to correlated motion. At 150 °C, the observed edge perturbations are small, with a range of ~ 2 nm, and become sufficiently damped by one neighboring domain. Comparatively, at 240 °C, edge displacements have magnitudes of ~ 5 nm, roughly 20% of the cylinder width, resulting in large deviations from their equilibrium positions, and stabilization from correlated motion becomes significant. Our measured displacements correspond closely with interfacial widths of 4.9 ± 0.1 nm reported by Stein *et al*. in lamellar PS-*b*-PMMA after thermal annealing at 240 °C and quenching to room temperature. Fluctuations during thermal annealing directly contribute to the ultimate quenched roughness.[25]

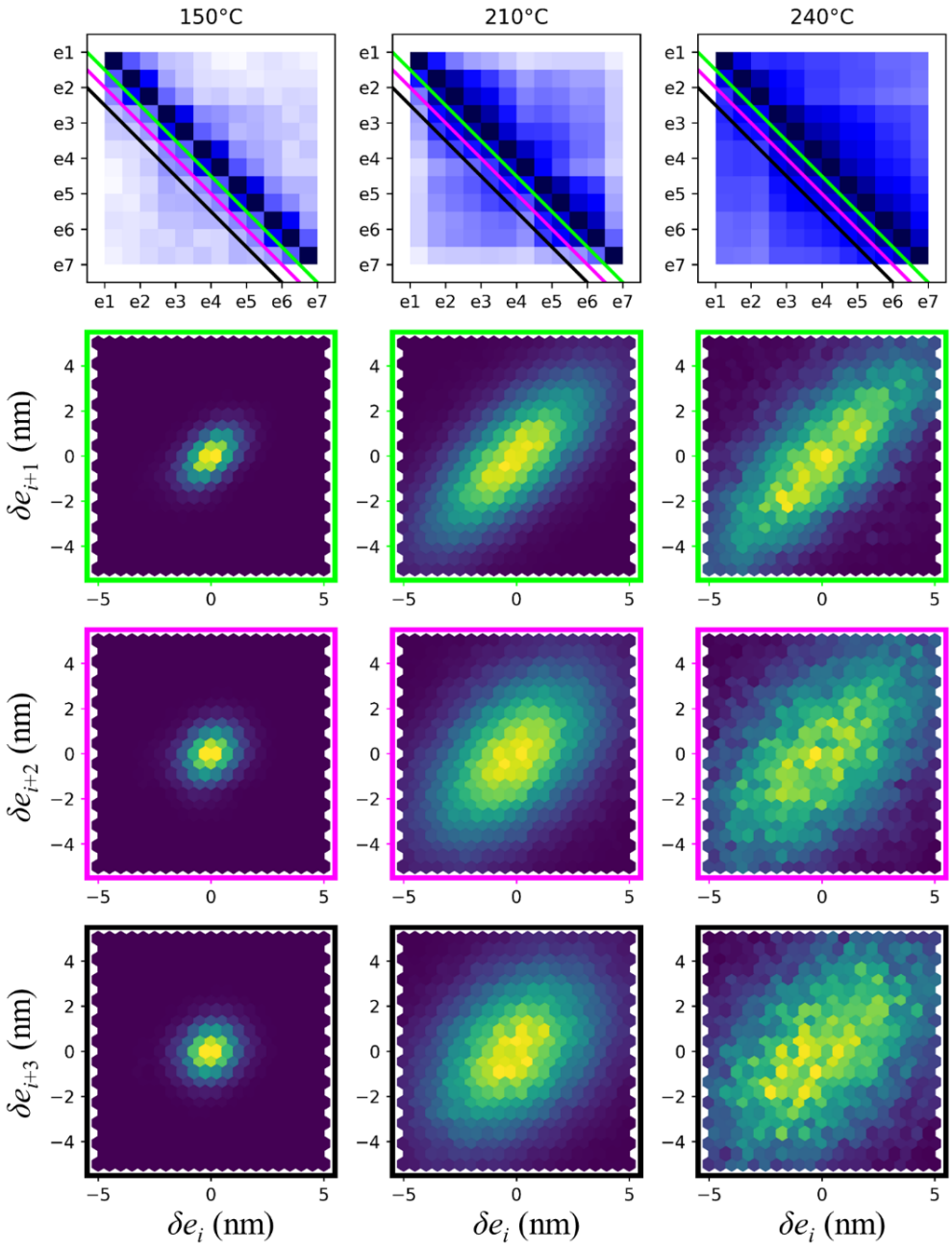

Figure 3.7 Edge Roughness Covariance. Two-dimensional histograms showing the pairwise distributions of edge displacements over a series of cylinder separations (1st, 2nd, and 3rd order) and temperatures (150, 210, and 240 °C). Each plot corresponds to a set of off-diagonal PCC matrix elements as indicated by the colored lines. The distribution spread shows the magnitude of fluctuations, while the distribution shape indicates correlation between the edge displacements. The fluctuation magnitude increases with increasing temperature, and the covariance decreases with increasing separation.

3.6 Conclusions

Lithographic templating applications of aligned DSA systems rely on careful understanding and control over structural disorder in BCP patterns. While previous investigations have characterized roughness in quenched, room temperature systems, *in situ* high-speed AFM imaging serves as a direct method for capturing the BCP dynamics above T_g. High-temperature imaging represents a significant step in understanding the intrinsic connection between the assembly of BCP patterns and dynamic fluctuations. Using SSD AFM imaging, we find that roughness scales with the annealing temperature and saturates above 220 °C. We identify robust spatial correlation that extends laterally across each individual confining trench. This coherence reflects continuum behavior in which cylinder oscillations may be described as a set of undulatory and peristaltic modes. These coupled dynamics directly contribute to the roughness and structural disorder of BCP patterns. In the future, we hope to examine time-dependent correlations and believe this to be feasible in higher molecular weight systems. Fluctuations should be understood not just as a barrier to pattern alignment, but as fundamental to thermal annealing and defect healing of BCP thin films.

3.7 Methods

Silicon wafer substrates (purchased from Virginia Semiconductor) were ultrasonically cleaned under toluene, acetone, and isopropanol and dried with N_2. Trench patterns were created by electron-beam lithography using an FEI NanoSEM 230 with PMMA as the electron-beam resist. After developing in methyl isobutyl ketone for 35 s, the patterned samples were rinsed with isopropanol and dried with N_2. Patterns were transferred to the silicon wafers with CF_4 and

O_2 plasma dry etching, using a South Bay Technologies, Inc. RIE-2000. The resulting trenches were about 375 nm wide and 50 nm deep.

Cylinder-forming PS-*b*-PMMA (55k-22k, PDI 1.09) with $L_0 = 44.1 \pm 1.7$ nm was purchased from Polymer Source. A 0.9 wt% polymer solution was prepared in toluene and spin coated at 3000 rpm for 50 s onto the patterned substrates to produce a monolayer within the trench patterns. Global film thicknesses, were measured with a Gaertner Waferskan ellipsometer, and found to be roughly 20 nm.

After pre-annealing in a tube furnace under argon at 250 °C for 8 h to produce aligned patterns – *i.e*. locally free of defects – samples were imaged with an Asylum Cypher ES Environmental AFM. A single sample was stepped over a series of *in situ* temperatures from 150-240 °C while under argon flow with cell gauge pressures of 30-40 mbar. The sample was initially heated to 150 °C at a ramp rate of 2 °C/s, and was then subsequently ramped through each experimental temperature without returning to room temperature. The sample equilibrated for at least 5 min at each temperature before imaging; equilibration was verified by comparing results over a sequence of images over time.

High-speed, tapping-mode imaging was performed using gold-coated Arrow UHF cantilevers with resonant frequency of 1-1.5 MHz, achieving a scanning rate of 20 Hz and 5.9 nm pixel resolution. For our measurements, the slow-scan axis was disabled yielding an effective time resolution of 50 ms per line. Images were collected with a 500 mV set point and in repulsive mode. These scanning parameters were selected to reliably track surface features while avoiding sample degradation. Following each measurement, the surrounding sample region was inspected to verify that the pattern was not locally damaged by the AFM scan.

Sub-pixel edge tracking is achieved through linear interpolation of the AFM data. A large pixel size was necessary (1) to include multiple trenches in each image and (2) to prevent sample damage. Including multiple trenches in each image allowed us to confirm that only cylinders in the same trench were correlated to each other and that the correlations were not an artifact of the AFM line scan. Imaging over a large region also distributed AFM interaction forces over a larger scan area.

All images were collected from the same region of one sample to control for any variations in polymer film thickness or in the lithographic trench boundaries. Throughout the imaging process, the local film thickness over patterned regions remained consistent, as confirmed from AFM topography images. Pattern pitch was found to be constant within error over the temperature range surveyed, as shown in Supporting Information, **Figure SI.3.3**. Drift was minimal, less than 80 pm across the measurement time of a single image. Drift correction produced no deviation in the resulting PSD plots, as discussed in the Supporting Information, **Figure SI.3.5**.

To accurately and reproducibly track and analyze domains, we used a custom image analysis software written in Python based on the SciPy framework.[60] At each temperature, the approximate location of the first PMMA domain in each trench was manually located on the time-averaged phase trace; the six successive PMMA domains were then identified by finding the next six local minima. Each phase trace was then processed in parallel to find the true position of each domain at a given timestep. In this procedure, the approximate cylinder placement was updated to the nearest local phase minimum. The neighboring left and right maxima then defined a local window that encompassed the interfaces between a given PMMA domain and its two adjacent PS domains. The first derivative of the phase signal was then fit

with a model Gaussian to precisely locate the extrema positions, corresponding to the steepest slope of the phase and, thus, the PS/PMMA domain edges. An example of this procedure is illustrated in **Figure 3.2** and the Gaussian fitting process is further discussed in the Supporting Information, **Figure SI.3.1**. The phase signal was not well defined at the boundary of the trenches due to a rapidly changing sample topography. To account for this, the leftmost and rightmost edges along the trench were determined by doubling the distance between the first-derivative maximum and half-maxima. For each of these experiments, we analyzed datasets ranging from 3-10 images. Altogether, at 150 °C, we averaged over a total of 129,024 points for widths and placements (doubled for edges); 86,368 points at 210 °C; and 28,672 points at 240 °C.

Chapter 4.

In Situ Atomic Force Microscopy of Fluctuations and Dynamics of Block Copolymer Defects in Tapered-Width Nanochannels

Block copolymers are attractive candidates for next generation lithography applications due to their ability to self-assemble into highly ordered, periodic nanostructures. While there has been much work on achieving perfectly ordered films over a high surface area, there is also a need to control the formation of isolated defect structures in the block copolymer ordering, for example jogs and T-junctions, for application in semiconductor devices. Tapered-width lithographic trenches provide a method for generating defects in block copolymer nanopatterns in a precise manner, allowing for controlled study of defect dynamics and formation that is directly observable with atomic force microscopy imaging. Here, we report the dynamics of defects in poly(styrene-*block*-methyl methacrylate) confined in tapered-width trenches, captured through *in situ* atomic force microscopy (AFM) imaging above the glass transition temperature. Overall, this work utilizes the controlled formation of dislocations to further the understanding of interfacial fluctuations in block copolymer domains in relation to defect proximity, and how these fluctuations translate into the patterns of templated devices.

4.1 Introduction

Block copolymers spontaneously self-assemble into a variety of periodic nanostructures - including lamellae, cylinders, gyroids, and spheres - depending on the relative volume fraction of the two blocks. This assembly is driven by the microphase separation of the polymer domains as governed by the Flory-Huggins interaction parameter χ between the polymer segments, leading to a reduction in the free energy of the system. Strongly segregating, or high χ, systems lead to nanopatterns with well-defined features.[1,2] These features, combined with the chemical flexibility of block copolymers, makes these unique systems attractive candidates for lithographic templating applications.

In the absence of guiding fields, block copolymer self-assembly results in randomly oriented structures. However, long-range control over the ordering of the morphological structures is needed to adopt block copolymers in industrial applications. Much work has gone into controlling the ordering of the polymer domains and we can now create near defect-free films on wafer size scales.[3-6] A number of directed self-assembly (DSA) methods, including chemoepitaxy,[7] graphoepitaxy,[8-10] and guiding electric fields,[11-13] have been introduced to control the domain orientation and connectivity, achieving long-range order in block copolymer structures. In the case of graphoepitaxy, topographical templates create boundary conditions for alignment, propagating linear ordering along the template side walls and inducing linear order throughout the trench. However, in addition to generating films with linear order, control over specific "defect" features, such as jogs and T-junctions, is necessary for templating semiconductor devices.[14-16] As such, templating methods that provide precise control of, as well as understanding of the energetics and mechanisms behind, defect formation are needed.

Constant-width (rectangular) templates are ideal for propagating linear ordering of block copolymer domains but are limited in providing precise control over defect formation. As such, studying defects, such as dislocations or disclinations in block copolymer films, controllably requires alternative template geometries. Tong introduced the use of tapered-width (wedge) templates as a method for inducing dislocation formation.[17] In these systems, the width of the template varies continuously, thus accommodating an increasing number of cylinder domains. The domains expand to fill the widening template until the energy of expansion overweighs the energy required to introduce a new cylinder domain, at which point a dislocation is present. These dislocations exist at regular equilibrium intervals predicted by $\Delta x = d_0 / \tan \alpha$ (**Eq. 4.1**), where d_0 is the equilibrium periodicity of the unconfined domains and α is the opening angle of the wedge; an example of such a trench is as depicted in **Figure 4.1a**. The predictability of dislocation formation makes these tapered-width templates an ideal environment for studying defects in block copolymer patterns.

In this Chapter, I report the ongoing study of dislocations as a function of width and defect proximity, as well as changes in defect behavior with temperature variations. Dislocations in ordered cylinder-forming polystyrene-*block*-poly(methyl methacrylate) thin films confined in tapered-width lithographic trenches (graphoepitaxy) are directly characterized with environmentally controlled atomic force microscopy (AFM), such as depicted in the image shown in **Figure 4.1b.** I observe the dynamics of this confined system at various temperatures, ranging from 150 to 250 ^{o}C, with *in situ* environmentally controlled, high-speed AFM.

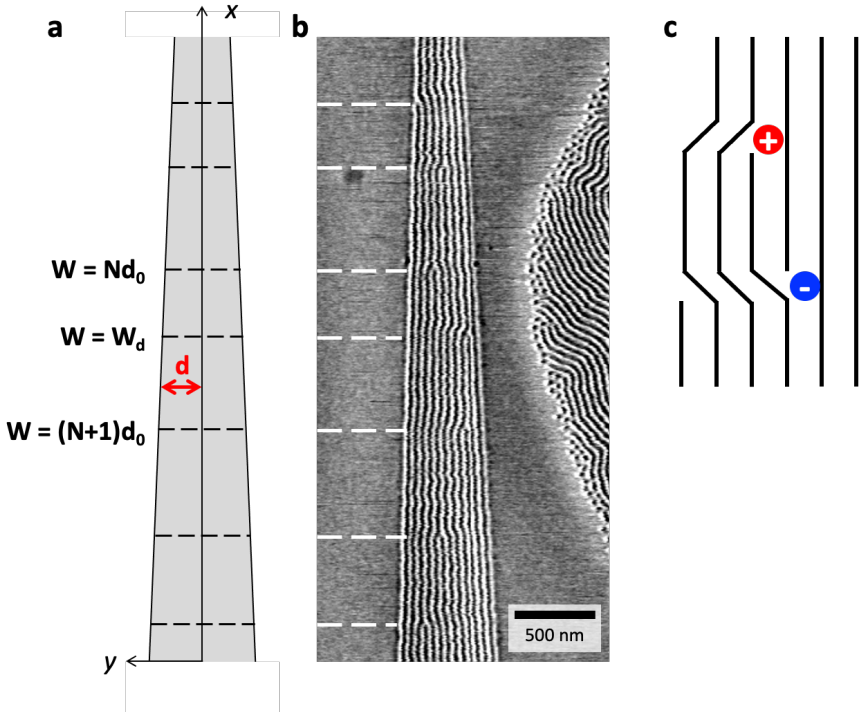

Figure 4.1 Tapered-Width Lithographic Trench. (a) Schematic diagram of a tapered-width or wedge-shaped lithographic trench. As the width of the trench narrows, the number of cylinder domains decreases by one, such that W = Nd0, where W is the width of confinement, N is the number of domains, and d0 is the equilibrium periodicity of the unconfined domains. A dislocation is introduced where the number of domains decreases, marked by black dashed lines. (b) Representative AFM phase image of PS-b-PMMA confined in a tapered-width trench. The positions of the dislocations are marked with the dashed lines on the left of the image, corresponding to the same locations depicted in the schematic. (c) Schematic depiction of a positive and negative disclination pair. The disclination in these trenches are defined as positive in this text.

4.2 Results and Discussion

Dislocations do not necessarily form at their equilibrium positions but arrive at those positions throughout the annealing process. I have observed a mechanism for this process in real time during our imaging. The mechanism consists of three steps, which are detailed below: (1) introduction of a dislocation pair; (2) dislocation climb; and (3) dislocation annihilation.

Figure 4.2 shows a series of AFM phase images taken *in situ* at 245 °C. There are six dislocations initially present in the trench, labeled 1-6 accordingly in **Figure 4.2a**. All but number 4 are in their equilibrium spacing positions, according to **Eq. 4.1**. To achieve equilibrium

positioning, a new dislocation pair (as depicted in **Figure 4.1c**), is introduced above 4, as indicated by the solid green lines in **Figure 4.2b**. The dislocation pair consists of a positive and negative dislocation, so the number of cylinders between 3 and 4 remains unchanged. The new dislocation pair gradually moves apart via a defect climb mechanism, *i.e.,* moves parallel to the patterned polymer domains, with the positive dislocation moving up the trench to the equilibrium spacing position and the negative dislocation moving closer to 4, along the *x*-axis, as shown in **Figures 4.2c-g**. The negative dislocation combines with 4, annihilating both defects. The dislocations within the trench are now all spaced according to the equilibrium positioning in **Equation 4.1**.

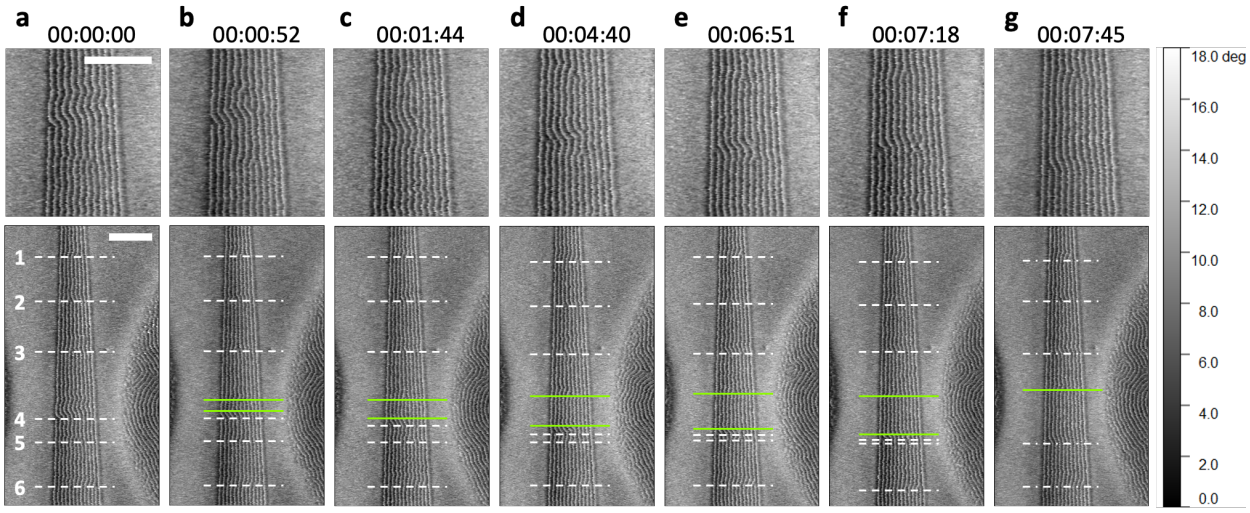

Figure 4.2 Dislocation Migration to Equilibrium Spacing. A time series of AFM phase images showing the mechanism by which dislocations reach their equilibrium positions within the trench. The top row is cropped to show the key dislocations as they evolve, while the bottom row shows the full trench with defects marked by horizontal lines. (a) Six dislocations are initially present in the trench, with dislocations numbered 4 and 5 too close together to meet the equilibrium spacing. (b) A dislocation pair is introduced (green lines) above 4. (c-f) The dislocation pair gradually separates moving along the *x*-axis, with the positive dislocation moving up the trench and the negative dislocation moving down. (g) Dislocation 4 combines with the negative dislocation, leaving all dislocations in the trench at the equilibrium spacing. Scale bars in the top right corner of panel (a) represent 500 nm.

It is interesting to note the timescale for the different steps in this defect migration mechanism: Introduction of a new dislocation pair occurs after imaging for 76.5 minutes at 245 ^{o}C. The separation and climb of the positive and negative dislocations occur over the course of about 6.5 minutes and begins in less than 1 minute after the new dislocation pair is introduced. Annihilation of the negative dislocation with Dislocation 4 occurs over less than 30 sec, over the course of one image acquisition.

This observed mechanism is in contrast with previous reports of a dislocation climb mechanism to achieve equilibrium positioning within the trench.[17] However, it is likely that the observation of this mechanism was inaccessible due to the AFM imaging time resolution required to capture each step. Previous reports suggest that the climb motion of a dislocation in confinement should be the favorable mechanism by which dislocations migrate throughout the trench, as the climb motion of a dislocation should have minimal free energy barrier.[18-20] The mechanism reported in this system is due to the additional strain created by the variation in the width of the confinement. Because of the tapered width, the movement of the dislocations up or down the trench follows a diagonal path, thus making the movement an inherent combination of climb and glide. A glide mechanism is defined as the motion of a dislocation perpendicular to the PS/PMMA domain interfaces, which requires mixing of the domains across interfaces. As such, glide motion has a higher energy barrier and is less favorable than a climb. The diagonal movement, in combination with the compression of the domains, forces the PS and PMMA blocks to mix more than they would otherwise in a straight channel. Additionally, the introduction of a new dislocation pair does not increase the strain on the system but decreases the overall distance the individual dislocations must travel to achieve equilibrium spacing. The strain

between dislocations with opposing Burgers vectors creates attractive forces that drive the dislocations together and eventually leads to annihilation.[21-27]

While the dislocations exist in these equilibrium positions, due to thermal fluctuations, the defects move across (along the *y*-axis) and up-and-down (along the *x*-axis) the channels slightly. Confinement in tapered-width channels paired with high-speed, environmentally controlled AFM enable the visualization of the relationship between defects and these thermal fluctuations within the polymer pattern. One method to look at these fluctuations are with cumulative distribution maps, as shown in **Figure 4.3**. In these maps, AFM images taken in a series are stacked on top of each other, providing a visualization of the movement of the cylinders through the imaging time. In the maps shown in **Figure 4.3,** yellow regions correspond to where cylinders are PS across all images, purple is where they are PMMA, and pink regions are where both PS and PMMA occur, indicative of pattern rearrangement. Overall, the patterns remain stable – defects remain in the equilibrium position, new defects are not introduced, and the linear alignment of domains remains. However, these cumulative distribution maps reveal that the movement caused by thermal fluctuations of the cylinders is concentrated at the locations of the dislocations. The PMMA cylinders along the sidewalls are pinned, consistent with the effects of interfacial confinement and the preferential wetting of the PMMA layer along the silicon substrate; similarly, regions between defects do not show much movement. However, the defects themselves move laterally across the trench. This movement increases with temperature, as apparent by the blurring and increased pink-coloring in the cumulative distribution map for images taken at 245 and 250 ^{o}C as compared to those at 240 ^{o}C.

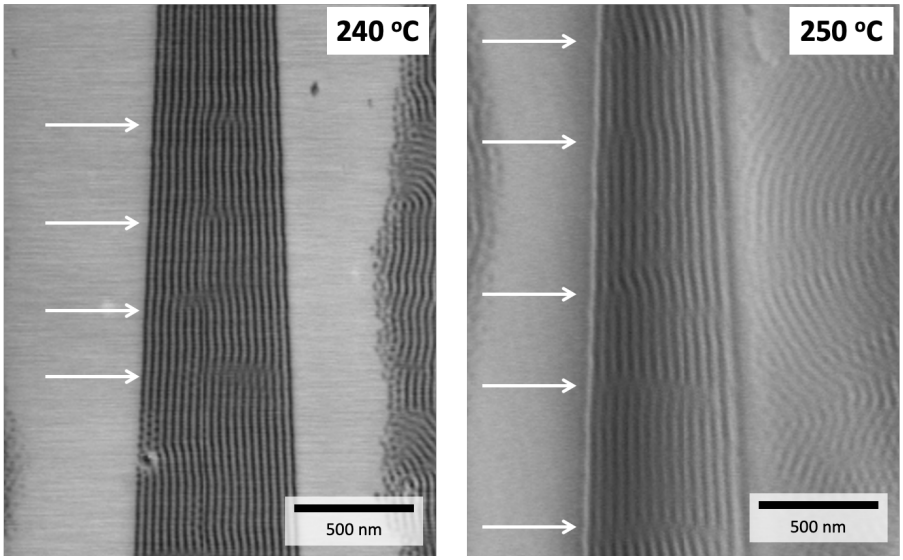

Figure 4.3 Cumulative Distribution of Cylinders across Temperature. Cumulative distribution map of AFM phase images taken at 240 °C (left) and 250 °C (right). Black regions represent PMMA cylinders, light gray are the PS cylinders, and gray regions indicate the presence of both PS and PMMA; locations of the dislocations are marked with white arrows.

I also see that the equilibrium position changes with temperature. The plot in **Figure 4.4** shows the average distance between dislocations across a temperature range of 150-250 °C; the values for the mean spacing and standard deviation are also presented in **Table 4.1**. The spacing between the dislocations increases with temperature due to combined effects of thermal expansion and confinement: As temperature increases, the polymer domain sizes increase due to thermal expansion. In turn, this increase in size leads to further compression of the cylinders within the confining trench, and the equilibrium spacing shifts to accommodate the change in the number of domains that can fit at a particular trench width. The average spacing at the higher temperatures from 240-250 °C shows a slight increase, although the values are within a standard deviation of each other. This trend is likely due to increased thermal fluctuations at these higher temperatures, leading to more variation in the measured equilibrium distance between any single images. Additionally, the region of the trench measured was not the same at each temperature. Distance measurements for the trench at 240 °C were measured across the region where the

number of domains decreases from 17 to 12, while those at 245 and 250 ºC were measured where the domains decrease from 15 to 8 cylinders. This difference could account for the smaller deviations reported in the measurements at 245 and 250 ºC. In the narrow regions of the trenches, the movement of the cylinders is less due to the increased confining effects, while the cylinders in the wider regions have more freedom to fluctuate.

Table 4.1 Average Equilibrium Spacing Distance Values. Uncertainties correspond to the first standard deviation bounds.

Temperature (ºC)	Mean spacing (nm)	Standard deviation (nm)
150	729	± 16
175	729	± 17
240	519	± 71
245	542	± 12
250	562	± 9

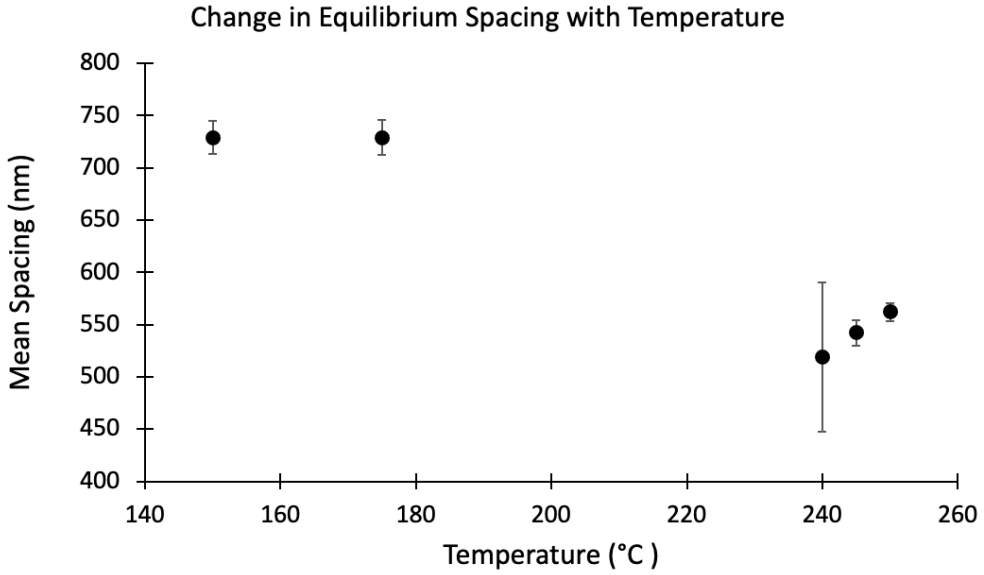

Figure 4.4 Change in Equilibrium Spacing with Temperature. Plot showing the average distance between dislocations within the trench versus temperature. Samples were measured at 150, 175, 240, 245, and 250 ºC. The equilibrium distance has an apparent decrease as temperature increases, reflecting the combined effects of thermal expansion and confinement of the polymer domains.

4.3 Ongoing Analysis

The above analysis is largely qualitative in describing dislocation formation and movement in confinement, and ongoing analysis is focused on further probing this movement and interfacial fluctuations in the polymer nanopattern. A current example of such analysis is shown in **Figure 4.5**. **Figure 4.5a** shows a skeletonized AFM images taken at 250 ^{o}C. In this image, each cylinder domain is reduced to one pixel in width at the center of the cylinder. Black lines indicate locations of the dislocations within the trench. **Figure 4.5b** shows the domain interfacial fluctuations throughout the trench plotted as a function of intensity for images acquired. This plot reveals an asymmetry in the fluctuation intensity: The fluctuation intensity is higher at the wide end of the trench and decreases gradually as the trench width decreases. This asymmetry arises due to anisotropy in the confining forces on the confined domains. In the wider region of the trench, the confining forces on the central cylinders are less, so the dislocations can move more freely than at the narrow end, where the confining forces are strong on all cylinders.

Upon normalizing against the width of the trench, as in **Figure 4.5c**, and plotting the average deviations in position, it becomes apparent that the fluctuations surrounding defects have a consistent intensity that is anisotropic. Fluctuations in position increase approaching the defect from the wide end of the trench, reaching a maximum before the number of cylinders decreases. The deviations then decrease going through the defect, reaching a minimum at the point where the number of cylinders is reduced by one. The difference between the maxima and minima values is consistent for all widths, i.e., numbers of cylinders, in the trench. This asymmetry results from confining effects of the trench: As the width narrows, the domains experience increasing compressive strain. When the domains cannot be compressed further, the strain reaches a maximum and a dislocation is introduced to reduce the number of cylinders. Because

the wider part of trench contains more domains, that strain is shared across multiple cylinders. Additionally, the wider part of trench has fewer confining effects than the narrow region. Cylinders in the center are freer to move than those close to the walls, so they can fluctuate to share the strain of the dislocation and move the dislocation across the trench.

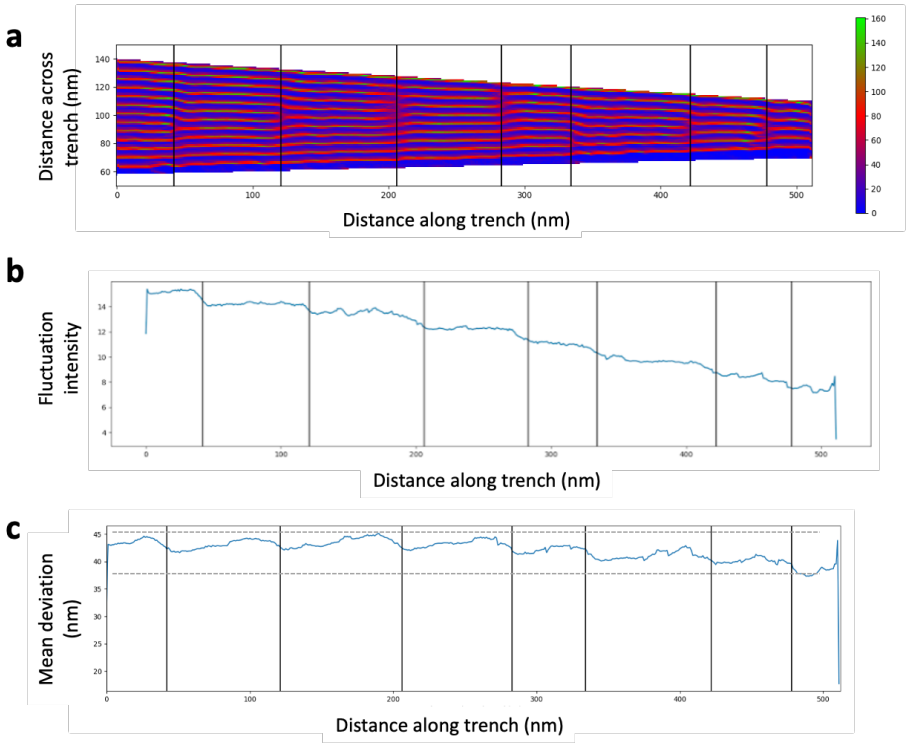

Figure 4.5 Interfacial Fluctuations surrounding Defects. (a) Skeletonized AFM phase image of PS-*b*-PMMA confined in a tapered-width trench. Red regions are the PS domains, while blue are the PMMA domains. Locations of the defects are marked with black lines. (b) Plot of fluctuation intensity as a function of distance along the *x*-axis of the trench, with defect locations marked at the black lines. Fluctuation intensity decreases with trench width. (c) Mean deviation in position as a function of distance along the *x*-axis of the trench. The deviations have sawtooth pattern with the deviation increasing approaching the dislocation from the wide end of the trench, and decrease moving through the dislocation. The difference between the maxima and minima is consistent throughout the trench.

Continued analysis on these fluctuations is underway, in particular to expand the range of measured temperatures and to relate the fluctuation intensity more directly to the physical

ordering of the polymer nanopattern. Overall, this work utilizes the controlled formation of dislocations to further the understanding of interfacial fluctuations in block copolymer domains in relation to defect proximity, and how these fluctuations translate into the patterns of templated devices.

4.4 Methods

Samples were prepared on silicon wafer substrates from Virginia Semiconductor, Inc. Wafers were sonicated in toluene and acetone for 5 minutes, then rinsed with IPA and dried under N_2. Trench patterns were created with electron-beam lithography on a FEI NanoSEM 230 using a PMMA resist annealed for 60 minutes at 175 ºC and developed in methyl isobutyl ketone for 35 s, followed by rinsing with IPA and drying under N_2. The patterns were transferred to the silicon wafers by plasma etching with CF_4 and O_2 using a South Bay Technologies, Inc. RIE-2000.

Cylinder-forming PS-*b*-PMMA (55k-22k) was purchased from Polymer Source, Inc. and prepared in 0.9 wt. % solutions in toluene. The solution was spincast onto the patterned substrates at 3000 RPM for 50 s and annealed under argon in a tube furnace at 250 ºC for 6-8 hours to induce ordering.

AFM imaging was done on an Asylum Research Cypher ES Environmental AFM. Samples were heated to the desired temperature at a ramp rate of 1ºC/s under argon atmosphere with gauge pressures of 30-40 mbar. Each sample was imaged continuously. High-speed tapping mode was done with arrow UHF cantilevers with 1-1.5 MHz resonant frequency, a setpoint of 500 mV to prevent sample damage during scanning, and scan rates of 19.53 Hz. Image scan sizes are about 3.70 μm, with 512 lines and 256 points.

Chapter 5.

Ion Transport *via* Local and Ensemble Measurements: Scanning Electrochemical Microscopy Combined with Atomic Force Microscopy

In order to design more energy efficient and selective water filtration membranes, a comprehensive understanding of molecular flow through porous media is crucial. Typical methods to study transport through membranes are macroscopic in nature, providing overall statistical properties but lacking in the detailed analysis at nano- and meso- length scales. This Chapter present combined scanning electrochemical-atomic force microscopy (SECM-AFM) as a method to bridge this gap by providing *in situ* and *operando* characterization of membranes and porous media at the single-pore size scale. Early imaging of conductive polymer blends, specifically poly(3-hexylthiophene-2,5-diyl) (P3HT) and poly(methyl methacrylate) (PMMA), demonstrate the ability to distinguish conductive islands from surrounding insulating material, both topographically and through redox conductivity. Additionally, I present direct imaging of transport of redox mediators in solution through pores in commercial membranes, as well as designs for a dual-chamber membrane sample holder to extend this imaging to investigate diffusive and iontophoretic transport.

5.1 Introduction

A comprehensive understanding of molecular flow through porous media is central to our understanding of transport in confined geometries. Important examples include materials for filtration and capture, selective permeation barriers, and catalysis. Studies of molecular transport involving macroscopic membranes are informative but lack the detailed multiscale information that governs molecular flux spanning atomic, nano-, and meso- length-scales. Such information is crucial as we seek to design more energy efficient and selective water filtration membranes, with important knowledge still needed for modelling neutral and charged molecular and particulate flow proximal to solid-water interfaces.

Membranes innately contain a distribution of pore sizes, structural inhomogeneities, and compositions that can notably influence the emanating fluxes of species in liquid environments. In this Chapter, building upon atomic force microscopy (AFM), I introduce scanning electrochemical microscopy (SECM)[2-4] and the powerful variant, SECM-AFM,[5,6] as powerful local probes for correlating surface structure to local transport activity. These methods offer unique capabilities for nondestructive quantitative measurements of transport at the level of a single pore, as well as imaging local dynamic changes to membranes under *in operando* conditions in solution. Critically, such measurements allow one to overcome the spatial averaging that occurs in more traditional macroscopic measurements where transport is examined globally through membranes sampling a wide palette of pore sizes, geometric shapes, and chemical decoration.

SECM is a scanning probe technique that provides local surface electrochemical information from monitoring reactions between a microelectrode probe and redox mediators in solution. This technique has been widely used to image transport through porous structures.

However, SECM is limited by the convolution of the topographic and current signals: The microelectrode probe is typically held at a fixed height above the sample surface without accounting for topographic variations in the sample, as shown in **Figure 5.1a;** these variations are therefore reflected in the measured current. Combining SECM with AFM allows for decoupling of the topography and current signals by first acquiring an AFM topographic scan, then retracing this topography at a constant distance above the surface while measuring the current signal, also depicted in **Figure 5.1a**. Combined SECM-AFM can thus provide current measurements that are more representative of the sample surface, enabling more complex characterization of membrane activity. Essential features of the overall electrochemical setup in SECM-AFM are shown schematically in **Figure 5.1b**, applicable to conducting as well as insulating materials.

SECM studies allow for the examination of a single pore or well-characterized membrane regions,[7-11] providing information for direct comparison with theory and simulations that seek to model transport on the atomic and nanoscales, the key length-scales that govern mass transport through such media.[12] **Figure 5.1c** illustrates the ability to locate and sample fluxes emanating from a single pore. The voltage bias between the sample working electrode and probe working electrode can be adjusted to measure diffusive or iontophoretic transport. In diffusive transport, the voltage on the sample and probe working electrodes are the same magnitude but of opposite signs, allowing measurement of the diffusion of redox mediators through a pore. Iontophoretic transport is driven by an applied voltage gradient. Further extension of these methods allows one to examine, for example, nanotextured electrodes,[13] single- nanoparticle catalysis,[14] channeled transport architectures,[15] and transport through pores in biologically relevant membranes.[16-18]

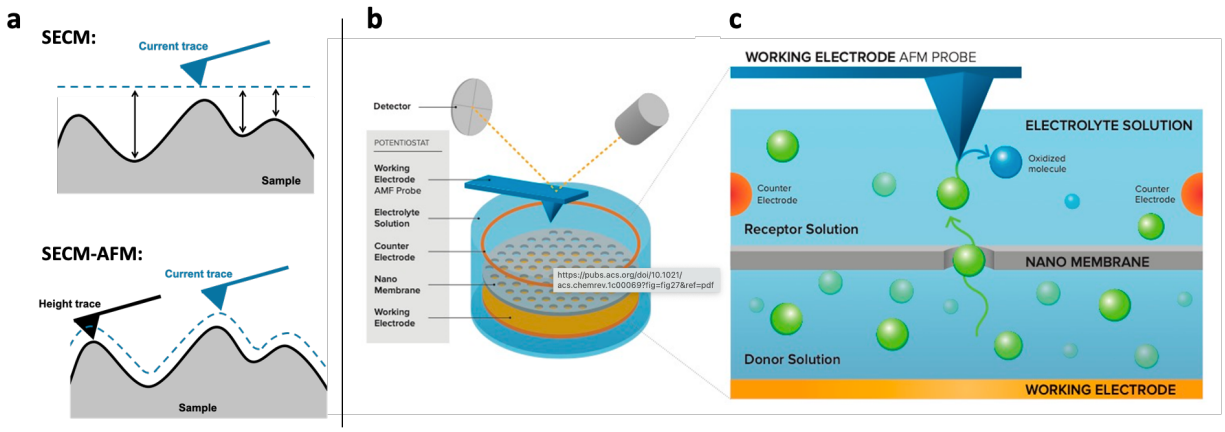

Figure 5.1 SECM-AFM Experimental Setup. (a) Schematic depiction of the probe positioning during an SECM versus SECM-AFM scan: In SECM scans (*top*), the probe is at a fixed height above the sample surface, resulting in measurements that are a convolution of current and sample topography. SECM-AFM (*bottom*) resolves this by first tracing the sample topography in tapping mode (black line) then measuring the current while retracing the topography at a fixed distance between the sample and probe. (b) Schematic showing the SECM-AFM: The sample and probe have integrated working electrodes, and an applied bias voltage is set with respect to the reference electrode. Dual SECM-AFM probes allow for integration with an AFM to correlate electrochemical data with local topography. (c) Detection of transport through a single pore by SECM: A porous sample separates a receptor solution from a donor solution containing reduced redox mediators, creating a concentration gradient. Mediators are reduced at the sample working electrode (yellow) and oxidized at the probe working electrode (blue), where they are detected.

In addition to providing a clear assessment of the relative contributions arising from diffusive and iontophoretic transport, SECM offers another key advantage: It offers chemical selectivity due to the ability to sweep operative electrode potentials, a capability not intrinsic to another incisive method, scanning ion-conductance microscopy (SICM).[19] There are other notable advantages that the local nature of SECM measurements provide to studies of transport that go beyond new information on flow in confinement. The local imaging allows decoupling of the intrinsic effects of nanoconfinement from the redox activity due to surface geometry.[13] Additionally, utilization of this technique, and extension into combined SECM-AFM, allows for characterization of active pore densities of typical and novel filtration membranes. Membrane features that appear to be pores active to transport in AFM topography images do not necessarily

correspond to active pores by SECM current measurements,[5] and mapping active versus inactive pores on a given membrane surface provides valuable information on where synthesis methods can be improved for the development of more efficient membranes. Combined SECM-AFM is highly applicable to more broadly characterizing filtration selectivity and understanding the effect of novel film architectures designed for improvements in efficient flow while maintaining desired species rejection rates and sensitivity to fouling.

5.2 Early Investigations of Conductive Thin Films and Membranes

This research was conducted using an SECM-AFM from Asylum Research. The instrument is based on the MFP-3D-BIO AFM and consists of two major components that enable SECM imaging: (1) an electrochemical sample cell and (2) a probe holder with electrical connections. The sample cell and probe are then connected to a CH Instruments 700E potentiostat to regulate the applied working potentials. Dual-function electrochemical probes from Scuba Probe Technologies allow for collection of traditional tapping-mode AFM images, including topography and phase, while also enabling collection of current images through applied voltages, all with sub-50 nm resolution. The complete instrumental setup and probes are pictured in **Figure 5.2**. The time resolution for a combined SECM-AFM scan is limited by the probe, specifically the mechanical response of the cantilever in tapping mode and is 0.25 Hz. Static measurements improve the time resolution to 1.0 Hz for a sacrifice in spatial information and are limited by the response of the potentiostat.

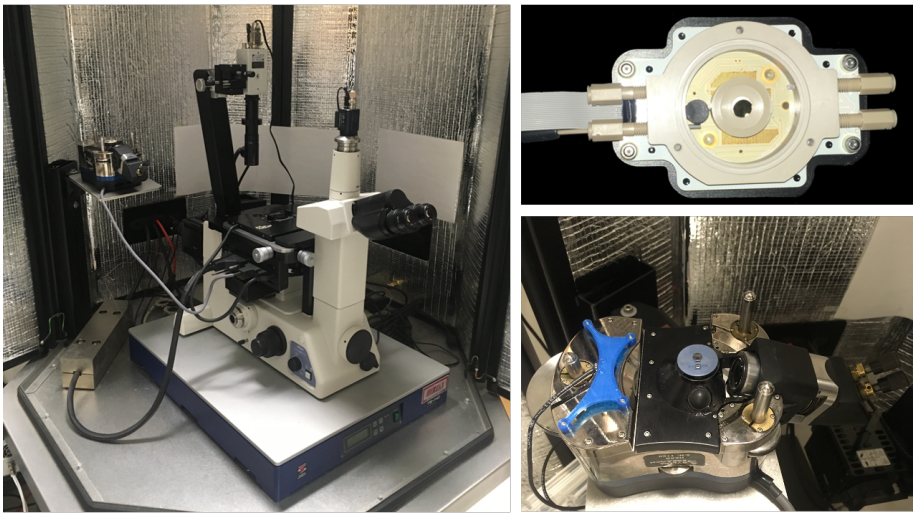

Figure 5.2 SECM-AFM Instrument. The instrumental setup includes the MFP-3D BIO AFM (left) and an electrochemical sample holder (top right) from Asylum Research, and dual-function insulated probes with connections to a potentiostat (bottom right).

As a preliminary experiment, a conductive and insulating polymer blend film was investigated, specifically poly(3-hexylthiophene-2,5-diyl) (P3HT) and poly(methyl methacrylate) (PMMA) blends on an indium tin oxide (ITO) substrate, as illustrated in **Figure 5.3**. The sample was submerged in a solution of ferrocene dimethanol redox reagent and a potassium chloride electrolyte; an example potential curve of the redox reaction at the cantilever tip is included in **Figure 5.3**. The P3HT bandgap matches that of the ferrocene complex, allowing measurable electron transfer between the two compounds. Enhanced redox activity at regions corresponding to the sites of elevated, conductive P3HT islands were identified, as shown in **Figure 5.3**.

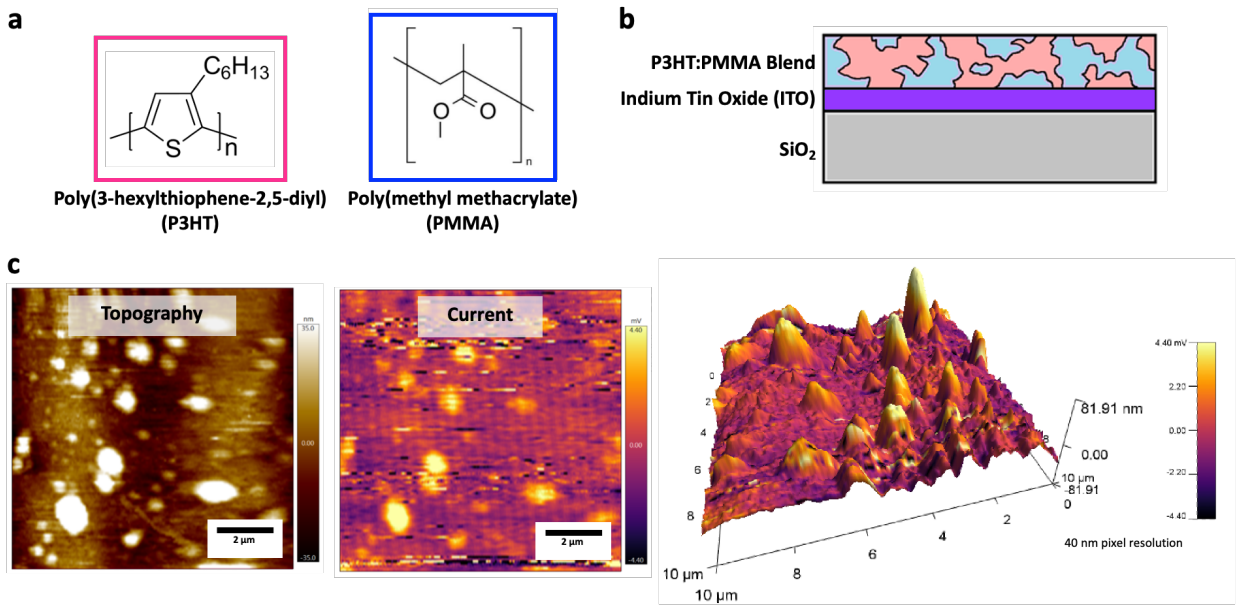

Figure 5.3 Imaging Conductive Polymer Blends. (a) Chemical structures for P3HT (*left*) and PMMA (*right*). (b) Schematic representation of the P3HT:PMMA blends on the ITO and SiO_2 substrate. (c) SECM-AFM images of polymer thin films: Topography and current images of 1:1 blend P3HT:PMMA thin film with 40 nm pixel resolution. The sample was immersed in an aqueous redox mediator solution of ferrocene dimethanol and potassium chloride. Current images were acquired with an applied voltage of 5.00 mV. Mapping of electrochemistry data on topography information confirms that areas of higher redox current correspond to the conductive P3HT islands with higher topography, as demonstrated by the current overlay on the topography image.

Commercial track-etched membranes from Millipore Sigma of various pore sizes, porosities, and thicknesses were then imaged to help identify the instrumental conditions required for membrane transport experiments. A comparison of these membranes imaged on the Cypher AFM and SECM-AFM are displayed in **Figure 5.4**. The Cypher has higher resolution imaging in both the topography and phase images than the SECM-AFM, but the images appear similar between the two instruments. Pores are not directly visible in either of the AFM images but are clearly seen in the current images. These pores are consistently visible across many samples and were identifiable at 0.4 and 0.1 µm pore sizes, shown in **Figure 5.4b**. To achieve these images, a constant voltage was applied to the sample working electrode, with the tip biased

with an opposite charge. The tip voltage is gated such that there is no current applied to the tip while doing an AFM scan, i.e., during the topography and phase imaging. As such, the pores are visible as separate from the surrounding membrane structure due to the diffusion of the redox mediator between the tip and underlying sample mount.

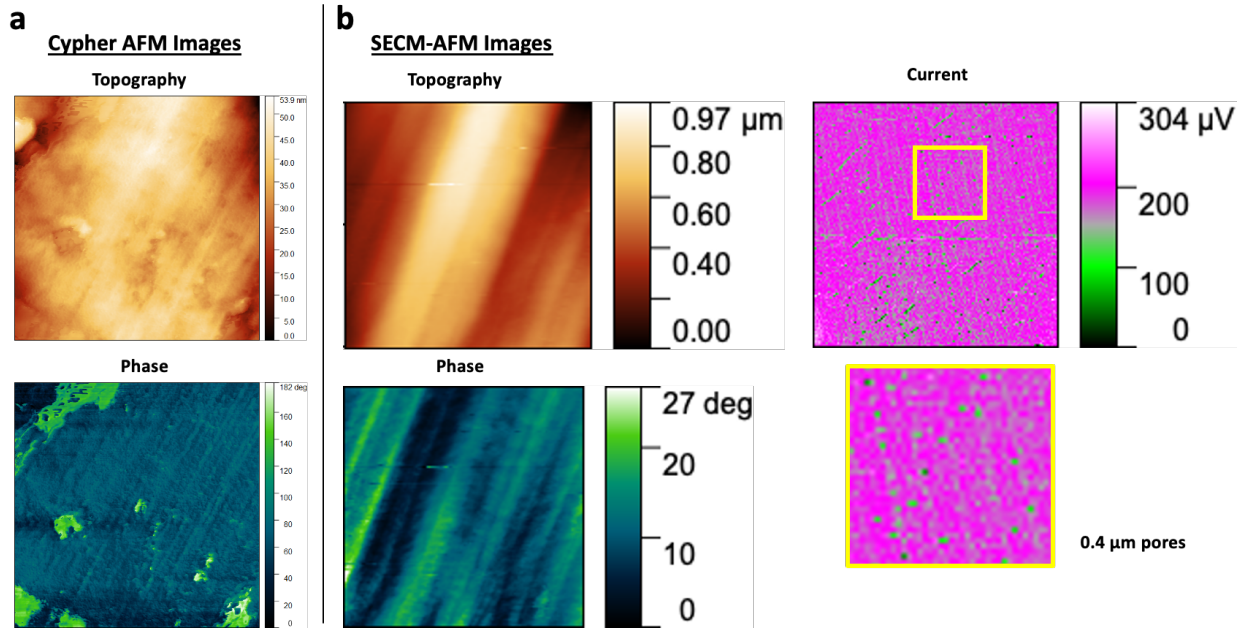

Figure 5.4 Comparison of AFM and SECM-AFM Imaging. (a) Representative topography and phase images of a Millipore Sigma Isopore™ membrane with 0.4 µm pore sizes collected in tapping mode acquired on an Asylum Research Cypher AFM. (b) SECM-AFM images of the same membranes, acquired in a KCl electrolyte solution with hexammineruthenium (III) chloride redox mediator with an applied tip current of 5 V. The measured current differences appear to correspond to the sample pore structures, which are not identifiable in any of the topography of phase scans.

5.3 Characterization of Transport through Membranes

Ultimately, the goal is to image transport through a membrane without the membrane directly mounted to an electrode, as was the case in the experiments described above. This would enable characterization of membrane transport through a single pore with SECM-AFM, with movement towards analyzing the impacts of changes in the membrane environment. To this end, I designed a custom dual-chamber membrane sample holder that suspends the membranes in solution, as

depicted in **Figure 5.5**. In this sample holder, the membrane is clamped in place and separates an electrolyte solution reservoir from the surrounding solution, allowing diffusive or iontophoretic transport through the membrane. Perfusion channels are located on the side of the reservoir, which enable control of the solution concentration while imaging. The sample holder fits into the electrochemical cell with the original working and reference electrodes.

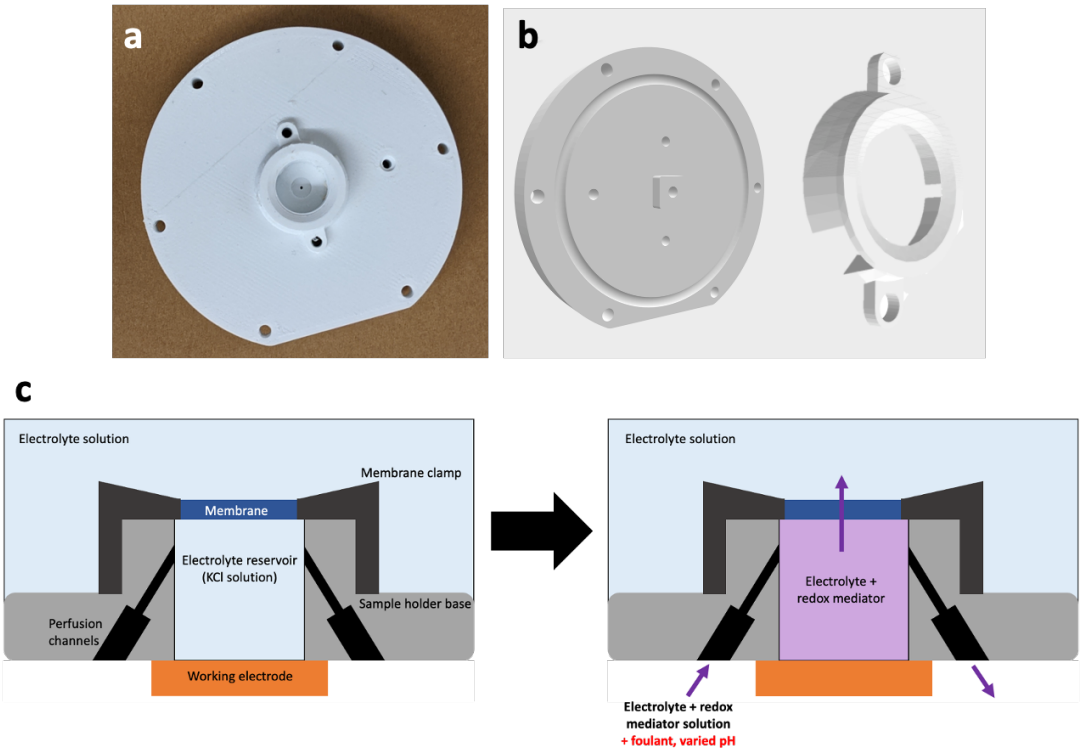

Figure 5.5 Membrane sample holder. (a) Picture of 3D printed custom dual-chamber membrane sample holder and (b) detailed designs of the underside (*left*) and membrane clamp (*right*). The clamp holds a membrane in place, which separates an electrolyte reservoir from the surrounding solution. (c) Schematic depiction of the experimental setup for transport experiments with the membrane sample holder. Perfusion channels provide control over the concentration and makeup of the electrolyte reservoir solution, allowing establishment of concentration gradients *in situ*.

This homebuilt membrane sample holder allows for the establishment of concentration gradients *in situ*, thus allowing for characterization of the response to solution changes on a single pore level. For example, upon the introduction of foulants, change of pH, or increase in redox mediator concentration, changes in the local flux or membrane topography and phase can be measured *in situ*; an example of this experimental setup is depicted in the schematic in **Figure 5.5c**. The redox mediator serves as a proxy to ion flow, allowing us to relate transport through the membranes to *in operando* environments and conditions. Additionally, the limited topography and slow time resolution that arise from limits in the dynamic feedback and tip positioning while scanning can be overcome through static measurements. In static experiments, pores of interest can be identified through the simultaneous acquisition of topography and current images, as in the dynamic SECM-AFM imaging. After a pore is selected, we can zoom in and remain over this pore to collect current measurements without scanning. This increases the time resolution to 1 Hz, enabling us to track changes in the membrane transport through time or as the operational environment is changed. This setup not only allows for characterization of commercial membranes, but also novel transport materials, such as molybdenum disulfide or Janus membranes,[20-21] that are designed to meet the efficiency and specificity required for modern filtration requirements. These measurements will present a window into the inhomogeneities present in membrane media *via* characterization of individual pore structure with correlated measurements of transport.

5.4 Summary and Outlook

In summary, SECM in concert with correlated AFM imaging provides an arguably unique information-rich probe of flows emanating from isolated pores and well-characterized local regions of membrane materials. Our early imaging with commercial membrane samples highlights the potential of this technique to identify and image pores that are not visible with AFM alone. The custom membrane sample holder will enable characterization of flux through membranes on the single-pore level, providing data on chemically and structurally specific structures. These data will allow for critical tests of our fundamental understanding of transport in nanostructures and confinement.

5.5 Methods

5.5.1 Instrumentation

Experiments were performed on an Asylum Research SECM-AFM, consisting of an electrochemistry cell and electrochemical tip holder housed on an MFP-3D BIO AFM. A CH Instruments Model 700E bipotentiostat was used to regulate applied voltages on the working electrodes (at the tip and sample) against an Ag/AgCl reference electrode on the tip, and a carbon counter electrode closed the circuit. Dual-functional electrochemical cantilevers were purchased from Scuba Probe Technologies. The silicon nitride cantilevers are coated with an insulating layer of silica and have an exposed platinum tip, and a polyimide handle connects the cantilever to a Pyrex chip, enabling electrical connection to the bipotentiostat. The exposed tip height is about 1.7 μm, and the cantilever resonant frequency is about 26 kHz in water (spring constant = 0.8 N/m) for tapping mode AFM and a lead resistance less than 20 Ω.

5.5.2 P3HT-PMMA Experiments

Polymer of samples 1:1 and 1:5 blends of Poly(3-hexylthiophene-2,5-diyl) (P3HT):poly(methyl methacrylate) (PMMA) on indium tin oxide (ITO) and on silicon dioxide substrates were made and provided by Asylum Research. Samples were mounted on stainless steel AFM pucks from Leitsilber Conductive Silver Cement from Ted Pella and submerged in a 100 mM potassium chloride (KCl) electrolyte solution with 5 mM ferrocenedimethanol redox mediator. SECM-AFM images were acquired with an applied voltage of 5.0 mV at 0.5 Hz per line, with 128 lines and 256 points per image, and a drive amplitude of 100 mV.

5.5.3 Membrane experiments

Isopore^{TM} Membrane Filters were purchased from Millipore Sigma. These hydrophilic polycarbonate track-etched membranes had pore sizes of 0.1 and 0.4 μm, with porosities of 4.18% and 10-20%, respectively. The membranes were mounted on stainless steel AFM pucks from Leitsilber Conductive Silver Cement from Ted Pella and submerged in a 100 mM potassium chloride (KCl) electrolyte solution with 5 mM hexaaminеruthenium (III) chloride redox mediator in deionized water. SECM-AFM images were acquired with a 5.0 V applied voltage at 0.5 Hz per line, with 128 points and lines per image, and a drive amplitude of 100 mV.

5.5.4 Membrane Sample Holder

The dual-chamber membrane sample holder was designed and 3D-printed with an Ultimaker 3 printer. The main body of the sample holder is made with a polylactic acid (PLA) resin, and natural PVA support material was used during the printing process and removed in water, according to manufacturer instructions.

References.

Chapter 1

1. J. G. Murphy, J. G. Raybin, S. J. Sibener. *J. Polym. Sci.* **2022**, *60*, 1042-1058.
2. G. J. Vancso, H. Schönherr. *Scanning Force Microscopy of Polymers*, Springer-Verlag, Berlin Heidelberg **2010**.
3. M. E. McConney, S. Singamaneni, V. V. Tsukruk *Polym. Rev.* **2010**, *50*, 235–286.
4. D. Wang, T. P. Russell *Macromolecules* **2018**, *22*, 3-24.
5. G. H. Michler, *Appl. Spectrosc. Rev.* **1993**, *28*, 327–384.
6. B. Chu, B. S. Hsiao, *Chem. Rev.* **2001**, *101*, 1727–1762.
7. A. Hexemer, P. Müller-Buschbaum, *IUCrJ* **2015**, *2*, 106–125.
8. J. S. Trent, J. I. Scheinbeim, P. R. Couchman, *Macromolecules* **1983**, *16*, 589–598.
9. C. G. Bischak, C. L. Hetherington, Z. Wang, J. T. Precht, D. M. Kaz, D. G. Schlom, N. S. Ginsberg, *Nano Lett.* **2015**, *15*, 3383–3390.
10. T. Albrecht, G. Strobl, *Macromolecules* **1996**, *29*, 783–785.
11. D. Posselt, J. Zhang, D.-M. Smilgies, A. V. Berezkin, I. I. Potemkin, C. M. Papadakis, *Prog. Polym. Sci.* **2017**, *66*, 80–115.
12. G. Binnig, C. F. Quate, Ch. Gerber, *Phys. Rev. Lett.* **1986**, *56*, 930–933.
13. B. Drake, C. B. Prater, A. L. Weisenhorn, S. A. Gould, T. R. Albrecht, C. F. Quate, D. S. Cannell, H. G. Hansma, P. K. Hansma, *Science* **1989**, *243*, 1586–1589.
14. T. Ando, N. Kodera, E. Takai, D. Maruyama, K. Saito, A. Toda, *PNAS* **2001**, *98*, 12468–12472.
15. R. García, R. Pérez, *Surf. Sci. Rep.* **2002**, *47*, 197–301.
16. R. Garcia, E. T. Herruzo, *Nat. Nanotechnol.* **2012**, *7*, 217–226.
17. Y. F. Dufrêne, T. Ando, R. Garcia, D. Alsteens, D. Martinez-Martin, A. Engel, C. Gerber, D. J. Müller, *Nat. Nanotechnol.* **2017**, *12*, 295–307.
18. R. Garcia, *Chem. Soc. Rev.* **2020**, *49*, 5850–5884.
19. H. G. Hansma, J. H. Hoh, *Annu. Rev. Biophys.* **1994**, *23*, 115–140.

20. H. G. Hansma, L. I. Pietrasanta, I. D. Auerbach, C. Sorenson, R. Golan, P. A. Holden, *J. Biomater. Sci. Polym. Ed.* **2000**, *11*, 675–683.

21. S. Liu, Y. Wang, *Scanning* **2010**, *32*, 61–73.

22. F. J. Giessibl *Jpn. J. Appl. Phys.* **1994**, *33*, 3726-3734.

23. F. J. Giessibl *Jpn. J. Appl. Phys.* **1994**, *33*, 3726-3734.

24. L. Chen, X. Gu, M. J. Fasolka, J. W. Martin, T. Nguyen, *Langmuir*, **2009**, 25, 3494–3503.

25. C. Marcuello, L. Foulon, B. Chabbert, V. Aguié-Béghin, M. Molinari, *Int. J. Biol. Macromol.* **2020**, *147*, 1064-1075.

26. M. J. Fasolka, A. M. Mayes, S. N Magonov, *Ultramicroscopy* **2001**, *90*, 21-31.

27. Y. Kikkawa, H. Abe, M. Fujita, T. Iwata, Y. Inoue, Y. Doi, *Macromol. Chem. Phys.* **2003**, *204*, 1822-1831.

28. J.-J. Zhou, J.-G. Liu, S.-K. Yan, J.-Y. Dong, L. Li, C.-M. Chan, J. M. Schultz, *Polymer* **2005**, *46*, 4077-4087.

29. P. K. Hansma, J. P. Cleveland, M. Radmacher, D. A. Walters, P. E. Hillner, M. Bezanilla, M. Fritz, D. Vie, H. G. Hansma, C. B. Prater, J. Massie, L. Fukunaga, J. Gurley, V. B. Elings, *Appl. Phys. Lett.* **1994**, *64*, 1738–1740.

30. J. P. Cleveland, B. Anczykowski, A. E. Schmid, V. B. Elings, *Appl. Phys. Lett.* **1998**, *72*, 2613–2615.

31. D. Raghavan, X. Gu, T. Nguyen, M. VanLandingham, A. Karim, *Macromolecules* **2000**, *33*, 2573–2583.

32. R. Proksch, D. G. Yablon, *Appl. Phys. Lett.* **2012**, *100*, 073106.

33. R. Proksch, M. Kocun, D. Hurley, M. Viani, A. Labuda, W. Meinhold, J. Bemis, *J. Appl. Phys.* **2016**, *119*, 134901.

34. R. Proksch, *Appl. Phys. Lett.* **2006**, *89*, 113121.

35. S. Santos, C.-Y. Lai, T. Olukan, M. Chiesa, *Nanoscale* **2017**, *9*, 5038–5043.

36. G. Benstetter, R. Biberger, D. Liu, *Thin Solid Films* **2009**, *517*, 5100–5105.

37. W. Melitz, J. Shen, A. C. Kummel, S. Lee, *Surf. Sci. Rep.* **2011**, *66*, 1–27.

38. J. Jahng, D. A. Fishman, S. Park, D. B. Nowak, W. A. Morrison, H. K. Wickramasinghe, E. O. Potma, *Acc. Chem. Res.* **2015**, *48*, 2671–2679.

39. A. Dazzi, C. B. Prater, *Chem. Rev.* **2017**, *117*, 5146–5173.

40. C. L. Bentley, J. Edmondson, G. N. Meloni, D. Perry, V. Shkirskiy, P. R. Unwin, *Anal. Chem.* **2019**, *91*, 84–108.

41. T. Ando, T. Uchihashi, T. Fukuma, *Prog. Surf. Sci.* **2008**, *83*, 337–437.

42. T. Ando, *Nanotechnology* **2012**, *23*, 062001.

43. T. Ando, T. Uchihashi, N. Kodera, *Annu. Rev. Biophys.* **2013**, *42*, 393–414.

44. T. Ando, *Curr. Opin. Struct. Bio.* **2014**, *28*, 63–68**.**

45. P. K. Hansma, G. Schitter, G. E. Fantner, C. Prater, *Science* **2006**, *314*, 601–602.

46. D. A. Walters, J. P. Cleveland, N. H. Thomson, P. K. Hansma, M. A. Wendman, G. Gurley, V. Elings, *Rev. Sci. Instrum.* **1996**, *67*, 3583–3590.

47. G. E. Fantner, G. Schitter, J. H. Kindt, T. Ivanov, K. Ivanova, R. Patel, N. Holten-Andersen, J. Adams, P. J. Thurner, I. W. Rangelow, P. K. Hansma, *Ultramicroscopy* **2006**, *106*, 881–887.

48. T. Sulchek, R. Hsieh, J. D. Adams, S. C. Minne, C. F. Quate, D. M. Adderton, *Rev. Sci. Instrum.* **2000**, *71*, 2097–2099.

49. A. D. L. Humphris, M. J. Miles, J. K. Hobbs, *Appl. Phys. Lett.* **2005**, *86*, 034106.

50. T. E. Schäffer, J. P. Cleveland, F. Ohnesorge, D. A. Walters, P. K. Hansma, *J. Appl. Phys.* **1996**, *80*, 3622–3627.

51. S. Tien, Qingze Zou, S. Devasia, *IEEE Trans. Contr. Syst. Technol.* **2005**, *13*, 921–931.

52. A. Labuda, K. Kobayashi, D. Kiracofe, K. Suzuki, P. H. Grütter, H. Yamada, *AIP Advances* **2011**, *1*, 022136.

53. A. Labuda, K. Kobayashi, Y. Miyahara, P. Grütter, *Rev. Sci. Instrum.* **2012**, *83*, 053703.

54. A. Labuda, S. Hohlbauch, M. Kocun, F. T. Limpoco, N. Kirchhofer, B. Ohler, D. Hurley, *Micros. Today* **2018**, *26*, 12–17.

55. N. Kodera, D. Yamamoto, R. Ishikawa, T. Ando, *Nature* **2010**, *468*, 72–76.

56. T. Fukui, T. Uchihashi, N. Sasaki, H. Watanabe, M. Takeuchi and K. Sugiyasu, *Angew. Chem. Int. Ed.* **2018**, *57*, 15465–15470.

57. K. Ushimaru, S. Mizuno, A. Honya, H. Abe, T. Tsuge, *ACS Omega* **2017**, *2*, 181–185.

58. J. Raybin, J. Ren, X. Chen, R. Gronheid, P. F. Nealey, S. J. Sibener, *Nano Lett.* **2017**, *17*, 7717–7723.

59. T. Brouns, H. De Keersmaecker, S. F. Konrad, N. Kodera, T. Ando, J. Lipfert, S. De Feyter, W. Vanderlinden, *ACS Nano* **2018**, *12*, 11907–11916.

60. Y. Zhang, M. Hashemi, Z. Lv, B. Williams, K. I. Popov, N. V. Dokholyan, Y. L. Lyubchenko, *J. Chem. Phys.* **2018**, *148*, 123322.

61. J. A. Kretzmann, C. W. Evans, L. Feng, N. B. Lawler, M. Norret, M. J. Higgins, K. S. Iyer, *Langmuir* **2020**, *36*, 9074–9080.

62. M. Soliman, Y. Ding, L. Tetard, *J. Phys.: Condens. Matter* **2017**, *29*, 173001.

63. E.-C. Spitzner, C. Riesch, R. Magerle, *ACS Nano* **2011**, *5*, 315–320.

64. D. Ebeling, B. Eslami, S. D. J. Solares, *ACS Nano* **2013**, *7*, 10387–10396.

65. L. Mester, A. A. Govyadinov, S. Chen, M. Goikoetxea, R. Hillenbrand, *Nat. Commun.* ***2020***, *11*, 3359.

66. B. Cappella, G. Dietler, *Surf. Sci. Rep.* **1999**, *34*, 1–104.

67. H.-J. Butt, B. Cappella, M. Kappl, *Surf. Sci. Rep.* **2005**, *59*, 1–152.

68. A. A. Tseng, *Small* **2011**, *7*, 3409–3427.

69. R. Garcia, A. W. Knoll, E. Riedo, *Nature Nanotech* **2014**, *9*, 577–587.

70. Y. Krivoshapkina, M. Kaestner, I. W. Rangelow, *Frontiers of Nanoscience* (Eds: A. Robinson, R. Lawson), Elsevier, **2016**, 497–542.

71. M. Hirtz, M. K. Brinks, S. Miele, A. Studer, H. Fuchs, L. Chi, *Small* **2009**, *5*, 919–923.

72. J. Duvigneau, H. Schönherr, G. J. Vancso, *ACS Nano* **2010**, *4*, 6932–6940.

73. S. T. Howell, A. Grushina, F. Holzner, J. Brugger, *Microsyst. Nanoeng.* **2020**, *6*, 1–24.

74. G. Liu, S. H. Petrosko, Z. Zheng, C. A. Mirkin, *Chem. Rev.* **2020**, *120*, 6009–6047.

75. P. Vettiger, G. Cross, M. Despont, U. Drechsler, U. Durig, B. Gotsmann, W. Haberle, M. A. Lantz, H. E. Rothuizen, R. Stutz, G. K. Binnig, *IEEE Trans. Nanotechnol.* **2002**, *1*, 39–55.

76. M. Muthukumar, *Progress in Understanding of Polymer Crystallization* (Eds: G. Reiter, G. R. Strobl), Springer, Berlin, Heidelberg **2007.**

77. X. Tang, W. Chen, L. Li, *Macromolecules* **2019**, *17*, 3575-3591.

78. J. K. Hobbs, O. E. Farrance, L. Kailas, *Polymer*, **2009**, *50*, 4281–4292.

79. T. P. Lodge, *Macromolecules* **2017**, *50*, 9525–9527.

80. J. I. Lauritzen, J. D. Hoffman, *J. Res. Natl. Bur. Stand. A Phys. Chem.* **1960**, *64A*, 73–102.

81. T. Hugel, G. Strobl, R. Thomann, *Acta Polymerica* **1999**, *50*, 214–217.

82. L. Li, C.-M. Chan, K. L. Yeung, J.-X. Li, K.-M. Ng, Y. Lei, *Macromolecules* **2001**, *34*, 316–325.

83. G. Strobl, *Eur. Phys. J. E* **2000**, *3*, 165–183.

84. J. Kumaki, T. Kawauchi, E. Yashima, *J. Am. Chem. Soc.* **2005**, *127*, 5788–5789.

85. Y. Ono, J. Kumaki, *Macromolecules* **2018**, *51*, 7629–7636.

86. V. V. Korolkov, A. Summerfield, A. Murphy, D. B. Amabilino, K. Watanabe, T. Taniguchi. P. H. Beton, *Nat. Commun.* **2019**, *10*, 1537.

87. D. E. Acevedo-Cartagena, J. Zhu, M. Kocun, S. S. Nonnenmann, R. C. Hayward, *Macromolecules* **2019**, *52*, 7756–7761.

88. X. Lyu, Y. Song, W. Feng, W. Zhang, *ACS Macro Lett.* **2018**, *7*, 762–766.

89. Y. Song, Z. Ma, P. Yang, X. Zhang, X. Lyu, K. Jiang, W. Zhang, *Macromolecules* **2019**, *52*, 1327–1333.

90. K. Liu, Y. Song, W. Feng, N. Liu, W. Zhang, X. Zhang, *J. Am. Chem. Soc.* **2011**, *133*, 3226–3229.

91. C. M. Bates, M. J. Maher, D. W. Janes, C. J. Ellison, C. G. Willson, *Macromolecules* **2014**, *47*, 2–12.

92. R. Ruiz, H. Kang, F. A. Detcheverry, E. Dobisz, D. S. Kercher, T. R. Albrecht, J. J. de Pablo, P. F. Nealey, *Science* **2008**, *321*, 936–939.

93. F. Bates, G. Fredrickson, *Annu. Rev. Phys. Chem.* **1990**, *41*, 525–57.

94. S. B. Darling, *Prog. Polym. Sci.* **2007**, *32*, 1152–1204.

95. D. Sundrani, S. B. Darling, S. J. Sibener, *Langmuir* **2004**, *20*, 5091–5099.

96. S. Ouk Kim, H. H. Solak, M. P. Stoykovich, N. J. Ferrier, J. J. de Pablo, P. F. Nealey, *Nature* **2003**, *424*, 411–414.

97. Q. Tong, Q. Zheng, S. J. Sibener, *Macromolecules* **2014**, *47*, 4236–4242.

98. M. A. van Dijk, R. van den Berg, *Macromolecules* **1995**, *28*, 6773–6778.

99. A. Knoll, A. Horvat, K. S. Lyakhova, G. Krausch, G. J. A. Sevink, A. V. Zvelindovsky, R. Magerle, *Phys. Rev. Lett.* **2002**, *89*, 035501.

100. A. Knoll, R. Magerle, G. Krausch, *Macromolecules* **2001**, *34*, 4159–4165.

101. Q. Zhang, O. K. C. Tsui, B. Du, F. Zhang, T. Tang, T. He, *Macromolecules* **2000**, *33*, 9561–9567.

102. K. W. Gotrik, A. F. Hannon, J. G. Son, B. Keller, A. Alexander-Katz, C. A. Ross, *ACS Nano* **2012**, *6*, 8052–8059.

103. J. Hayat, I. Mitra, Y. Qiao, G. E. Stein, C. Tang, *Eur. Polym. J.* **2015**, *71*, 476–489.

104. H. Zhang, B. Wang, G. Wang, C. Shen, J. Chen, G. Reiter, B. Zhang, *Macromolecules* **2020**, *53*, 9631–9640.

105. K. Takano, T. Nyu, T. Maekawa, T. Seki, R. Nakatani, T. Komamura, T. Hayakawa, T. Hayashi, *RSC Adv.* **2020**, *10*, 70–75.

106. A. Modi, S. M. Bhaway, B. D. Vogt, J. F. Douglas, A. Al-Enizi, A. Elzatahry, A. Sharma, A. Karim, *ACS Appl. Mater. Interfaces* **2015**, *7*, 21639–21645.

107. M. Longanecker, A. Modi, A. Dobrynin, S. Kim, G. Yuan, R. Jones, S. Satija, J. Bang, A. Karim, *Macromolecules* **2016**, *49*, 8563–8571.

108. C. Harrison, D. H. Adamson, Z. Cheng, J. M. Sebastian, S. Sethuraman, D. A. Huse, R. A. Register, P. M. Chaikin, *Science* **2000**, *290*, 1558–1560.

109. J. Hahm, W. A. Lopes, H. M. Jaeger, S. J. Sibener, *J. Chem. Phys.* **1998**, *109*, 10111–10114.

110. J. Hahm, S. J. Sibener, *J. Chem. Phys.* **2001**, *114*, 4730–4740.

111. Q. Tong, S. J. Sibener, *Macromolecules* **2013**, *46*, 8538–8544.

112. H. J. Ryu, Q. Tong, S. J. Sibener, *J. Phys. Chem. Lett.* **2013**, *4*, 2890–2895.

113. F. Stehlin, F. Diot, A. Gwiazda, A. Dirani, M. Salaun, M. Zelsmann, O. Soppera, *Langmuir* **2013**, *29*, 12796–12803.

114. N. A. Yufa, J. Li, S. J. Sibener, *Polymer* **2009**, *50*, 2630–2634.

115. A. Chandra, R. Nakatani, T. Uchiyama, Y. Seino, H. Sato, Y. Kasahara, T. Azuma, T. Hayakawa, *Adv. Mater. Interfaces* **2019**, *6*, 1801401.

116. C. T. Bezik, J. J. de Pablo, *Macromolecules* **2020**, *53*, 10446–10456.

117. J. G. Raybin, J. G. Murphy, M. Dolejsi, S. J. Sibener, *ACS Nano* **2019**, *13*, 11741–11752.

118. B. Pollard, E. A. Muller, K. Hinrichs, M. B. Raschke, *Nat. Commun.*, **2014**, *5*, 3587.

119. D. Nowak, W. Morrison, H. K. Wickramasinghe, J. Jahng, E. Potma, L. Wan, R. Ruiz, T. R. Albrecht, K. Schmidt, J. Frommer, D. P. Sanders, S. Park, *Science Advances*, **2016**, *2*, e1501571.

120. L. Wang, H. Wang, M. Wagner, Y. Yan, D. S. Jakob, X. G. Xu, *Science Advances*, **2017**, *3*, e1700255.

121. L. S. C. Pingree, O. G. Reid, D. S. Ginger, *Advanced Materials* **2009**, *21*, 19–28.

122. M. Osaka, D. Mori, H. Benten, H. Ogawa, H. Ohkita, S. Ito, *ACS Appl. Mater. Interfaces* **2017**, *9*, 15615-15622.

123. N. Spampinato, G. Pecastaings, M. Maglione, G. Hadziioannou, E. Pavlopoulou, *Colloid Polym. Sci.* **2021**, *299*, 551–560.

124. O. G. Reid, K. Munechika, D. S. Ginger, *Nano Lett.* **2008**, *8*, 1602–1609.

125. E. Daviddi, Z. Chen, B. Beam Massani, J. Lee, C. L. Bentley, P. R. Unwin, E. L. Ratcliff, *ACS Nano* **2019**, *13*, 13271–13284.

126. M. Osaka, H. Benten, H. Ohkita, S. Ito, *Macromolecules* **2017**, *50*, 1618–1625.

127. C. Groves, O. G. Reid, D. S. Ginger, *Acc. Chem. Res.* **2010**, *43*, 612-620.

128. D. C. Coffey, O. G. Reid, D. B. Rodovsky, G. P. Bartholomew, D. S. Ginger, *Nano Lett.* **2007**, *7*, 738–744.

129. J. L. Luria, N. Hoepker, R. Bruce, A. R. Jacobs, C. Groves, J. A. Marohn, *ACS Nano* **2012**, *6*, 9392–9401.

130. S. Pont, F. Foglia, A. M. Higgins, J. R. Durrant, J. T. Cabral, *Adv. Funct. Mater.* **2018**, *28*, 1802520.

131. V. Abetz, *Macromol. Rapid Commun.* **2015**, *36*, 10–22.

132. A. Lee, J. W. Elam, S. B. Darling, *Environ. Sci.: Water Res. Technol.* **2016**, *2*, 17–42.

133. S. P. Nunes, *Macromolecules* **2016**, *49*, 2905–2916.

134. H.-C. Yang, Y. Xie, J. Hou, A. K. Cheetham, V. Chen, S. B. Darling, *Adv. Mater.* **2018**, *30*, 1801495.

135. D. J. Lyman, *ASAIO J.* **1963**, *9*, 92-96.

136. D. J. Lyman, B. H. Loo, R. W. Crawford, *Biochemistry* **1964**, *3*, 985–990.

137. S. P. Nunes, M. L. Sforça, K.-V. Peinemann, *J. Membr. Sci.* **1995**, *106*, 49–56.

138. S. Y. Yang, I. Ryu, H. Y. Kim, J. K. Kim, S. K. Jang, T. P. Russell, *Adv. Mater.* **2006**, *18*, 709–712.

139. K.-V. Peinemann, V. Abetz, P. F. W. Simon, *Nat. Mater.* **2007**, *6*, 992–996.

140. Z. Wang, X. Yao, Y. Wang, *J. Mater. Chem.* **2012**, *22*, 20542–20548.

141. R. Z. Waldman, H.-C. Yang, D. J. Mandia, P. F. Nealey, J. W. Elam, S. B. Darling, *Adv. Mater. Interfaces* **2018**, *5*, 1800658.

142. S. Y. Yang, I. Ryu, H. Y. Kim, J. K. Kim, S. K. Jang, T. P. Russell, *Adv. Mater.* **2006**, *18*, 709-712.

143. R. Z. Waldman, N. Jeon, D. J. Mandia, O. Heinonen, S. B. Darling, A. B. F. Martinson, *Chem. Mater.* **2019**, *31*, 5274–5285.

144. W. R. Bowen, T. A. Doneva, *Surf. Interface Anal.* **2000**, *29*, 544-547.

145. A. M. ElHadidy, S. Peldszus, M. I. Van Dyke, *J. Membr. Sci.* **2013**, *429*, 373–383.

146. D. Yu. Khanukaeva, A. N. Filippov, A. V. Bildyukevich, *Pet. Chem.* **2014**, *54*, 498–506.

147. K. Boussu, B. Van der Bruggen, A. Volodin, J. Snauwaert, C. Van Haesendonck, C. Vandecasteele, *J. Colloid Interface Sci.* **2005**, *286*, 632–638.

148. Y. Wyart, R. Tamime, L. Siozade, I. Baudin, K. Glucina, C. Deumié, P. Moulin, *J. Membr. Sci.* **2014**, *472*, 241–250.

149. A. J. Bard, F. R. F. Fan, J. Kwak, O. Lev, *Anal. Chem.* **1989**, *61*, 132-138.

150. J. V. Macpherson, P. R. Unwin, *Anal. Chem.* **2000**, *72*, 276-285.

151. S. Amemiya, A. J. Bard, F.-R. F. Fan, M. V. Mirkin, P. R. Unwin, *Annu. Rev. Anal. Chem.* **2008**, *1*, 95-131.

152. A. Davoodi, A. Farzadi, J. Pan, C. Leygraf, Y. Zhu, *J. Electrochem. Soc.* **2008**, *155*, C474-C485.

153. X. Shi, W. Qing, T. Marhaba, W. Zhang, *Electrochimica Acta* **2020**, *332*, 135472.

154. E. R. Scott, H. S. White, *Anal. Chem.* **1993**, *65*, 1537.

155. G. Liu, S. H. Petrosko, Z. Zheng and C. A. Mirkin, *Chem. Rev.*, **2020**, *120*, 6009–6047.

156. O. D. Uitto, H. S. White, *Anal. Chem.* **2002**, *74*, 4577-4582.

157. C. E. Gardner, P. R. Unwin, J. V. Macpherson, *Electrochem. Commun.* **2005**, *7*, 612-618.

158. P. J. Flory, *J. Chem. Phys.* **1941**, *9*, 660–660.

159. M. L. Huggins, *J. Chem. Phys.* **1941**, *9*, 440–440.

160. Y. Lai, Y. Hu, *Soft Matter* **2018**, *14*, 2619-2627.

161. J. G. Raybin, S. J. Sibener, *Macromolecules* **2019**, *52*, 5985–5994.

162. D. Messmer, O. Bertran, R. Kissner, C. Alemán, A. D. Schlüter, *Chem. Sci.* **2019**, *10*, 6125–6139.

163. A. D. Schlüter, A. Halperin, M. Kröger, D. Vlassopoulos, G. Wegner, B. Zhang, *ACS Macro Lett.* **2014**, *3*, 991–998.

164. K. Jalili, F. Abbasi, L. Behboodpour, *J. Mech. Behav. Biomed. Mater.* **2019**, *93*, 118–129.

165. M. R. Hibbs, B. A. Hernandez-Sanchez, J. Daniels, S. J. Stafslien, *Biofouling* **2015**, *31*, 613–624.

166. Y. Higaki, J. Nishida, A. Takenaka, R. Yoshimatsu, M. Kobayashi, A. Takahara, *Polymer Journal* **2015**, *47*, 811–818.

167. S. Guo, R. Quintana, M. Cirelli, Z. S. D. Toa, V. Arjunan Vasantha, E. S. Kooij, D. Jańczewski, G. J. Vancso, *Langmuir* **2019**, *35*, 8085–8094.

Chapter 2

1. C. Sagui, M. Grant, *Phys. Rev. E.* **1999**, *59*, 4175-4187.

2. I. M. Lifshitz, V. V. Slyozov, *J. Phys. Chem. Solids*, **1961**, *19*, 35-50.

3. C. Wagner, *Zeitschrift für Elektrochemie, Berichte der Bunsengesellschaft für physikalische Chemie* **1961**, *65*, 581-591.

4. A. J. Ardell, *Phys. Rev. Lett.* **1990**, *74*, 4960-4960.

5. G. Leptoukh, B. Strickland, C. Roland, *Phys. Rev. Lett.* **1995**, *74*, 3636-3639.

6. U. Gasser, E. R. Weeks, A. Schofield, P. N. Pusey, D. A. Weitz, *Science* **2001**, *292*, 258-262.

7. F. Haußer, A. Voigt, *Phys. Rev. B* **2005**, *72*, 035437.

8. Q. Tong, Q. Zheng, S. J. Sibener, **2014**, *47*, 4236-4242.

9. J. G. Raybin, J. G. Murphy, M. Dolejsi, S. J. Sibener, *ACS Nano*, **2019**, *13*, 11741-11752.

10. S. B. Darling, *Prog. Polym. Sci.* **2007**, *32*, 1152-1204.

11. C. M. Bates, M. J. Maher, D. W. Janes, C. J. Ellison, C. G. Willson, *Macromolecules,* **2013**, *47*, 2-12.

12. R. D. Peters, P. Stasiak, M. W. Matsen, K. Dalnoki-Veress, *ACS Macro Letters* **2013**, *2*, 441-445.

13. A. Chandra, R. Nakatani, T. Uchiyama, Y. Seino, H. Sato, Y. Kasahara, T. Azuma, T. Hayakawa, *Adv. Mater. Interfaces* **2019***, 6*, 1801401.

14. Y.-S. Sun, S.-W. Chien, J.-Y. Liou *Macromolecules,* **2010**, *43*, 7250-7260.

15. T. G. Stange, D. F. Evans, *Langmuir* **1997**, *13*, 4459-4465.

16. R. Limary, P. F. Green, *Langmuir* **2003**, *19*, 2419-2424.

17. A. P. Smith, J. F. Douglas, E. J. Amis, A. Karim, *Langmuir*, **2007**, *23*, 12380-12387.

18. K. Aissou, M. Kogelschatz, T. Baron, *Nanotechnology* **2009**, *20*, 095602.

19. R. D. Peters, K. Dalnoki-Veress, *Eur. Phys. J. E* **2012**, *35*, 132.

20. G. Madres, B. J. McCoy, *Phys. Chem. Chem. Phys.* **2003**, *5*, 5459-5466.

21. S. Lucas, P. Moskovkin, *Thin Solid Films* **2010**, *518*, 5355-5361.

22. D. A. Beysens, *Physica A* **1997**, *239*, 329-339.

23. I. Fortelný, A. Živný, *Polymer* **1995**, *36*, 4113-4118.

24. S. Joy, D. Ausserré, G. Brotons, Y. Gallot, *Eur. Phys. J. E* **2002**, *8*, 355-363.

25. G. Zhan, Z.-F. Cai, K. Strutyński, L. Yu, N. Herrmann, M. Martínez-Abadía, M. Melle-Franco, A. Mateo-Alonso, S. D. Feyter, *Nature,* **2022**, *603*, 835-840.

26. T. Sugimoto, *Adv. Colloid Interface Sci.* **1987**, *28*, 65-108.

27. X. Peng, J. Wickham, A. P. Alivisatos, *J. Am. Chem. Soc.* **1998**, *120*, 5343-5344.

28. D. V. Talapin, A. L. Rogach, M. Haase, H. Weller, *J. Phys. Chem. B* **2001**, *105*, 12278-12285.

29. C. K. Haas, J. M. Torkelson, *Phys. Rev. E.* **1997**, *55*, 3191-3201.

Chapter 3

1. J. G. Raybin, J. G. Murphy, M. Dolejsi, S. J. Sibener, *ACS Nano,* **2019**, *13*, 11741-11752.
2. S. B. Darling, *Prog. Polym. Sci.* **2007**, *32*, 1152−1204.
3. C. M. Bates, M. J. Maher, D. W. Janes, C. J. Ellison, C. G. Willson, *Macromolecules* **2013**, *47*, 2−12.
4. G. H. Fredrickson, F. S. Bates, *Annu. Rev. Mater. Sci.* **1996**, *26*, 501−550.
5. C. M. Bates, F. S. Bates, *Macromolecules* **2016**, *50*, 3−22.
6. C. Liu, A. Ramírez-Hernández, E. Han, G. S. W. Craig, Y. Tada, H. Yoshida, H. Kang, S. Ji, P. Gopalan, J. J. de Pablo, P. F. Nealey, *Macromolecules* **2013**, *46*, 1415−1424.
7. R. Ruiz, H. Kang, F. A. Detcheverry, E. Dobisz, D. S. Kercher, T. R. Albrecht, J. J. de Pablo, P. F. Nealey, *Science* **2008**, *321*, 936−939
8. D. Sundrani, S. B. Darling, S. J. Sibener, *Nano Lett.* **2004**, *4*, 273−276.
9. D. Sundrani, S. B. Darling, S. J. Sibener, *Langmuir* **2004**, *20*, 5091−5099.
10. J. Y. Cheng, C. A. Ross, E. L. Thomas, H. I. Smith, G. J. Vancso, *Adv. Mater.* **2003**, *15*, 1599−1602.
11. H. J. Ryu, Q. Tong, S. J. Sibener, *J. Phys. Chem. Lett.* **2013**, *4*, 2890−2895.
12. W. Li, M. Müller, *Prog. Polym. Sci.* **2015**, *54−55*, 47−75.
13. G. P. Garner, P. R. Delgadillo, R. Gronheid, P. F. Nealey, J. J. de Pablo, *Mol. Syst. Des. Eng.* **2017**, *2*, 567−580.
14. Q. Tong, Q. Zheng, S. J. Sibener, *Macromolecules* **2014**, *47*, 4236−4242.
15. W. Li, M. Müller, *Macromolecules* **2016**, *49*, 6126−6138.
16. S.-M. Hur, V. Thapar, A. Ramírez-Hernández, G. Khaira, T. Segal-Peretz, P. A. Rincon-Delgadillo, W. Li, M. Müller, P. F. Nealey, J. J. de Pablo, *Proc. Natl. Acad. Sci. U. S. A.* **2015**, *112*, 14144−14149.
17. C. C. Liu, C. J. Thode, P. A. R. Delgadillo, G. S. Craig, P. F. Nealey, R. Gronheid, *J. Vac. Sci. Technol., B* **2011**, *29*, 06F203.
18. M. P. Stoykovich, K. C. Daoulas, M. Müller, H. Kang, J. J. de Pablo, P. F. Nealey, *Macromolecules* **2010**, *43*, 2334−2342.
19. P. N. Patrone, G. M. Gallatin, *Macromolecules* **2012**, *45*, 9507−9516.

20. H. S. Suh, X. Chen, P. A. Rincon-Delgadillo, Z. Jiang, J. Strzalka, J. Wang, W. Chen, R. Gronheid, J. J. de Pablo, N. Ferrier, M. Doxastakis, P. F. Nealey, *J. Appl. Crystallogr.*. **2016**, *49*, 823−834.

21. T. A. Witten, L. Leibler, P. A. Pincus, *Macromolecules* **1990**, *23*, 824−829.

22. A. N. Semenov, *Macromolecules* **1993**, *26*, 6617−6621.

23. A. N. Semenov, *Macromolecules* **1994**, *27*, 2732−2735.

24. G. Srinivas, W. C. Swope, J. W. Pitera, *J. Phys. Chem. B* **2007**, *111*, 13734−13742.

25. G. E. Stein, J. A. Liddle, A. L. Aquila, E. M. Gullikson, *Macromolecules* **2010**, *43*, 433−441.

26. C. Want, G. E. Stein, A. W. Bosse, W. Wu, *AIP Conf. Proc.* **2011**, *1395*, 305−308.

27. V. Constantoudis, G. Papavieros, E. Gogolides, A. V. Pret, H. Pathangi, R. Gronheid, *J. Micro/Nanolith. MEMS MOEMS* **2017**, *16*, 024001-1−024001-9.

28. C. Cutler, J. W. Thackeray, J. DeSisto, J. Nelson, C.-B. Lee, M. Li, E. Aqad, X. Hou, T. Marangoni, J. Kaitz, R. Rena, C. A. Mack, *Proc. of SPIE* **2018**, *10587*, 1058707-1−1058707-11.

29. C. A. Mack, *J. Micro/Nanolith. MEMS MOEMS* **2018**, *17*, 041006-1−041006-6.

30. A. W. Bosse, *Macromol. Theory Simul.* **2010**, *19*, 399−406.

31. A. W. Bosse, *J. Vac. Sci. Technol., B* **2011**, *29*, 031803.

32. A. W. Bosse, *J. Vac. Sci. Technol., B* **2011**, *29*, 06F202.

33. R. Ruiz, L. Wan, R. Lopez, T. R. Albrecht, *Macromolecules* **2017**, *50*, 1037−1046.

34. D. F. Sunday, M. R. Hammond, C. Wang, W. Wut, D. M. Delongchamp, M. Tjio, J. Y. Cheng, J. W. Pitera, R. J. Kline, *ACS Nano* **2014**, *8*, 8426−8437.

35. D. F. Sunday, J. Ren, C. D. Liman, L. D. Williamson, R. Gronheid, P. F. Nealey, R. J. Kline, *ACS Appl. Mater. Interfaces* **2017**, *9*, 31325−31334.

36. T. Segal-Peretz, J. Ren, S. Xiong, G. Khaira, A. Bowen, L. E. Ocola, R. Divan, M. Doxastakis, N. J. Ferrier, J. J. de Pablo, P. F. Nealey, *ACS Nano* **2017**, *11*, 1307−1319.

37. C. Harrison, D. H. Adamson, Z. Cheng, J. M. Sebastian, S. Sethuraman, D. A. Huse, R. A. Register, P. M. Chaikin, *Science* **2000**, *290*, 1558−1560.

38. J. Hahm, W. A. Lopes, H. M. Jaeger, S. J. Sibener, *J. Chem. Phys.* **1998**, *109*, 10111−10114.

39. J. Raybin, J. Ren, X. Chen, R. Gronheid, P. F. Nealey, S. J. Sibener, *Nano Lett.* **2017**, *17*, 7717−7723.

40. L. Tsarkova, A. Knoll, R. Magerle, *Nano Lett.* **2006**, *6*, 1574−1577

41. L. Tsarkova, A. Horvat, G. Krausch, A. V. Zvelindovsky, G. J. Agur Sevink, R. Magerle, *Langmuir*, **2006**, *22*, 8089−8095.

42. N. A. Yufa, J. Li, S. J. Sibener, *Macromolecules* **2009**, *42*, 2667−2671.

43. P. K. Hansma, G. Schitter, G. E. Fantner, C. Prater, *Science* **2006**, *314*, 601−602.

44. C. Riesch, G. Radons, R. Magerle, *Phys. Rev. E* **2014**, *90*, 052101.

45. C. Riesch, G. Radons, R. Magerle, *Interface Focus* **2017**, *7*, 20160146.

46. D. F. Sunday, M. J. Maher, A. F. Hannon, C. D. Liman, S. Tein, G. Blachut, Y. Asano, C. J. Ellison, C. G. Willson, R. J. Kline, *Macromolecules* **2017**, *51*, 173-180.

47. J. P. Cleveland, B. Anczykowski, A. E. Schmid, V. B. Elings, *Appl. Phys. Lett.* **1998**, *72*, 2613−2615.

48. A. W. Bosse, E. K. Lin, R. L. Jones, A. Karim, *Soft Matter* **2009**, *5*, 4266−4271.

49. C. A. Mack, *J. Micro/Nanolith. MEMS MOEMS* **2013**, *12*, 033016-1−033016-10.

50. C. A. Mack, *J. Micro/Nanolith. MEMS MOESM* **2015**, *14*, 033502-1−033502-8.

51. K. R. Shull, A. M. Mayes, T. P. Russell, *Macromolecules* **1993**, *26*, 3929−3936.

52. T. Geisinger, M. Müller, K. Binder, *J. Chem. Phys.* **1999**, *111*, 5251−5258.

53. P. Mansky, T. P. Russell, C. J. Hawker, J. Mays, D. C. Cook, S. K. Satija, *Phys. Rev. Lett.* **1997**, *79*, 237−240.

54. J. L. Keddie, *Europhys. Lett.* **1994**, *27*, 59−64.

55. Z. Fakhraai, J. A. Forrest, *Phys. Rev. Lett.* **2005**, *95*, 025701.

56. Y. Zhang, R. Potter, W. Zhang, Z. Fakhraai, *Soft Matter* **2016**, *44*, 9115−9120.

57. K. Pearson, *Proc. Royal Soc. Lond.* **1895**, *58*, 240−242.

58. C. Yeung, A.-C. Shi, J. Noolandi, R. C. Desai, *Macromol. Theory Simul.* **1996**, *5*, 291−298.

59. M. R. Hammond, E. J. Kramer, *Macromolecules* **2006**, *39*, 1538−1544.

60. E. Jones, E. Oliphant, P. Peterson, *et. al.* SciPy: Open Source Scientific Tools for Python. **2001**, http://www.scipy.org/ (accessed February 13, 2018).

Chapter 4

1. F. S. Bates, G. H. Fredrickson, *Annu. Rev. Phys. Chem.* **1990**, *41*, 525-557.

2. S. B. Darling, *Progress in Polymer Science* **2007**, *32*, 1152−1204.

3. T. P. Bigioni, X.-M. Lin, T. T. Nguyen, E. I. Corwin, T. A. Witten, H. M. Jaeger, *Nature Materials* **2006**, *5*, 265-270.

4. C. C. Liu, C. J. Thode, P. A. R. Delgadillo, G. S. Craig, P. F. Nealey, R. Gronheid, *J. Vac. Sci. Technol B* **2011**, *29*, 06F203.

5. N. A. García, R. L. Davis, S. Y. Kim, P. M. Chaikin, R. A. Register, D. A. Vega, *RCS Adv.* **2014**, *4*, 38412-38417.

6. C. C. Liu, A. Ramírez-Hernández, E. Han, G. S. W. Craig, Y. Tada, H. Yoshida, H. Kang, S. Ji, P. Gopalan, J. J. de Pablo, P. F. Nealey, *Macromolecules* **2013**, *46*, 1415−1424.

7. S. Sundrani, S. J. Sibener, *Macromolecules* **2002**, *35*, 8531-8539.

8. S. Sundrani, S. B. Darling, S. J. Sibener, *Nano Lett.* **2004**, *4*, 273-276.

9. S. Sundrani, S. B. Darling; S. J. Sibener, *Langmuir* **2004**, *20*, 5091-5099.

10. P. Mansky, J. DeRouchey, T. P. Russel, J. Mays, M. Pitsikalis, T. Morkved, H. Jaeger, *Macromolecules* **1998**, *31*, 4399-4401.

11. C. C. Kathrein, W. Bai, J. A. Currian-Incorvia, G. Liontos, K. Ntetsikas, A. Avgeropoulos, A. Böker, L. Tsarkova, C. A. Ross, *Chem. Mater.* **2015**, *27*, 6890-6898.

12. H. U. Jeon, H. M. Jin, J. Y. Kim, S. K. Cha, J. H. Mun, K. E. Lee, J. J. Oh, T. Yun, J. Kim, S. O. Kim *Mol. Syst. Des. Eng.* **2017**, *2*, 560-566.

13. M. P. Stoykovich, H. Kang, K. Ch. Daoulas, G. Liu, C.-C. Liu, J. J. de Pablo, M. Müller, P. F. Nealey, *ACS Nano* **2007**, *1*, 168-175.

14. D. J. C. Herr, *The Extensibility of Optical Patterning via Directed Self-assembly of Nano-engineered Imaging Materials*; Montgomery Research Inc.: San Francisco, 2005; Vol. 18.

15. D. J. C. Herr, *Update on the Extensibility of Optical Patterning via Directed Self-assembly*. Montgomery Research Incorporated: San Francisco, 2006; Vol. 20.

16. Semiconductor Research Corporation and National Nanotechnology Initiative. *Directed Self Assembly of Materials for Patterning Workshop*; Madison, WI, 2005.

17. Q. Tong, Q. Zheng, S. J. Sibener, *Macromolecules* **2014**, *47*, 4236-4242.

18. U. Nagpal, M. Müller, P. F. Nealey, J. J. de Pablo, *ACS Macro Lett.* **2012**, *1*, 418-422.

19. H. Takahashi, N. Laachi, K. T. Delaney, S.-M. Hur, C. J. Weinheimer, D. Shykind, G. H. Fredrickson *Macromolecules* **2012**, *45*, 6253-6265.

20. Q. Tong, S. J. Sibener, *Macromolecules* **2013**, *46*, 8538-8544.

21. C. Harrison, D. H. Adamson, Z. Cheng, J. M. Sebastian, S. Sethuraman, D. A. Huse, R. A. Register, P. M. Chaikin, *Science* **2000**, *290*, 1558-1560.

22. J. Hahm, S. J. Sibener, *J. Chem. Phys.* **2001**, *114*, 4730-4740.

23. N. M. Abukhdeir, A. D. Rey, *N. J. Phys.* **2008**, DOI: 10.1088/1367-2630/10/6/063025

24. W. Li, M. Müller, *Annu. Rev. Chem. Biomol. Eng.* **2015**, *6*, 187-216.

25. S.-M. Hur, V. Thapar, A. Ramírez-Hernández, G. Khaira, T. Segal-Peretz, P. A. Rincon-Delgadillo, W. Li, M. Müller, P. F. Nealey, J. J. de Pablo, *PNAS* **2015**, *112*, 14144-14149.

26. W. Li, M. Müller, *Macromolecules* **2016**, *49*, 6126-6139.

27. S.-M. Hur, V. Thapar, A. Ramírez-Hernández, P. F. Nealey, J. J. de Pablo, *ACS Nano* **2018**, *12*, 9974-9981.

Chapter 5

1. E. Barry, R. Burns, W. Chen, G. X. De Hoe, J. M. M. De Oca, J. J. de Pablo, J. Dombrowski, J. W. Elam, A. M. Felts, G. Galli, J. Hack, Q. He, X. He, E. Hoenig, A. Iscen, B. Kash, H. H. Kung, N. H. C. Lewis, C. Liu, X. Ma, A. Mane, A. B. F. Martinson, K. L. Mulfort, J. Murphy, K. Mølhave, P. Nealey, Y. Qiao, V. Rozyyev, G. C. Schatz, S. J. Sibener, D. Talapin, D. M. Tiede, M. V. Tirrell, A. Tokmakoff, G. A. Voth, Z. Wang, Z. Ye, M. Yesibolati, N. J. Zaluzec, S. B. Darling, *Chem. Rev.* **2021**, *121*, 9450-9501.

2. A. J. Bard, F. R. F. Fan, J. Kwak, O. Lev, *Anal. Chem.* **1989**, *61*, 132−138.

3. A. J. Bard, G. Denuault, C. Lee, D. Mandler, D. O. Wipf, *Acc. Chem. Res.* **1990**, *23*, 357−363.

4. A. J. Bard, F.-R. F. Fan, D. T. Pierce, P. R. Unwin, D. O. Wipf, F. Zhou, *Science* **1991**, *254*, 68−74.

5. C. E. Gardner, P. R. Unwin, J. V. Macpherson, *Electrochem. Commun.* **2005**, *7*, 612−618.

6. T. S. Watkins, D. Sarbapalli, M. J. Counihan, A. S. Danis, J. Zhang, L. Zhang, K. R. Zavadil, J. A. Rodríguez-López, *J. Mater. Chem. A* **2020**, *8*, 15734−15745.

7. E. R. Scott, H. S. White, J. B. Phipps, *J. Membr. Sci.* **1991**, *58*, 71−87.

8. S. Nugues, G. Denuault, *J. Electroanal. Chem.* **1996**, *408*, 125−140.

9. B. D. Bath, R. D. Lee, H. S. White, E. R. Scott, *Anal. Chem.* **1998**, *70*, 1047−1058.

10. M. Edwards, D. Robinson, H. Ren, C. Cheyne, C. Tan, H. White, *Faraday Discuss.* **2018**, *210*, 9−28.

11. A. Holzinger, G. Neusser, B. J. Austen, A. Gamero-Quijano, G. Herzog, D. Arrigan, A. Ziegler, P. Walther, C. Kranz, *Faraday Discuss.* **2018**, *210*, 113−130.

12. S. Balme, F. Picaud, M. Lepoitevin, M. Bechelany, E. Balanzat, J.-M. Janot, *Faraday Discuss.* **2018**, *210*, 69− 85.

13. J. H. Bae, Y. Yu, M. V. Mirkin, *J. Phys. Chem. C* **2016**, *120*, 20651−20658.

14. T. Sun, D. Wang, M. V. Mirkin, *Faraday Discuss.* **2018**, *210*, 173−188.

15. L. Cao, X. He, Z. Jiang, X. Li, Y. Li, Y. Ren, L. Yang, H. Wu, *Chem. Soc. Rev.* **2017**, *46*, 6725−6745.

16. E. R. Scott, H. S. White, J. B. Phipps, *Anal. Chem.* **1993**, *65*, 1537−1545.

17. J. Kim, A. Izadyar, N. Nioradze, S. Amemiya, *J. Am. Chem. Soc.* **2013**, *135*, 2321−2329.

18. P. Pathirathna, R. J. Balla, D. T. Jantz, N. Kurapati, E. R. Gramm, K. C. Leonard, S. Amemiya, *Anal. Chem.* **2019**, *91*, 5446−5454.

19. P. Hansma, B. Drake, O. Marti, S. Gould, C. Prater, *Science* **1989**, *243*, 641−643.

20. E. Hoenig, S. E. Strong, M. Wang, J. M. Radhakrishnan, N. J. Zaluzec, J. L. Skinner, C. Liu *Nano Letters* **2020**, *20*, 7844-7851.

21. J. M. Montes de Oca, J. Dhanasekaran, A. Córdoba, S. B. Darling, J. J. de Pablo *ACS Nano* **2022**, *16,* 3768-3775.

Appendix A.

Supporting Information

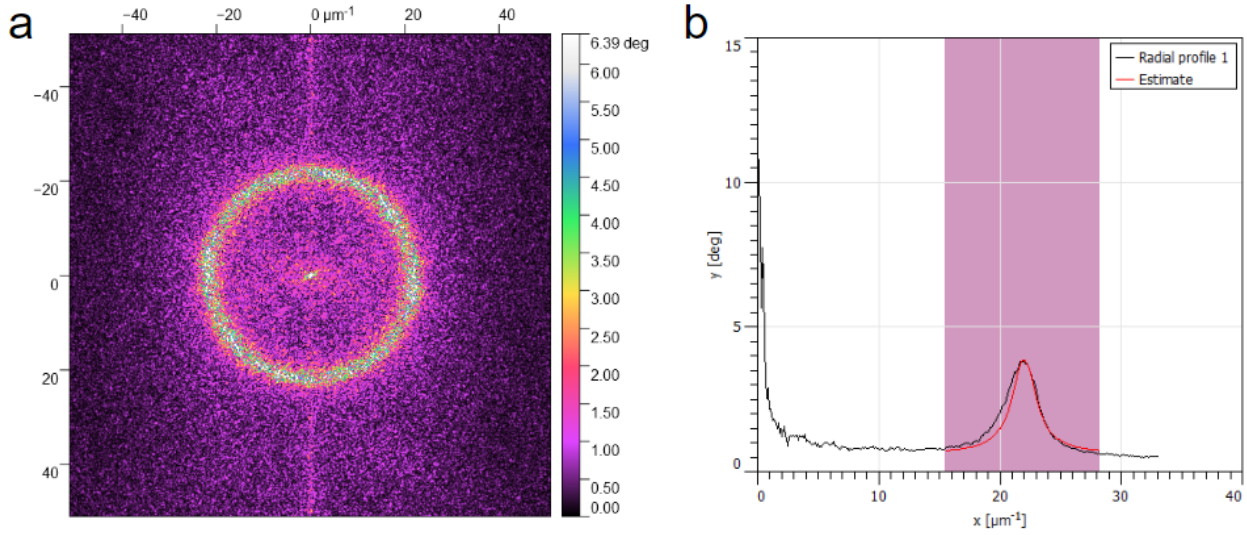

Figure SI.2.1. Measurement of L_0. (a) 2D Fourier transform of an AFM image of the PS-*b*-PMMA fingerprint pattern, with a ring pattern showing the periodicity in reciprocal space, obtained using Gwyddion analysis software. (b) Radially averaged plot of the 2D Fourier transform with a Lorentzian fit centered at 22.0 μm^{-1} and with a full-width at half-maximum of 2.4 μm^{-1}, corresponding to a real-space periodicity of 45.5 ± 0.4 nm.

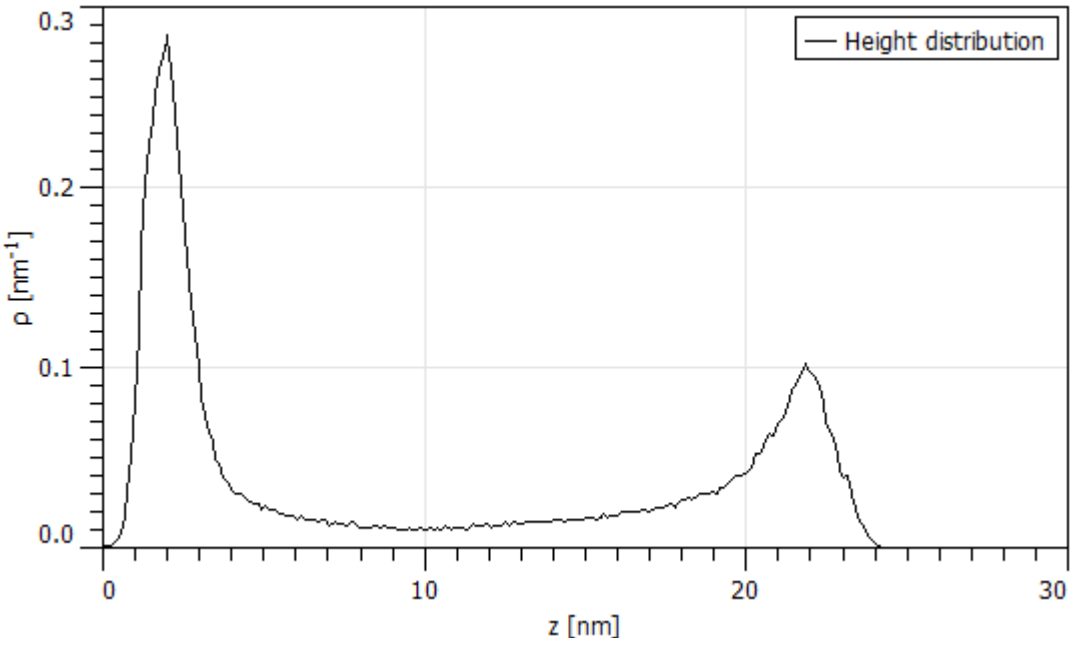

Figure SI.2.2. Measurement of $\Delta\tau$. Histogram showing the height distribution of a PS-*b*-PMMA film following *in situ* annealing. Peaks show the heights of the upper and lower terrace, corresponding to a height difference of 19.8 ± 1.8 nm, consistent with $\frac{1}{2}L_0$.

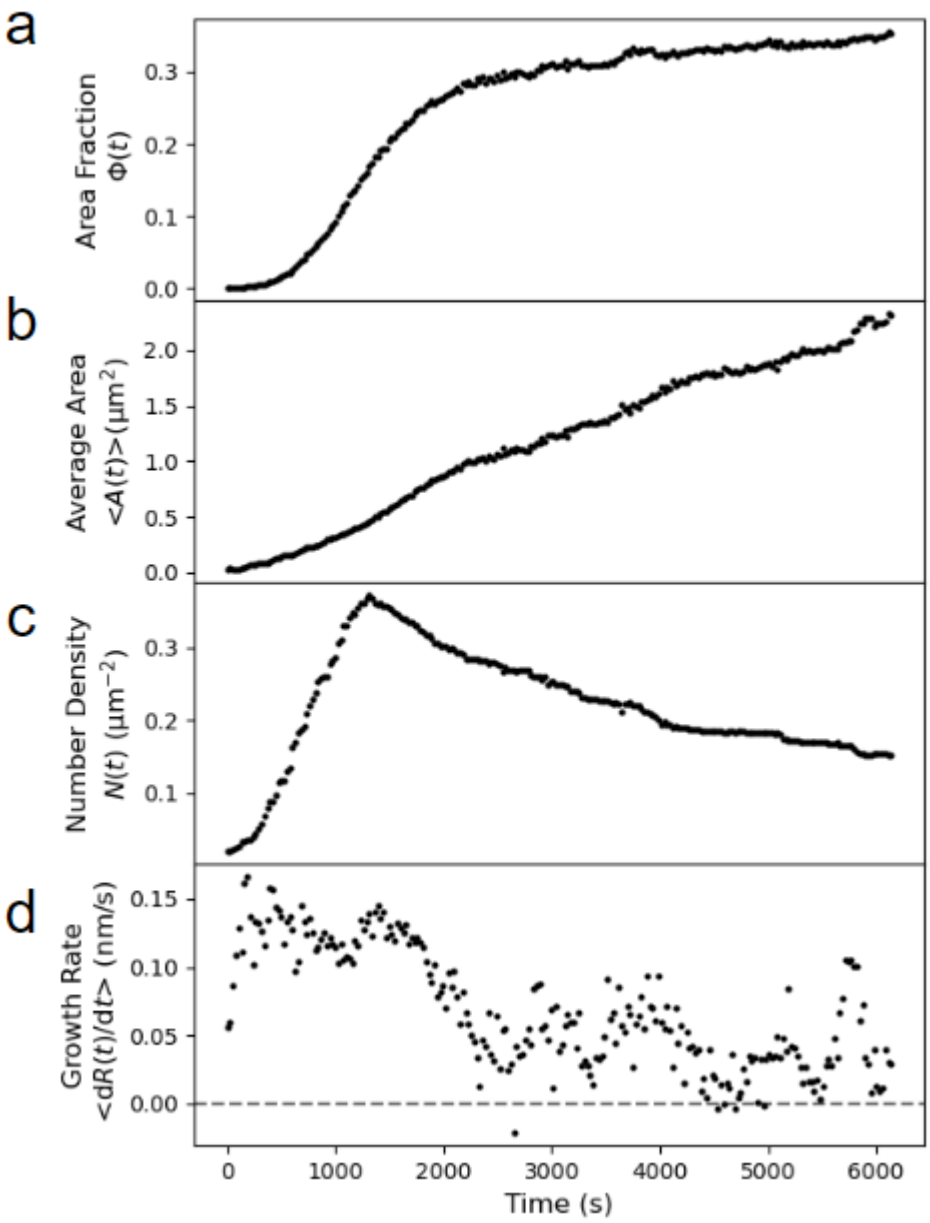

Figure SI.2.3. Ensemble Growth Statistics. Measurements over time of (a) the total hole area fraction $\Phi(t)$, (b) the average hole area $\langle A(t) \rangle$, (c) the hole number density $N(t)$, and (d) the average growth rate $\langle dR/dt \rangle$. Plots include the same data shown in the main paper in **Figure 2** plotted with a linear time scale.

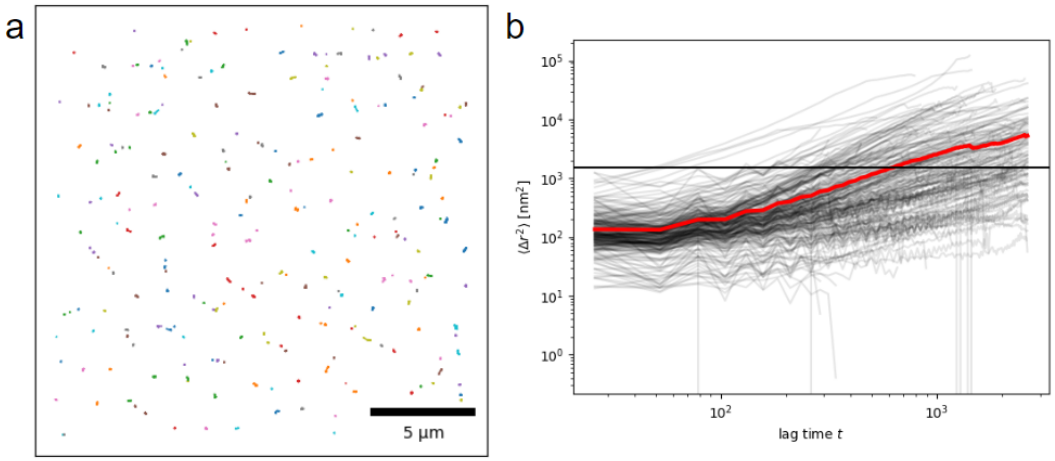

Figure SI.2.4. Center-of-Mass Motion. (a) Trajectories showing movement of the hole center-of-mass positions over time obtained using the trackpy Python library. (b) Plot of the individual and ensemble mean-square displacements (MSD) of the center-of-mass trajectories. Oscillations in the individual MSDs arise due to sub-pixel imaging hysteresis for up and down AFM scan directions. The horizontal line indicates the pixel resolution threshold and shows mean center-of-mass displacement of less than 2 pixels over the imaging period.

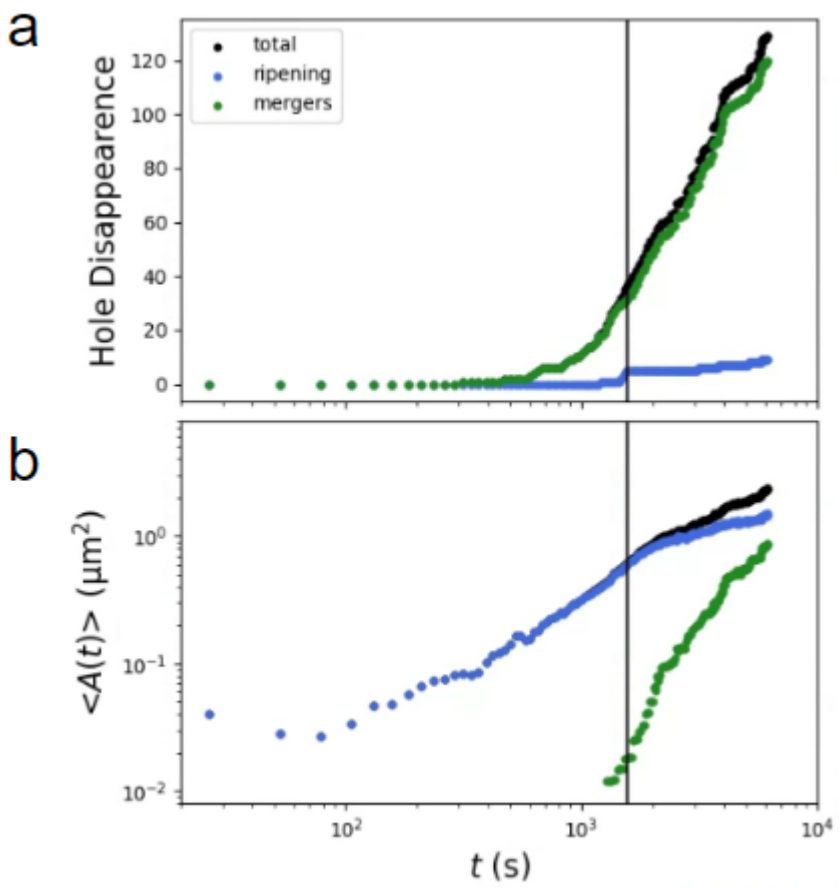

Figure SI.2.5. Contribution of Coalescence Mechanisms. (a) Cumulative count of hole disappearances over time due to evaporation (blue) or merger events (green). The majority of the decrease in number density is due to hole mergers. (b) Measure of the change in average hole area over time due to continuous ripening (blue) and discrete hole merger events (green). Continuous growth initially predominates but mergers become increasingly significant over time. In each plot, the vertical line marks the time for the onset of coarsening. After removing merger events, growth due ripening scales as $A \sim t^{1/2}$, lower than expected for capillarity-driven processes.

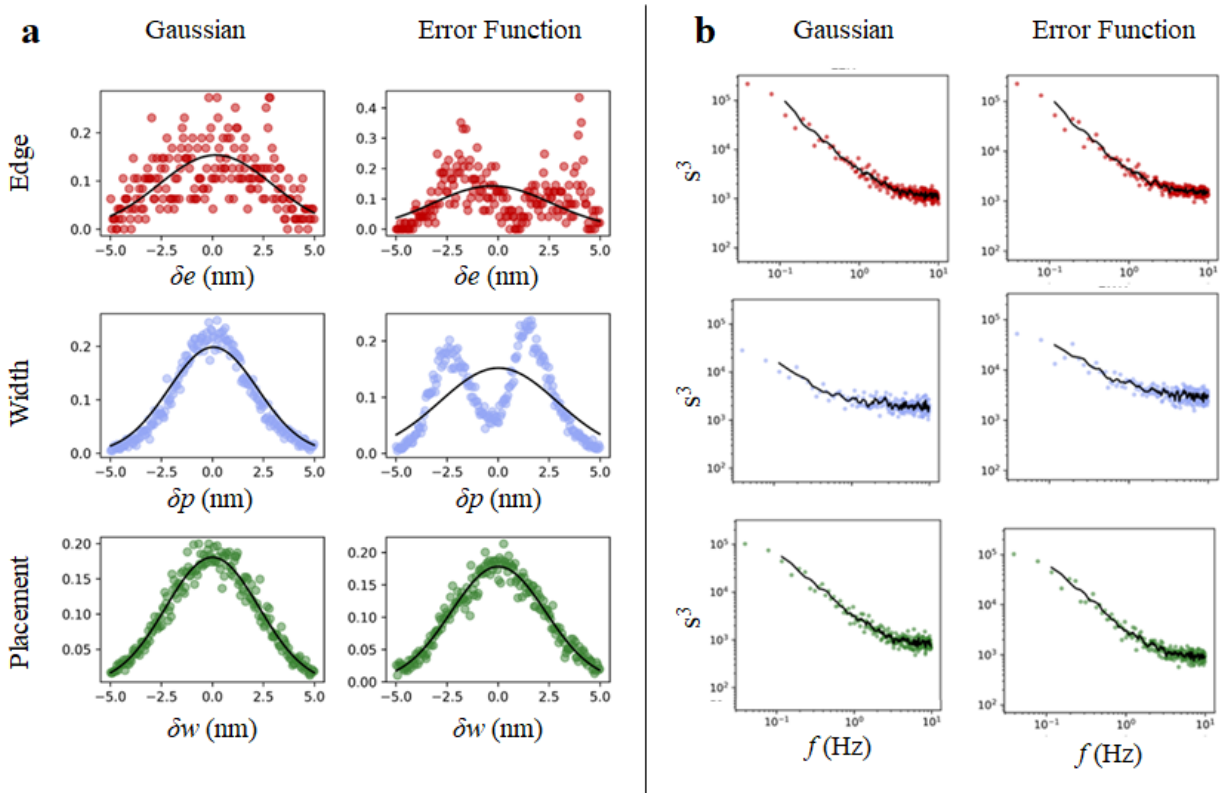

Figure SI.3.1. Gaussian Edge Fitting. (a) Distributions and (b) log-log plots of the temporal PSD for edge (red), position (blue), and width (green) measurements at 210 °C, as determined from two edge fitting methods. In the first method, we fit the derivative of the phase signal to a Gaussian; in the second, we directly model the phase data with an error function. Following the first procedure, the normal edge distribution illustrates that there is no spatial aliasing in edge detection. However, with the second fitting procedure, we observe a bimodal distribution of measured edges and widths, indicative of a lossy fit. We believe this may be due to the underlying optimization algorithm of SciPy curve fit resulting in clustering around pixel locations. Even with this "pixel-walking" effect, the PSD obtained from this data almost exactly matches that found from the Gaussian fit of the derivative. All subsequent analysis is performed using the first Gaussian fitting procedure.

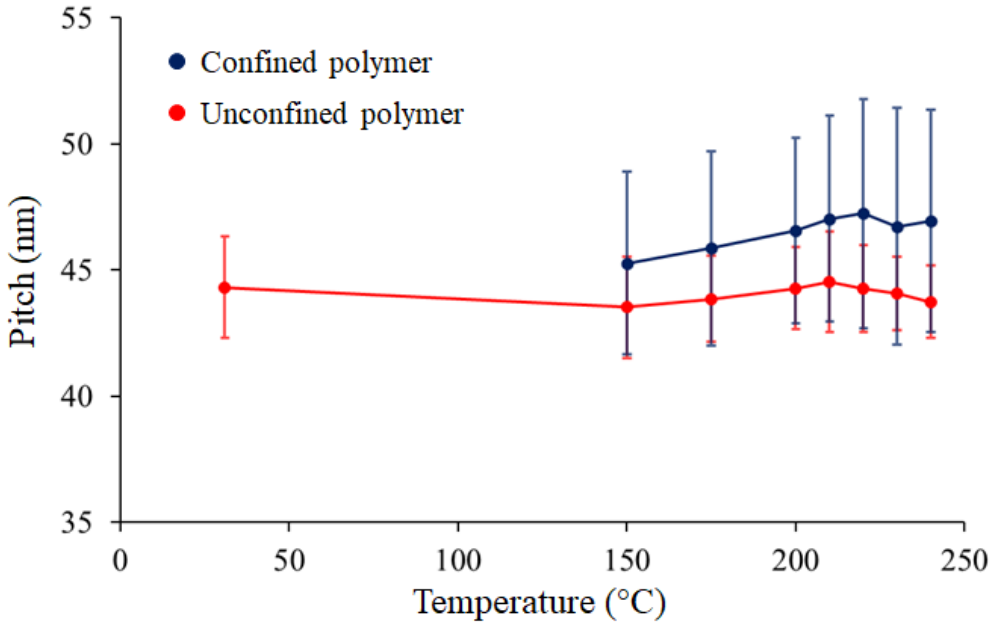

Figure SI.3.2. Pitch Variation with Temperature. Pitch measurements of confined (blue) and unconfined (red) polymer cylinders. Averaged over temperature, we find a confined pitch of 46.5 ± 4.1 nm and an unconfined pitch 44.1 ± 1.7 nm. The confined pitch is extended due to slight incommensurability with the Si trenches. These values were determined from the two-dimensional Fourier transform for unconfined polymer and from the one-dimensional Fourier transform for polymer confined in trenches. Error bars correspond to the full-width half-maximum of the spectral peak. Over the temperatures measured, we find that the pitch varies by less than 2 nm in the confined cylinders and by less than 1 nm in the unconfined cylinders.

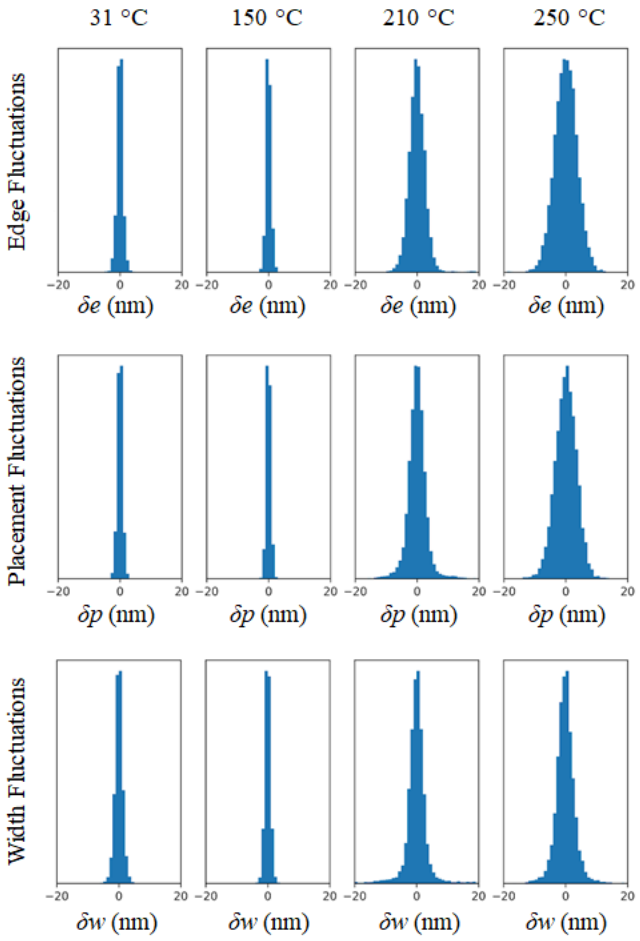

Figure SI.3.3. Fluctuation Distributions. Histograms of the residuals of edge, placement, and width cross correlations over temperature. Changes in commensurability, resulting from a changing χ with increased temperature, could potentially introduce asymmetry into width fluctuations. Incommensurability between the cylinder pitch and trench width leads to a bias toward contraction or expansion of the domains. The observed residuals across all temperatures are symmetric, indicating that the confining potentials are not significantly perturbed from equilibrium. In addition, the fluctuations at 31 and 150 °C have a similar narrow distribution, indicating that the roughness is comparable at both temperatures.

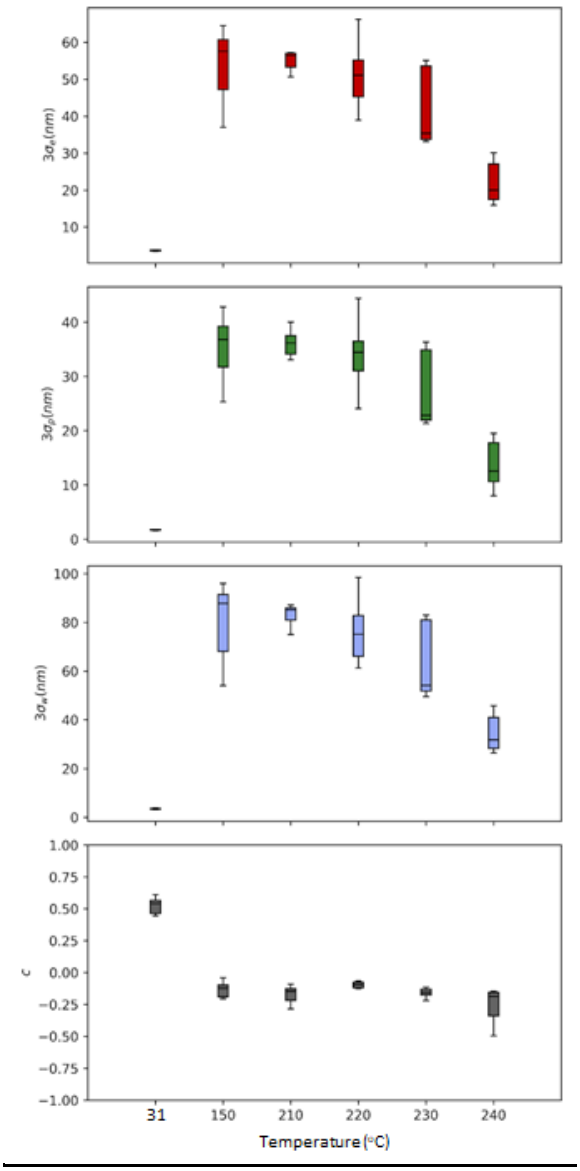

Figure SI.3.4. Roughness and Correlation of Si Trenches. Box plots comparing the distributions of measured roughness and correlation parameters of Si trench sidewalls without polymer across temperature. Roughness values are measured from AFM height images (rather than phase) and cannot be directly compared with polymer samples due to convolution with the AFM tip shape. At 31 °C, we find negligible fluctuation intensity, leading to an apparent increase in correlation. Above 150 °C, roughness increases and we measure no correlation between sidewall edges.

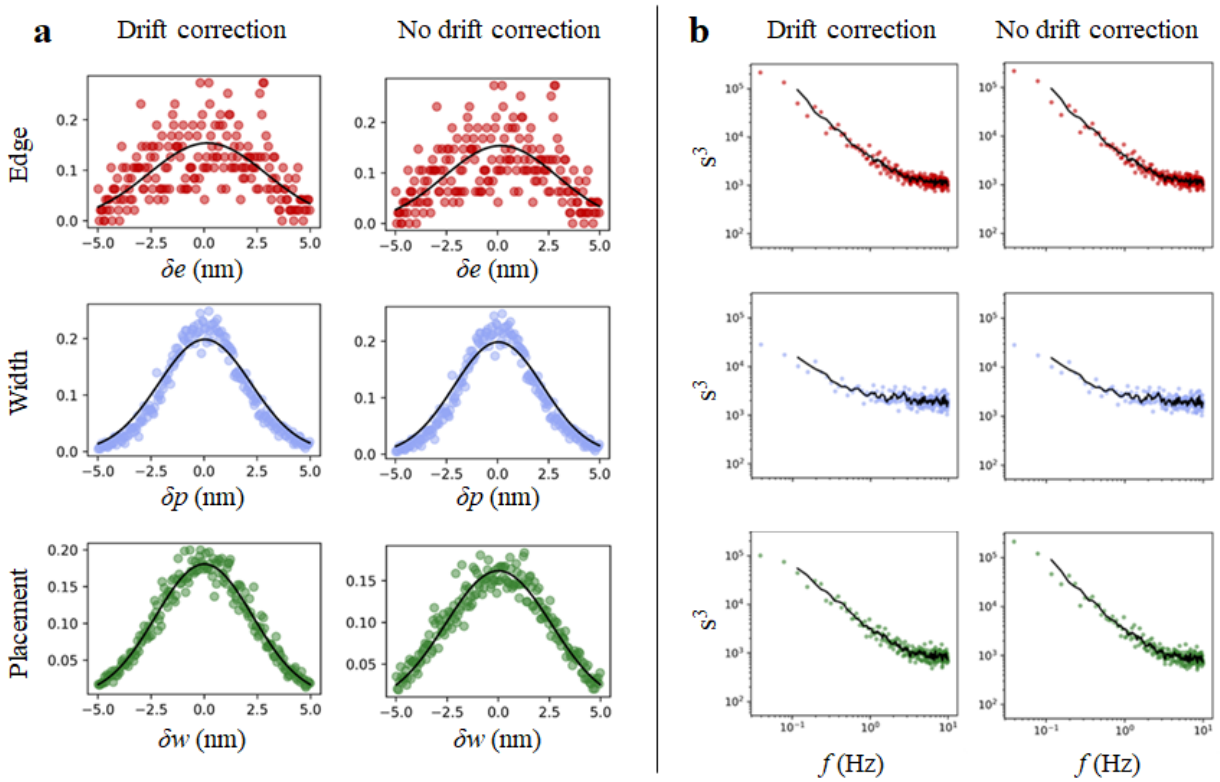

Figure SI.3.5 Drift Correction. (a) Distributions and (b) log-log plots of the temporal PSD for edge (red), position (blue), and width (green) measurements at 210 °C, analyzed with and without drift correction. Drift in the *x* and *y* scan directions is determined from AFM imaging of thermally equilibrated samples. The sample trajectories are corrected for drift in the *x* direction using a linear offset for all trajectories within each image. Imaging at the time scales of SSD AFM has minimal drift, less than 80 pm across the measurement time of a single image. We notice no deviation in either the distribution of the measured cylinder edges, positions, and widths when the drift correction is removed.

Appendix B.

Raw Data Referenced for Figures

This appendix includes raw image files referenced during the data analysis presented throughout this Thesis. Images were collected on an Asylum Cypher ES Environmental AFM and MFP-3D-BIO AFM with the SECM accessory. Each image presented here had minimal processing applied to it, and the specific processing is listed in the figure caption if applicable. Additionally, the file names and directories are included for data retrieval.

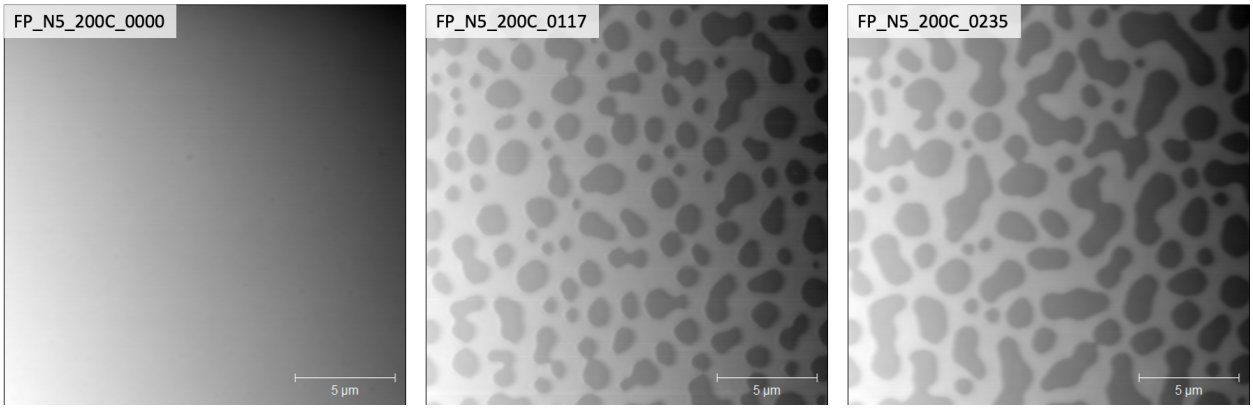

Figure A.2.1 Terrace Nucleation and Coarsening. Representative AFM topography images from the time series data used for **Figures 2.1-2.5**, taken on an Asylum Research Cypher ES AFM at 200 °C and under argon atmosphere. The full time series data is available electronically in the Sibener group.

Directory: 220515
File base name: FP_N5_200C_
File numbers: 0000-0235

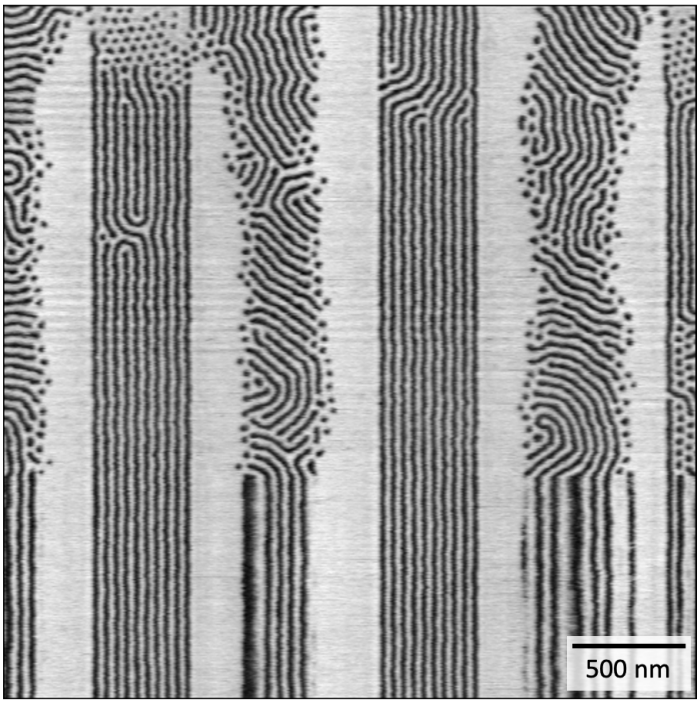

Figure A.3.1 Example Slow-Scan-Disabled AFM Image. Representative AFM phase image of PS-*b*-PMMA confined in lithographic trenches, with the slow-scan imaging axis disabled partway through collection of this image, used to create **Figure 3.1**. This was taken on an Asylum Cypher ES AFM at 220 ºC under argon atmosphere.

Directory: 170824
File base name: channels_220C_1D_
File numbers: 0001

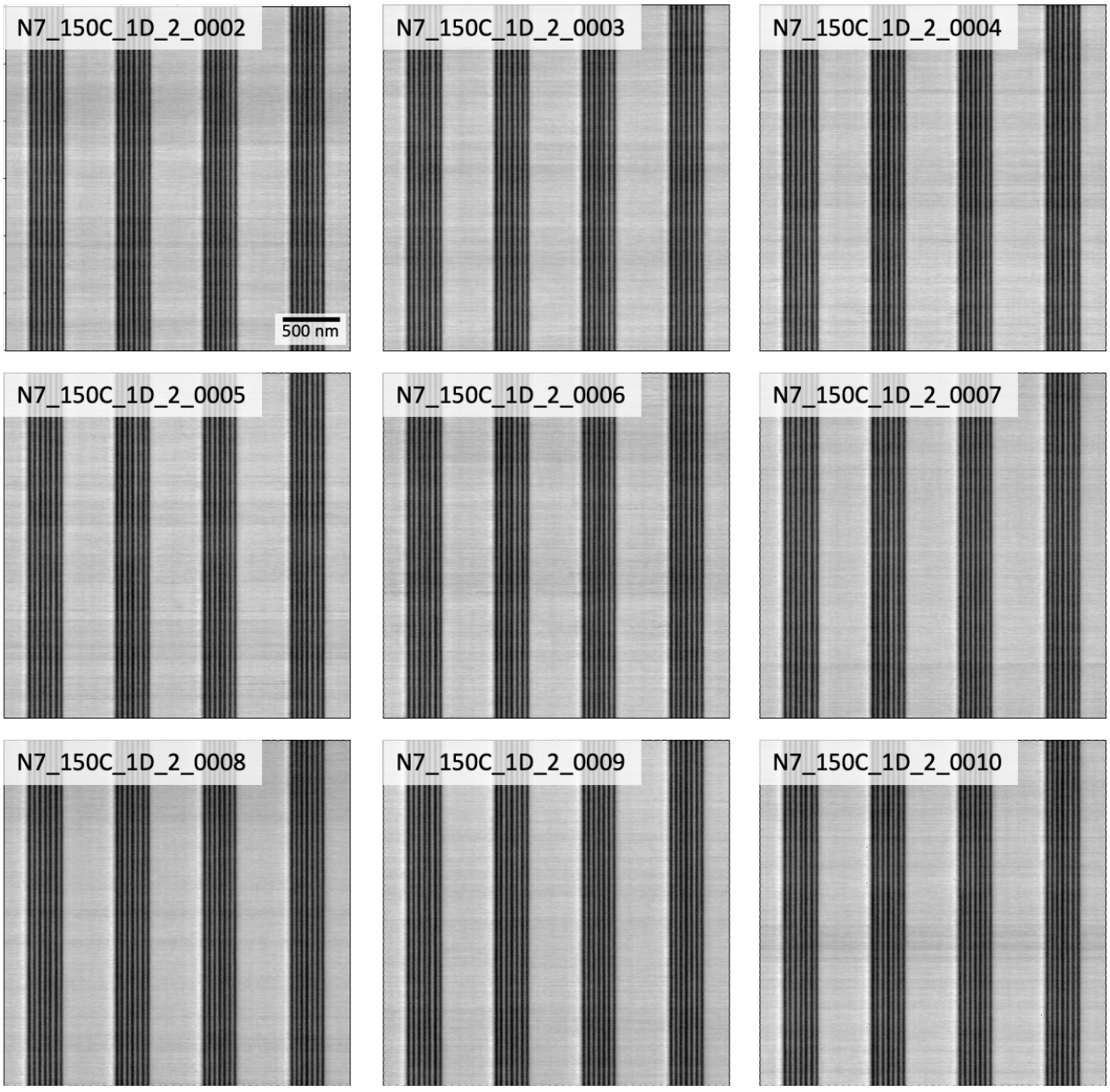

A.3.2 SSD AFM Phase Images at 150 °C. SSD AFM images taken on the Asylum Cypher ES at 150 °C under argon and used to create **Figures 3.4-3.7** and **Table 3.2**.

Directory: 180611
File base name: N7_150C_1D_2_
File numbers: 0002-0010

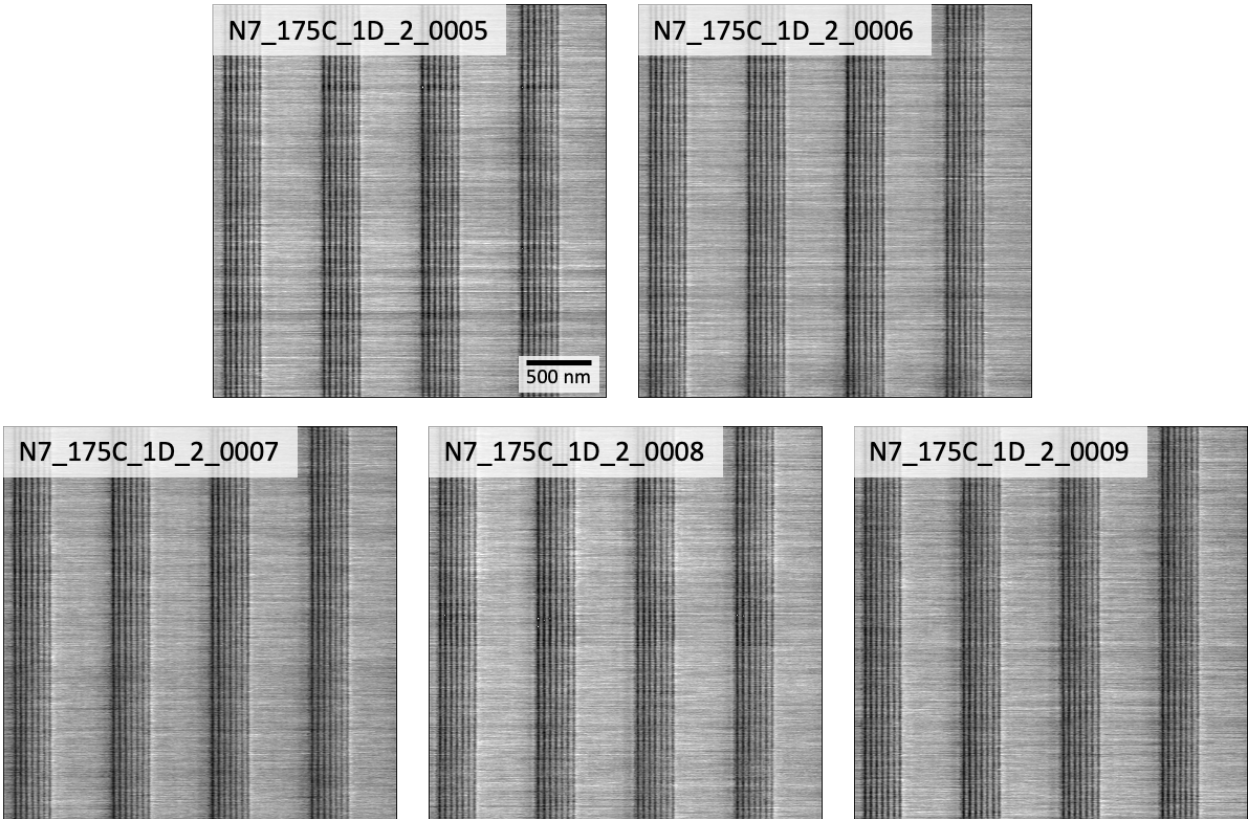

A.3.3 SSD AFM Phase Images at 175 ºC. SSD AFM images taken on the Asylum Cypher ES at 175 ºC under argon and used to create **Figures 3.5** and **Table 3.2**.

Directory: 180611
File base name: N7_175C_1D_2_
File numbers: 0005-0009

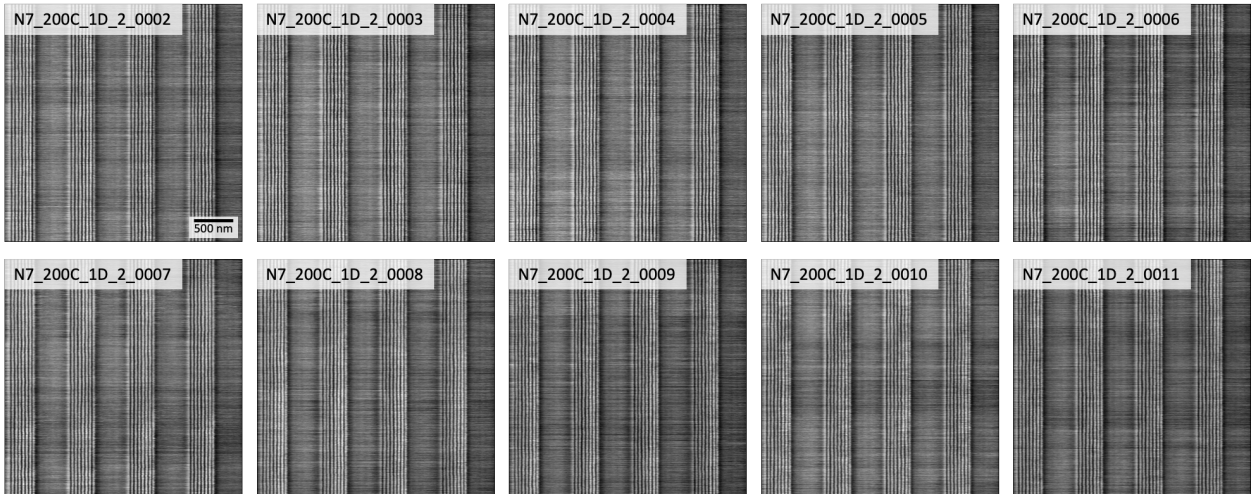

A.3.4 SSD AFM Phase Images at 200 ºC. SSD AFM images taken on the Asylum Cypher ES at 200 ºC under argon and used to create **Figures 3.5** and **Table 3.2**.

Directory: 180611
File base name: N7_200C_1D_2_
File numbers: 0002-0011

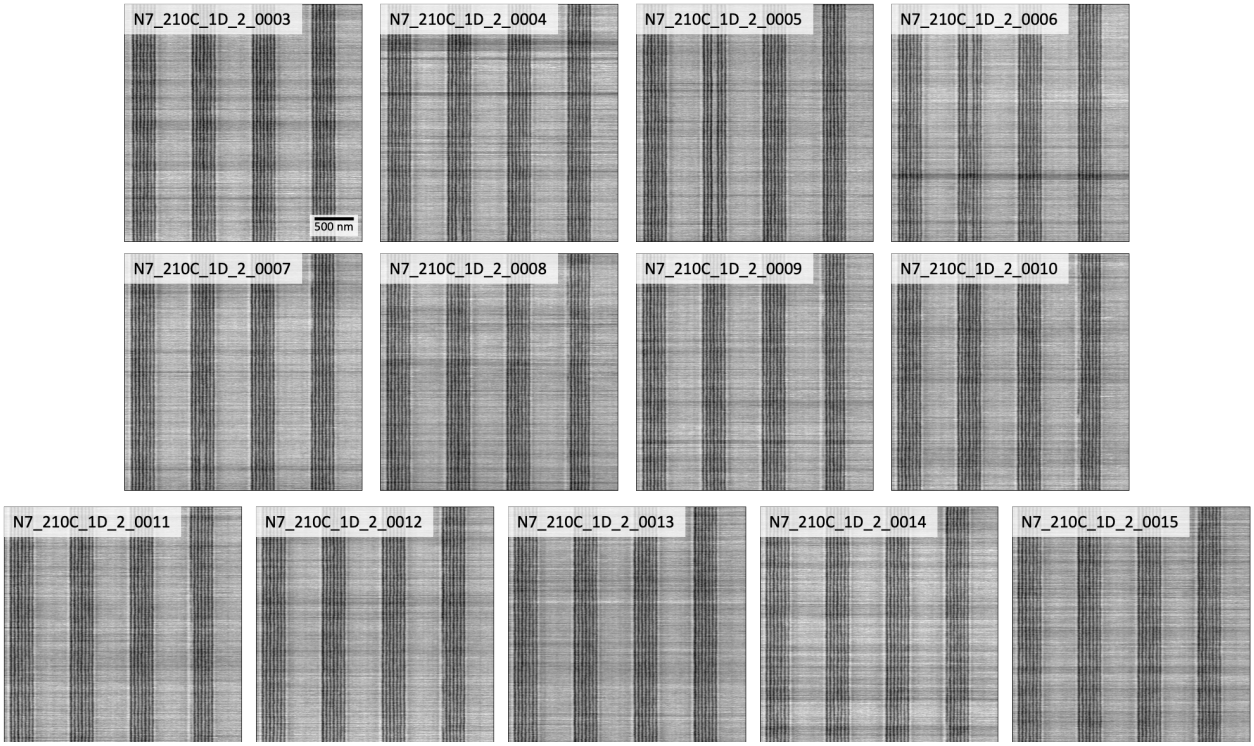

A.3.5 SSD AFM Phase Images at 210 ºC. SSD AFM images taken on the Asylum Cypher ES at 210 ºC under argon and used to create **Figures 3.4-3.7** and **Table 3.2**.

Directory: 180611
File base name: N7_210C_1D_2_
File numbers: 0003-0015

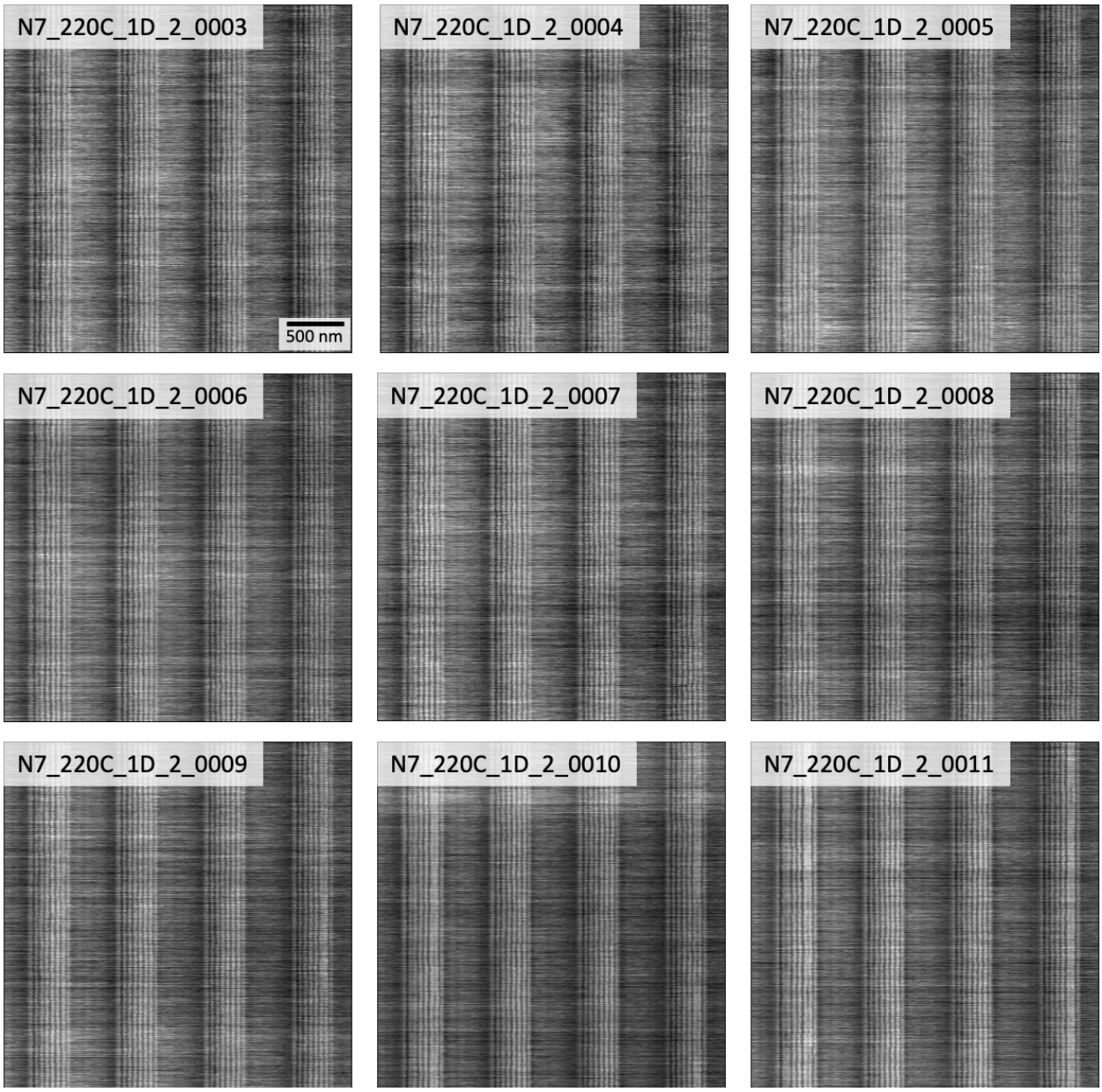

A.3.6 SSD AFM Phase Images at 220 ºC. SSD AFM images taken on the Asylum Cypher ES at 220 ºC under argon and used to create **Figures 3.5** and **Table 3.2**.

Directory: 180611
File base name: N7_220C_1D_2_
File numbers: 0003-0011

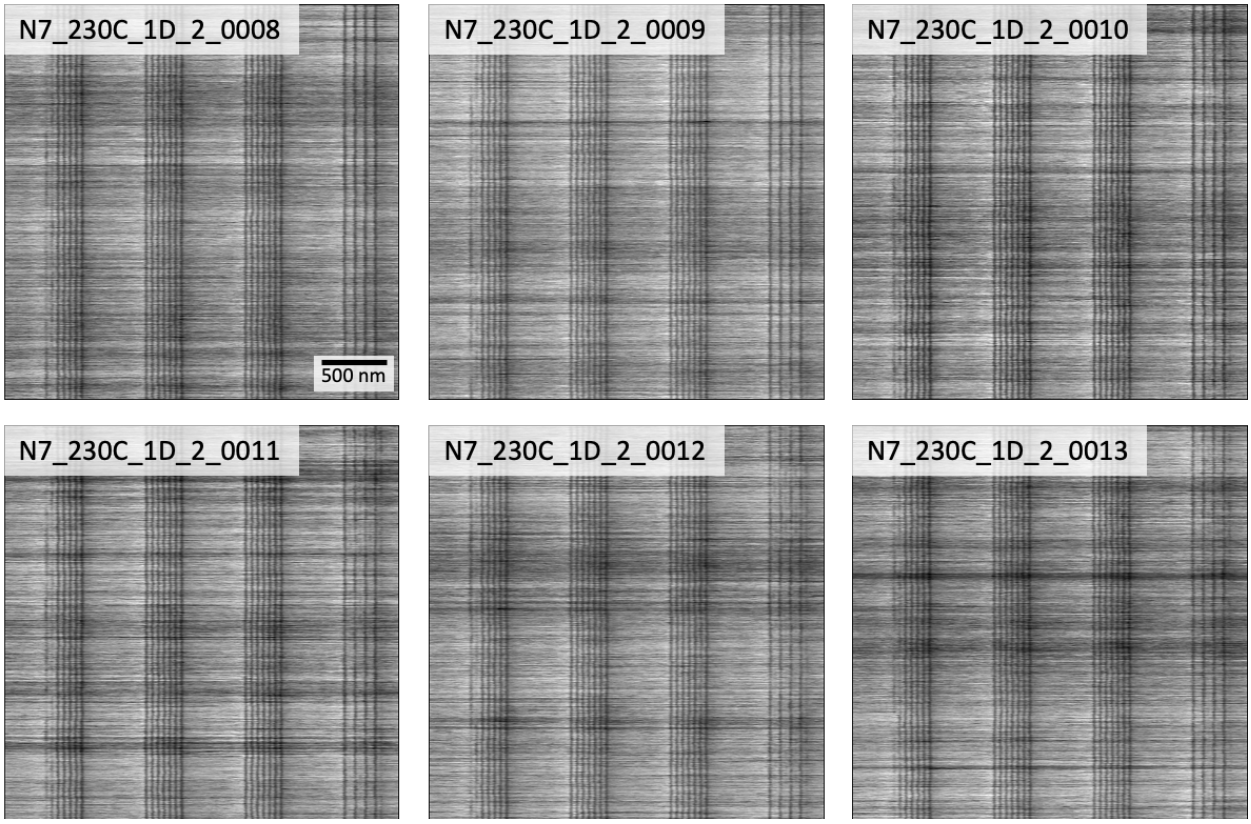

A.3.7 SSD AFM Phase Images at 230 ºC. SSD AFM images taken on the Asylum Cypher ES at 230 ºC under argon and used to create **Figures 3.5** and **Table 3.2**.

Directory: 180611
File base name: N7_230C_1D_2_
File numbers: 0008-0013

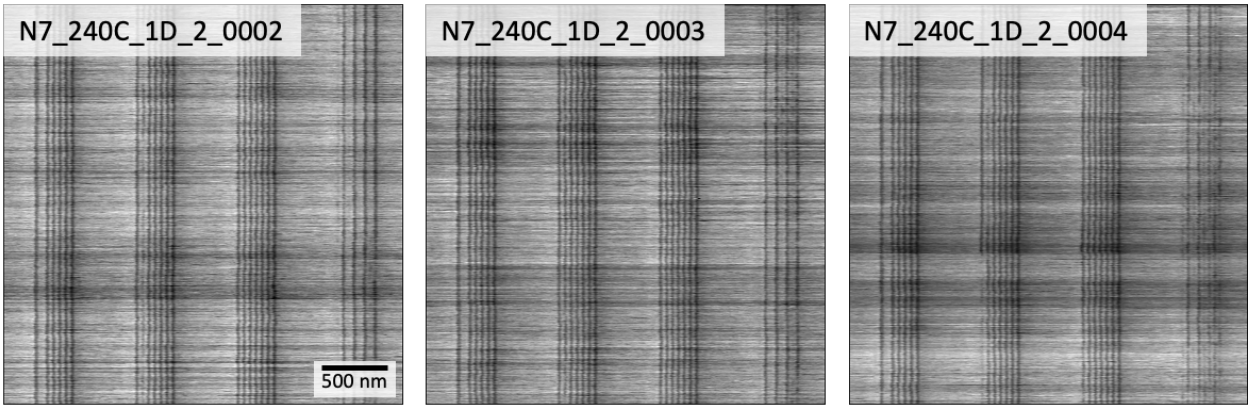

A.3.8 SSD AFM Phase Images at 240 ºC. SSD AFM images taken on the Asylum Cypher ES at 210 ºC under argon and used to create **Figures 3.4-3.7** and **Tables 3.1-3.2**.

Directory: 180611
File base name: N7_240C_1D_2_
File numbers: 0002-0004

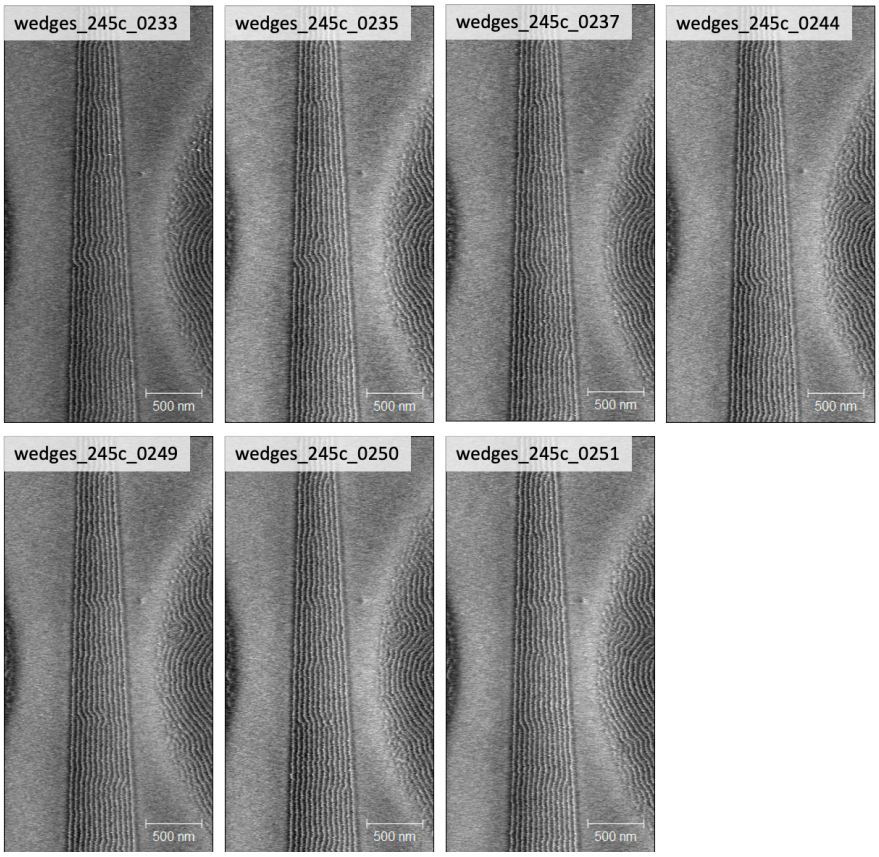

Figure A.4.1 Dislocation Migration Mechanism. AFM phase images taken on an Asylum Cypher ES AFM at 245 °C under argon atmosphere to create **Figure 4.2**.

Directory: 170216
File base name: wedges_245c_
File numbers: 0233, 0235, 0237, 0244, 0249, 0250, 0251

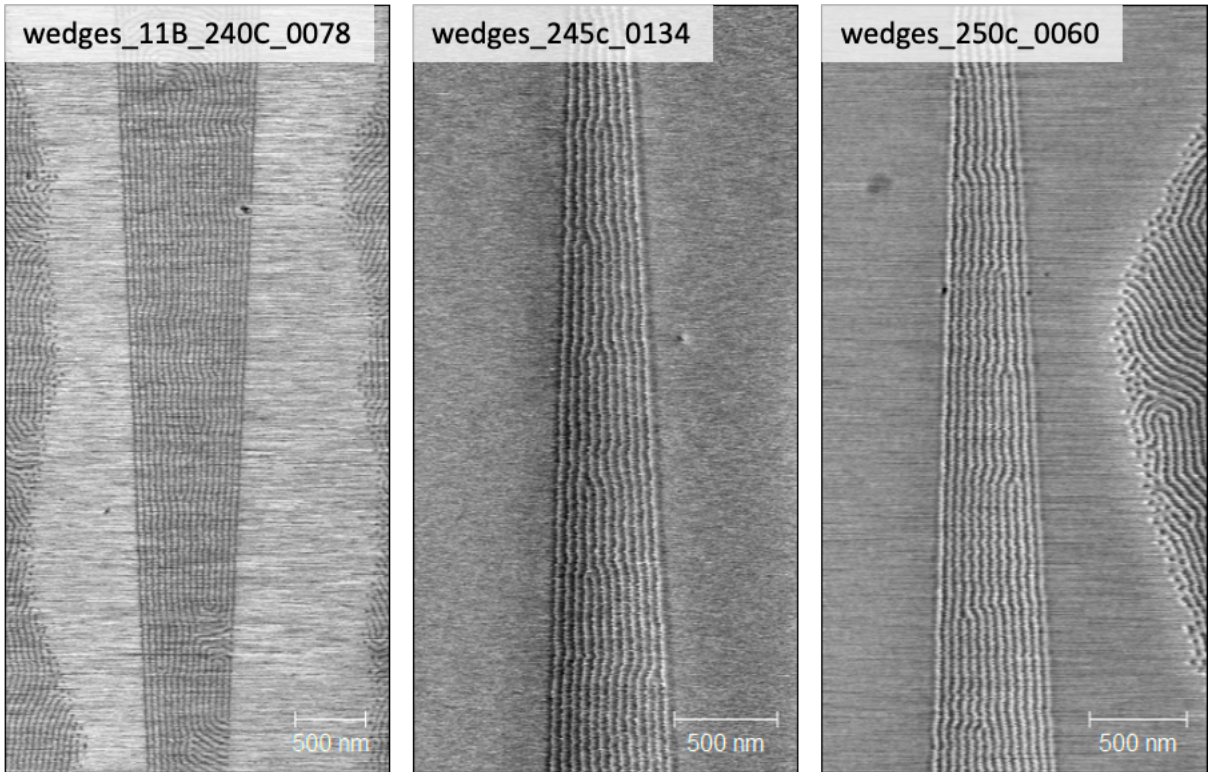

Figure A.4.2 Cumulative Distribution Mapping. Representative AFM phase images taken on an Asylum Cypher ES AFM at 240, 245, and 250 ºC under argon atmosphere to create **Figure 4.3**. The full time series data is available electronically in the Sibener group.

240 ºC:

Directory: 170705
File base name: wedges_11B_240C_
File numbers: 0078 - 0166

245 ºC:

Directory: 170216
File base name: wedges_245c_
File numbers: 0134 - 0344

250 ºC:

Directory: 170216
File base name: wedges_250c_
File numbers: 0060 - 0332

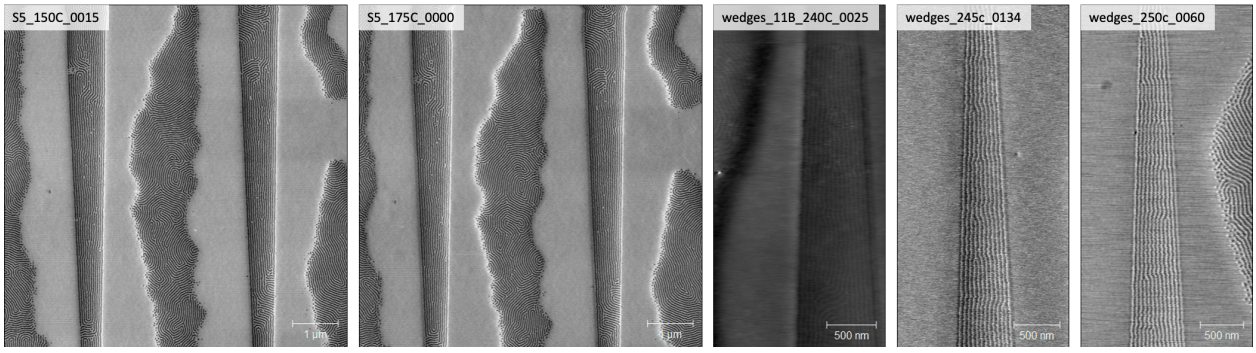

Figure A.4.3 Equilibrium Spacing versus Temperature. Representative AFM phase images taken on an Asylum Cypher ES AFM at 150, 175, 240, 245, and 250 ºC under argon atmosphere to create **Table 4.1** and **Figure 4.4**. One sample was imaged continuously at 150 and 175 ºC, first heating and imaging at 150 ºC then increasing the temperature to 175 ºC. Similarly, an additional sample was used and imaged continuously at 245 and 250 ºC. The full time series data is available electronically in the Sibener group.

150 ºC:

Directory: 200918 → 150 C
File base name: S5_150C_
File numbers: 0015, 0020, 0025, 0030, 0035, 0040, 0045, 0050, 0055, 0060, 0065, 0070, 0075, 0080, 0085, 0090, 0095, 0100, 0105, 0110, 0115, 0120, 0125
Number of data points averaged: 46

175 ºC:

Directory: 200918 → 175 C
File base name: S5_175C_
File numbers: 0000, 0005, 0010, 0015, 0020, 0024, 0030, 0035, 0040, 0044, 0050, 0055, 0060, 0065, 0070, 0075, 0080, 0084, 0090, 0095, 0100, 0105, 0109, 0115, 0120, 0125
Number of data points averaged: 52

240 ºC:

Directory: 170629
File base name: wedges_11B_240C_
File numbers: 0010, 0011, 0013-0074
Number of data points averaged: 64

Figure A.4.3 Continued

245 °C:

Directory: 170216
File base name: wedges_245c_
File numbers: 0155, 0156, 0160, 0161, 0165, 0166, 0170, 0171, 0175, 0176, 0180, 0181, 0185, 0186, 0190, 0191, 0195, 0196, 0200, 0201, 0205, 0206, 0210, 0211, 0215, 0216, 0220, 0221, 0225, 0226, 0230, 0250, 0251, 0255, 0256, 0260, 0261, 0265, 0266, 0269, 0275, 0276, 0280, 0281, 0285, 0286, 0290, 0291, 0295, 0296, 0300, 0301, 0305, 0306, 0310, 0311, 0315, 0316, 0320, 0321, 0325, 0326, 0330, 0331, 0335, 0336, 0340, 0341
Number of data points averaged: 68

250 °C:

Directory: 170216
File base name: wedges_250c_
File numbers: 0060, 0065, 0070, 0075, 0080, 0085, 0090, 0095, 0100, 0105, 0110, 0115, 0120, 0125, 0130, 0135, 0140, 0145, 0150, 0155, 0160, 0165, 0170, 0175, 0180, 0185, 0190, 0195, 0200, 0205, 0210, 0215, 0220, 0225, 0230, 0235, 0240, 0245, 0250, 0255, 0260, 0265, 0270, 0275, 0280, 0285, 0290, 0295, 0300, 0305, 0310, 0315, 0320, 0325, 0330
Number of data points averaged: 55

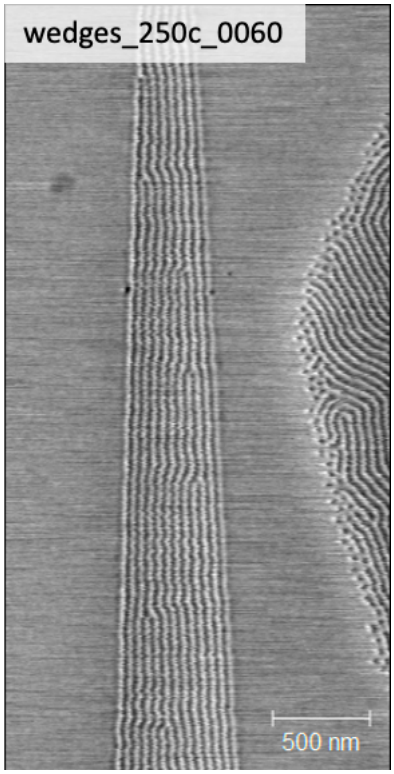

Figure A.4.4 Interfacial Fluctuations Averaging. Representative AFM phase image taken on an Asylum Cypher ES AFM at 250 ºC under argon atmosphere to create **Figure 4.5**. The full time series data is available electronically in the Sibener group.

Directory: 170216
File base name: wedges_250c_
File numbers: 0060 - 0332

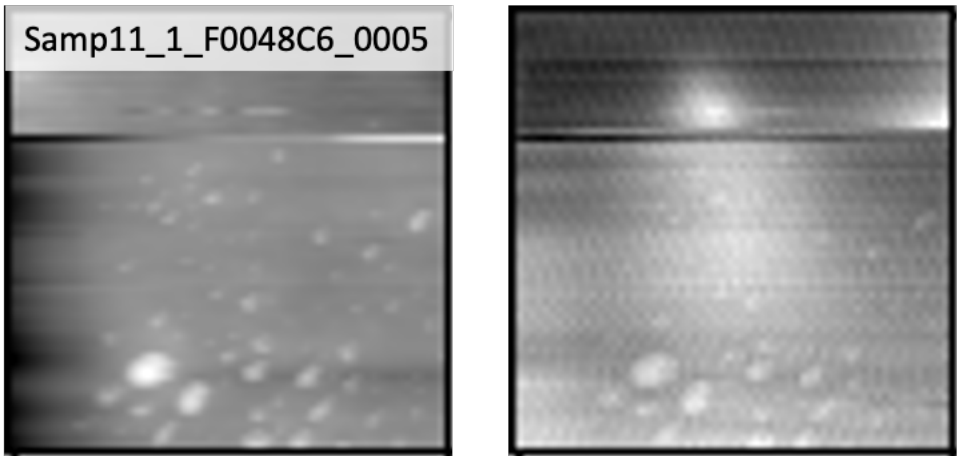

Figure A.5.1 P3HT:PMMA Blend Film. Topography (left), phase (center), and current (right) images of a P3HT:PMMA blend in a 1:1 ratio used to produce **Figure 5.3**.

Directory: 20190227 UChicago (Sibener) SECM Demo
File base name: Samp11_1_F0050C4_
File numbers: 0005

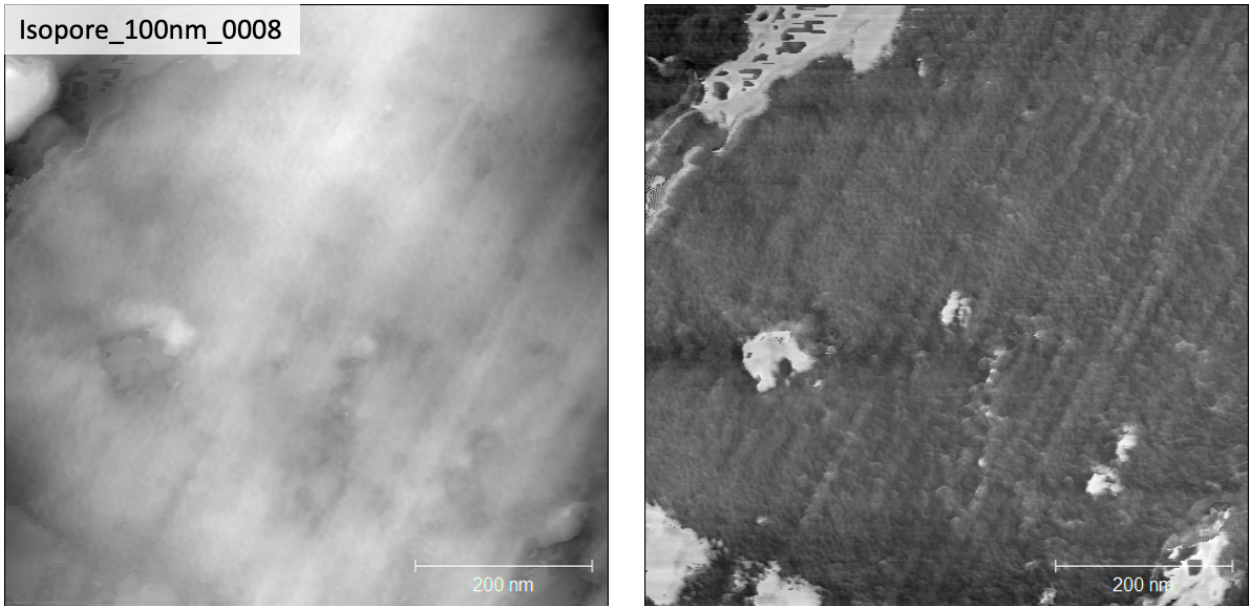

Figure A.5.2 Isopore Membrane AFM Images. AFM topography (left) and phase (right) images taken on an Asylum Cypher ES AFM to create **Figure 5.4**. A first order flatten has been applied to both images.

Directory: 210402
File base name: Isopore_100nm_
File numbers: 0008

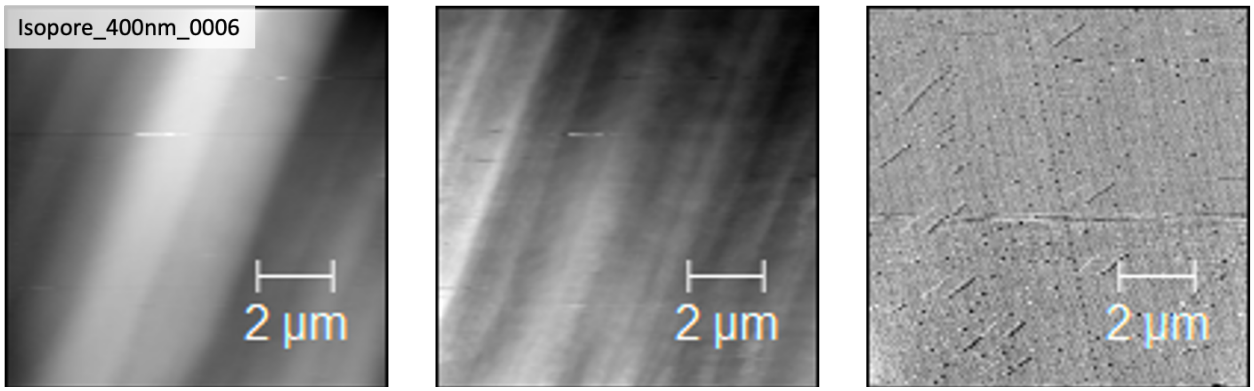

Figure A.5.3 Isopore Membrane SECM-AFM Images. Topography (left), phase (center), and current (right) images of a track-etched Isopore membrane from Millipore Sigma used to produce **Figure 5.4**. A first order flatten has been applied to all images.

Directory: 210614
File base name: Isopore_400nm_
File numbers: 0006